

*Sister Rod Destructive Examinations (FY21)*

# ***Appendix F: Cyclic Integrated Reversible- Bending Fatigue Tests***

## **Spent Fuel and Waste Disposition**

*Prepared for  
US Department of Energy  
Spent Fuel and Waste Science  
and Technology*

*Oak Ridge National Laboratory*

*Rose Montgomery,  
Jy-An Wang, Paul Cantonwine,  
Yadukrishnan Sasikumar,  
Hong Wang, Bruce Bevard,  
Darren Skitt, Oscar Martinez*

***March 31, 2022***

**M2SF-22OR010201042**

**ORNL/SPR-2021/2291**

**ORNL/SPR-2020/1780 Revision 1**

This report was prepared as an account of work sponsored by an agency of the United States Government. Neither the United States Government nor any agency thereof, nor any of their employees, makes any warranty, express or implied, or assumes any legal liability or responsibility for the accuracy, completeness, or usefulness of any information, apparatus, product, or process disclosed, or represents that its use would not infringe privately owned rights. Reference herein to any specific commercial product, process, or service by trade name, trademark, manufacturer, or otherwise, does not necessarily constitute or imply its endorsement, recommendation, or favoring by the United States Government or any agency thereof. The views and opinions of authors expressed herein do not necessarily state or reflect those of the United States Government or any agency thereof.



## SUMMARY

This report documents work performed under the Spent Fuel and Waste Disposition's Spent Fuel and Waste Science and Technology program for the US Department of Energy (DOE) Office of Nuclear Energy (NE). This work was performed to fulfill Level 2 Milestone M2SF-22OR010201042, "FY2021 ORNL Report on High Burnup Sibling Pin Testing Results," within work package SF-22OR01020104 and is an update to the work reported in M2SF-21OR010201032, M2SF-19ORO010201026 and M2SF-19OR010201028.

As a part of DOE NE High Burnup Spent Fuel Data Project, Oak Ridge National Laboratory (ORNL) is performing destructive examinations (DEs) of high burnup (HBU) (>45 GWd/MTU) spent nuclear fuel (SNF) rods from the North Anna Nuclear Power Station operated by Dominion Energy. The SNF rods, called *sister rods* or *sibling rods*, are all HBU and include four different kinds of fuel rod cladding: standard Zircaloy-4 (Zirc-4), low-tin (LT) Zirc-4, ZIRLO, and M5. The DEs are being conducted to obtain a baseline of the HBU rods' condition before dry storage and are focused on understanding overall SNF rod strength and durability. Composite fuel and defueled cladding will be tested to derive material properties. Although the data generated can be used for multiple purposes, one primary goal for obtaining the post-irradiation examination data and the associated measured mechanical properties is to support SNF dry storage licensing and relicensing activities by (1) addressing identified knowledge gaps and (2) enhancing the technical basis for post-storage transportation, handling, and subsequent disposition.

This appendix documents the status of the ORNL Phase 1 DE activities related to tests of the sister rods using the Cyclic Integrated Reversible-Bending Fatigue Tester (CIRFT) in Phase 1 of the sister rod test program.

Table FS-1 provides the status of the CIRFT tests.

**Table FS-1. DE.05 status.**

Planned DE		P.I.	Status	Comments
DE.05	Perform CIRFT tests to determine static, dynamic, and cumulative effects and fatigue lifetime	P.E. Cantonwine	In progress	<p>Thirty-one tests using the CIRFT were completed on 25 specimens. The results are consistent with those for other rods of the same type that were tested in the past, but they fall on the lower side of the database, especially the rods with Zirc-4 and LT Zirc-4 cladding. One dynamic test was removed from the fatigue database because, after closer examination of the data, it was determined the rod failed during the preceding static test. The heat treatments applied to selected rods resulted in a shorter fatigue lifetime, which is suspected to be related to their observed reduced flexural rigidity.</p> <p>The flexural rigidity measured for the baseline sister rods is consistent with, although on the lower side of, previously tested <math>17 \times 17</math> specimens for M5-, ZIRLO-, and LT Zirc-4 clad specimens. The heat-</p>

Planned DE		P.I.	Status	Comments
				<p>treated rods have a lower flexural rigidity than the corresponding baseline rod, except the Zirc-4 clad specimens, which have a higher flexural rigidity which is possibly related to the design's longer pellet length. However, because of the recent calculation of large uncertainty in the CIRFT-measured flexural rigidity values (see Appendix G), there is now less certainty in these observed trends.</p> <p>A test on a specimen with a grid-to-rod-fretting mark in the maximum strain location did not result in a reduced fatigue lifetime.</p> <p>One test remains to be completed on a specimen that has multiple pellet-pellet gaps. The specimen will be tested to determine whether the gaps have an impact on the fatigue lifetime.</p> <p>The cumulative effects test fixture is being redesigned.</p>
	Post-test imaging and dogbone characterization	Skitt	Complete	All completed test pairs have been characterized.
	Post-test SEM characterization of fracture surface	Sasikumar	In Progress	A sample preparation procedure has been developed and the fracture surface of one sample has been characterized. Features consistent with fatigue were observed, but no conclusions can be made at this early stage of the activity. More specimens will be examined, with the goal of identifying the initiating crack location and direction of crack propagation.
	Finite element modeling of selected performance characteristics	Martinez	In progress	Modeling of the cumulative impact test to determine the appropriate fixture configuration is complete and indicates that applying an impact to a specimen mounted in a dogbone will yield an impact load that is higher than desired. In the coming year, an alternative testing approach will be developed to consider the effect of cumulative impact loads on fatigue.

## **ACKNOWLEDGMENTS**

Many thanks to our US Department of Energy Office of Nuclear Energy sponsor Ned Larson, along with the Spent Fuel and Waste Science and Technology storage and transportation program leadership for their continued support. The sister rod project would not have been possible without the vision and support of the Electric Power Research Institute, Westinghouse, Framatome, and Dominion Energy.

This work would not have been possible without the support and expertise provided by the leadership and staff members of Oak Ridge National Laboratory's Irradiated Fuel Examination Laboratory. Special thanks go to Scott Thurman, who built the dogbones in-cell, tracked the specimens and the tests, and helped perform the testing, and to Bryan Woody for his assistance with in-cell testing activities. Ricardo Muse supported the fabrication jobs associated with the Cyclic Integrated Reversible-Bending Fatigue Tester tests, and we appreciate his continued support.

This page intentionally blank

## CONTENTS

SUMMARY .....	iii
ACKNOWLEDGMENTS .....	v
CONTENTS.....	vii
LIST OF FIGURES .....	ix
LIST OF TABLES .....	xiii
REVISION HISTORY.....	xv
ACRONYMS .....	xvii
F-1. Introduction .....	1
F-2. CIRFT Description .....	1
F-3. Data Acquisition, Data Processing, Basic Information, and Extended Information .....	4
F-3.1 Basic Calculated Information.....	7
F-3.2 Extended Calculated Information within the Context of CIRFT .....	7
F-3.2.1 Pellet Bonding Stiffening.....	8
F-3.2.2 Discontinuous Cladding Support .....	8
F-3.2.3 Cladding Hydride Reorientation Effects .....	9
F-3.2.4 Cladding Irradiation Defect Annealing.....	9
F-3.2.5 Normal Condition Impacts.....	9
F-4. Comparison Data Available from Previous ORNL Tests.....	10
F-5. Description of the Sister Rods Tested .....	12
F-6. Selection of CIRFT Test Conditions .....	20
F-7. Test Results .....	22
F-7.1 Static Tests .....	22
F-7.2 Dynamic Tests.....	24
F-7.3 Cumulative Effects Tests .....	25
F-7.4 Comparisons of Paired Specimens.....	33
F-7.5 Imaging of the Fractured Specimens.....	35
F-7.6 Scanning Electron Microscope (SEM) Characterization of Fracture.....	61
F-8. CIRFT Cumulative Effects Fixture Development.....	66
F-8.1 Finite Element Modeling of the Cumulative Impactor .....	67
F-8.1.1 Finite Element Modeling Software .....	67
F-8.1.2 Finite Element Model.....	68
F-8.1.3 Material Models .....	69
F-8.1.4 Initial Conditions, Boundary Conditions and Load Cases .....	70
F-8.1.5 Load Cases .....	70
F-8.2 Results, Discussion, and Conclusions from the Cumulative Effects Fixture Modeling .....	71
F-8.3 Verification of FEA Results Using the Cumulative Effects Fixture .....	74
F-8.4 Summary .....	75
REFERENCES .....	76

This page is intentionally blank

## LIST OF FIGURES

Figure F-1 Two views of the ORNL CIRFT: (a) a surrogate rod specimen undergoing out-of-cell testing with three linear variable differential transducers (LVDTs) for curvature measurements, and (b) an SNF rod being tested in the hot cell.....	2
Figure F-2. Schematic drawings of U-frame setup for reversal bending when rigid arms are (a) closing, (b) neutral, and (c) opening.....	3
Figure F-3. Image showing the grip design of CIRFT with one end-block removed. ....	4
Figure F-4. The LVDT measurements for the curvature calculation.....	5
Figure F-5. An example of a single cycle from two low cycle (0.05 Hz) tests used for equipment performance confirmation showing (a) the instantaneous applied bending moment, (b) the calculated curvature, and (c) the moment-curvature hysteresis loop. The example is also representative of the type of data collected in the fatigue performance portion of the test session. ....	6
Figure F-6. Cladding and pellet stack (a) in the neutral position and (b) in bending. [F-5]. ....	8
Figure F-7. The static test data for 30AD05-0697-0850 represent the typical result.....	22
Figure F-8. Results of CIRFT tests plotted with reference data, applied moment vs. cycles to failure. The error bars on the sister rod data represent the calculated uncertainty (0.8 N-m) in Section G-3.3, Appendix G (non-sister rod data from [F-4], [F-5])......	27
Figure F-9. Results of CIRFT tests completed to date, strain amplitude vs. cycles to failure. The error bars on the sister rod data represent the calculated uncertainty in Section G-3.4, Appendix G (non-sister rod data from [F-4], [F-5])......	28
Figure F-10. Average stress amplitude of the composite rod based on Eq. (F-7), as a function of cycles to failure for the sister rods. The error bars on the sister rod data represent the calculated uncertainty in Section G-3.5, Appendix G. ....	29
Figure F-11. Cladding stress amplitude as a function of cycles to failure for the sister rods. The error bars on the sister rod data represent the calculated uncertainty in Section G-3.5, Appendix G. ....	30
Figure F-12. CIRFT-measured flexural rigidity of the sister rod segments tested as a function of estimated segment burnup plotted with previous CIRFT data. ....	31
Figure F-13. Trend of CIRFT-measured dynamic flexural rigidity with applied bending moment. The error bars on the sister rod data represent the calculated uncertainty in Section G-3.6, Appendix G. ....	32
Figure F-14. 6U3K09-3353-3506 post-fatigue test condition.....	37
Figure F-15. 6U3K09-2310-2463 post-fatigue test condition.....	38
Figure F-16. 6U3K09-3200-3353 post-fatigue test condition.....	39
Figure F-17. 6U3K09-2635-2788 post-fatigue test condition.....	40
Figure F-18. 6U3K09-2463-2616 post-fatigue test condition.....	41
Figure F-19. 3F9N05-2710-2863 post-fatigue test condition. ....	42
Figure F-20. 3F9N05-2329-2482 post-fatigue test condition. ....	43
Figure F-21. 3F9N05-0719-0872 post-fatigue test condition. ....	44

Figure F-22. 3D8E14-2963-3116 post-fatigue test condition. ....	45
Figure F-23. 30AD05-2630-2783 post-fatigue test condition.....	46
Figure F-24. 30AE14-0672-0825 post-fatigue test condition. ....	47
Figure F-25. F35P17-1855-2008 post-fatigue test condition. ....	48
Figure F-26. F35P17-3159-3312 post-fatigue test condition. ....	49
Figure F-27. 3A1F05-2025-2178 post-fatigue test condition. ....	50
Figure F-28. 3A1F05-1853-2006 post-fatigue test condition. ....	51
Figure F-29. 30AD05-0697-0850 post-fatigue test condition (broken ends only). ....	52
Figure F-30. 30AD05-2050-2203 post-fatigue test condition (broken ends only). ....	53
Figure F-31. 30AE14-2850-3003 post-fatigue test condition (broken ends only). ....	54
Figure F-32. 30AE14-3156-3309 post-fatigue test condition (broken ends only). ....	55
Figure F-33. 3A1F05-3214-3367 post-fatigue test condition. ....	56
Figure F-34. 3D8E14-719-872 post-fatigue test condition. ....	57
Figure F-35. 3D8E14-2412-2565 post-fatigue test condition. ....	58
Figure F-36. 3A1F05-3367-3520 post-fatigue test condition. ....	59
Figure F-37. 3D8E14-1178-1331 post-fatigue test condition. ....	60
Figure F-38. Applied moment and measured radius of curvature as a function of cumulative time for the final test session of 3D8E14-2963-3116. The decrease in radius of curvature is likely caused by the initiation and growth of a fatigue crack. ....	62
Figure F-39. 23X montage of the surface of the fatigue failure in sample 3D8E14-2963-3116. The areas identified in the various quadrants were investigated at higher magnification (see Figures F-40 to F-43). ....	63
Figure F-40. 330× and 1,000× images of quadrant 1 in sample 3D8E14-2963-3116. ....	64
Figure F-41. 100× and 1,000× images of quadrant 3 in sample 3D8E14-2963-3116, approximately 180° from region in quadrant 1, that is suspected to have failed after fatigue test ended. ....	64
Figure F-42. 120× and 500× images of quadrant 2 in sample 3D8E14-2963-3116, showing signs of fatigue striations typical of fatigue crack propagation, indicating propagation in the circumferential direction. ....	65
Figure F-43. 120× and 350× images of quadrant 4 in sample 3D8E14-2963-3116 showing signs of fatigue striations typical of fatigue crack propagation. The flatness of the feature on the cladding ID may be associated with fatigue initiation. There are also circumferential cracks near the cladding OD that may be associated with hydrides. ....	65
Figure F-44. Cumulative shock fixture developed to apply a normal transport condition shock before fatigue testing. ....	66
Figure F-45. The cumulative impactor CAD model (left) and finite element model (right) include a rod segment with discrete pellets, guide blocks, and a weight with impact geometry. ....	68
Figure F-46. 304 stainless steel (left) and Zirc-4 (right) true stress–strain curves used compared with corresponding engineering stress–strain curves. ....	70
Figure F-47. Impactor end configuration (a) results for load cases 1–4. ....	71



---

Figure F-48. Impactor end configuration (a) results for load cases 5–9. ....	72
Figure F-49. Plastic strain occurred on the dimples for impactor end configuration (a). ....	73
Figure F-50. CIRFT dogbone. ....	73
Figure F-51. Physical test configurations with the cumulative effects fixture.....	74
Figure F-52. Impactors used in the physical tests. ....	74

This page is intentionally blank

## LIST OF TABLES

Table FS-1. DE.05 status. ....	iii
Table F-1. Reference Dynamic Dataset [F-4]. ....	10
Table F-2. Sister rod segments selected for CIRFT. ....	13
Table F-3. CIRFT specimen and test pairing. ....	21
Table F-4. Static test results. ....	23
Table F-5. Sister rod CIRFT test results to date. ....	26
Table F-6. Results arranged by paired specimens (baseline rods vs. heat-treated rods) for static/dynamic and dynamic CIRFT. ....	34
Table F-7. Summary of visual observations of CIRFT-fractured dogbones. ....	36
Table F-8. CIRFT Specimens identified for SEM characterization. ....	62
Table F-9. Cumulative impactor model minimum material properties. ....	69
Table F-10 Cumulative tester FEA load case summary. ....	70
Table F-11. Summary of fuel rod maximum g-load during impact with end configuration (a). ....	72

This page is intentionally left blank.

## REVISION HISTORY

Date	Changes
3/29/2019	Initial release
9/27/2019	Revised to include additional data and incorporate comments from the previously released report.
10/29/2020	The CIRFT detailed report was moved to Appendix F and was updated to include the most recent information.
11/30/2020	Comments received on the draft were incorporated, and the document numbering was revised to reflect its M2 status.
10/29/21	Section F-7.6 has been added. The results of the uncertainty estimates (Appendix G) were integrated into the data table and plots, and related discussions were modified. One low data point was investigated and removed from the CIRFT dataset, and the supporting information has been added to the report (Section F-7.1). Minor clarifications have been made throughout.
3/31/22	Minor formatting changes and clarifications have been made in response to comments received on the 10/29/21 report (Section F-2 paragraph 4, Section F-3 paragraph 1, Figure F-5 caption, addition of reference F-19). The document ID number was revised to reflect its M2 status and the issue date was changed.

This page is intentionally left blank.

## **ACRONYMS**

ASME	American Society of Mechanical Engineers
BPVC	Boiler and Pressure Vessel Code
BWR	boiling water reactor
CIRFT	cyclic integrated reversible-bending fatigue tester
DE	destructive examination
DOE	US Department of Energy
FEA	finite element analysis
FHT	full-length fuel rod heat treatment
GTRF	grid-to-rod fretting
HBU	high burnup
ID	inner diameter
LSTC	Livermore Software Technology Corporation
LT	low tin
NDE	nondestructive examination
NE	Office of Nuclear Energy
NRC	US Nuclear Regulatory Commission
OD	outer diameter
ORNL	Oak Ridge National Laboratory
PWR	pressurized water reactor
SEM	scanning electron microscope
SNF	spent nuclear fuel

This page is intentionally left blank.



## F-1. Introduction

Spent nuclear fuel (SNF) assemblies must be shipped to other sites for processing and disposal. During shipment, the fuel is typically oriented horizontally, and the fuel rods are subject to periodic alternating loads related to the movement of the vehicle that results in alternating bending of the SNF fuel rods. The number of bending cycles is related to the length of the shipping route, with longer routes producing more cycles. Because it is well-known that cyclic loads can produce failures, even when the stress and strain imposed are below the material's yield point, investigation of the SNF's fatigue behavior is prudent.

This report discusses the results of fatigue testing conducted at Oak Ridge National Laboratory (ORNL) using the Cyclic Integrated Reversible-Bending Fatigue Tester (CIRFT) created by the US Department of Energy (DOE) Office of Nuclear Energy (NE) for the High Burnup Spent Fuel Data Project and its sister rods [F-1, F-2, F-3]. The results of the tests are compared with results obtained over the last decade using the same CIRFT for the US Nuclear Regulatory Commission (NRC).

## F-2. CIRFT Description

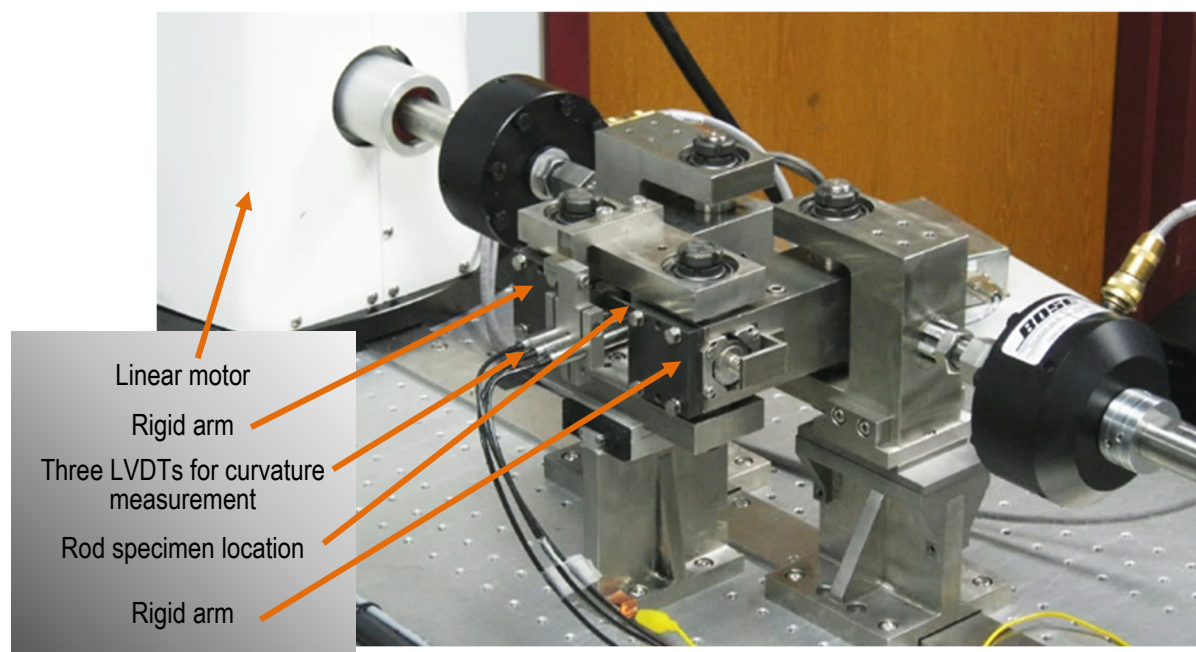
The CIRFT, shown in Figure F-1, is hardware developed by ORNL [F-4, F-5] to test the fatigue lifetime of SNF in postulated normal transportation vibration conditions. The machine oscillates 6-inch segments of high burnup (HBU) SNF until fatigue failure occurs. The CIRFT uses a U-frame with two rigid arms that convert the motor's linear motion into a bending moment exerted on the rod segment. The two U-frame arms are driven by two electromagnetic-force-based motors. The motors (Bose model LM2) have a maximum load capacity of  $\pm 3,000$  N and a maximum stroke of  $\pm 25.6$  mm.

Each tested SNF segment is fitted with special end grips, or *dogbones*, which are epoxied onto both ends of the segment. When prepared this way, the SNF segment is referred to as a *dogbone*. The epoxy provides a compliant layer that is important for ensuring pure bending. The epoxy layer thickness depends on the as-built diameter of dogbone recesses and segment outer diameter. This layer is important for ensuring pure bending. When the dogbone is engaged with the U-frame, bending is imposed by the motor through the U-frame, as illustrated in Figure F-2, with a cycle that progresses as follows: the dogbone (1) begins in the neutral position (i.e., no bending), (2) is flexed laterally away from the front face of the machine, (3) is returned to the neutral position, (4) is flexed laterally toward the front face of the machine, and (5) is returned to the neutral position. The CIRFT can flex the rod specimen at 5–10 Hz during the dynamic test, with the sister rod tests performed at 5 Hz.

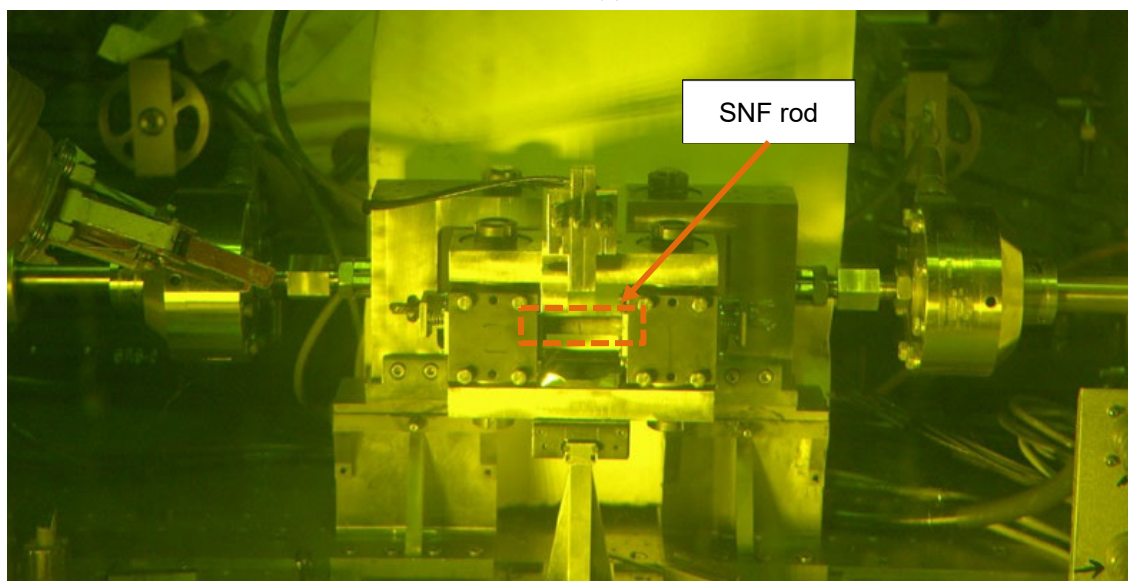
To ensure the desired motion, the CIRFT is specifically configured to test SNF rod segments that have diameters ranging from 9.70 to 11.74 mm, with a fixed segment length of 152.40 mm (6 in.). The test's gauge section is the 50.80 mm (2 in.) SNF rod length between the dogbones, where the maximum bending deflection occurs.

To date, two types of tests have been performed: a *static* test and a *dynamic test*. A third test, the *cumulative effects* test, is still in the equipment development stage. The dynamic test is the standard fatigue test performed on the CIRFT. Dynamic testing is performed in a series of sessions, where a session consists of two displacement-controlled cyclic tests performed at 0.05 Hz for a low number of cycles at loads less than the 5 Hz fatigue test (to confirm equipment performance) and a load-controlled cyclic test at 5 Hz (to test fatigue performance). The number of sessions in a complete dynamic test is dependent on the cycles to failure and varies from 1 session (for low-cycle fatigue conditions) to as many as 7 sessions (for high-cycle fatigue conditions) [F-19]. During the dynamic test, the SNF segment is flexed at a fixed frequency and motor stroke length. For the static test, the segment is flexed slowly to the maximum stroke of the machine and the deflection of the SNF specimen is measured. The static test does not typically result in fracture of the specimen because the largest possible machine stroke usually cannot impose enough deflection on the SNF specimen to exceed the cladding tensile strength and cause a non-

fatigue fracture. Although the static test can be followed by a dynamic test, the flexure imposed during the static test is much higher than that imposed during the dynamic test, and the large deflection may reduce the flexural rigidity and fatigue lifetime, even without fracture of the SNF segment, as discussed in later sections of this appendix. The cumulative test will impose impacts on the SNF segment before a dynamic test is performed; the cumulative test is meant to determine whether periodic impacts of the rod with other rods or the packaging during transport are detrimental to the fatigue lifetime.

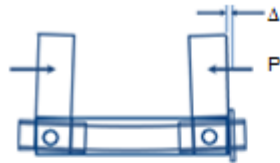


(a)

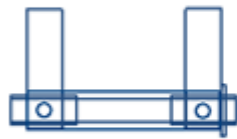


(b)

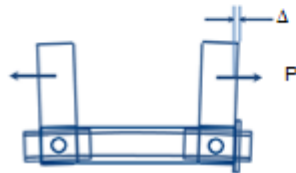
**Figure F-1 Two views of the ORNL CIRFT: (a) a surrogate rod specimen undergoing out-of-cell testing with three linear variable differential transducers (LVDTs) for curvature measurements, and (b) an SNF rod being tested in the hot cell.**



(a) Rigid arms are closing. The curvature is concave outward and designated with a negative sign.



(b) Rigid arms are in neutral position.

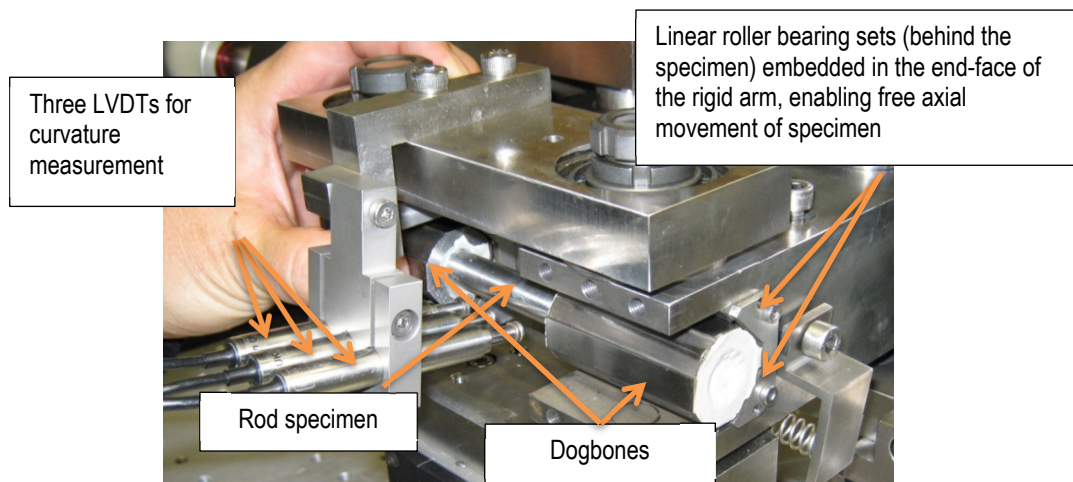


(c) Rigid arms are opening. The curvature concave inward and designated with a positive sign.

Figure F-2. Schematic drawings of U-frame setup for reversal bending when rigid arms are (a) closing, (b) neutral, and (c) opening.

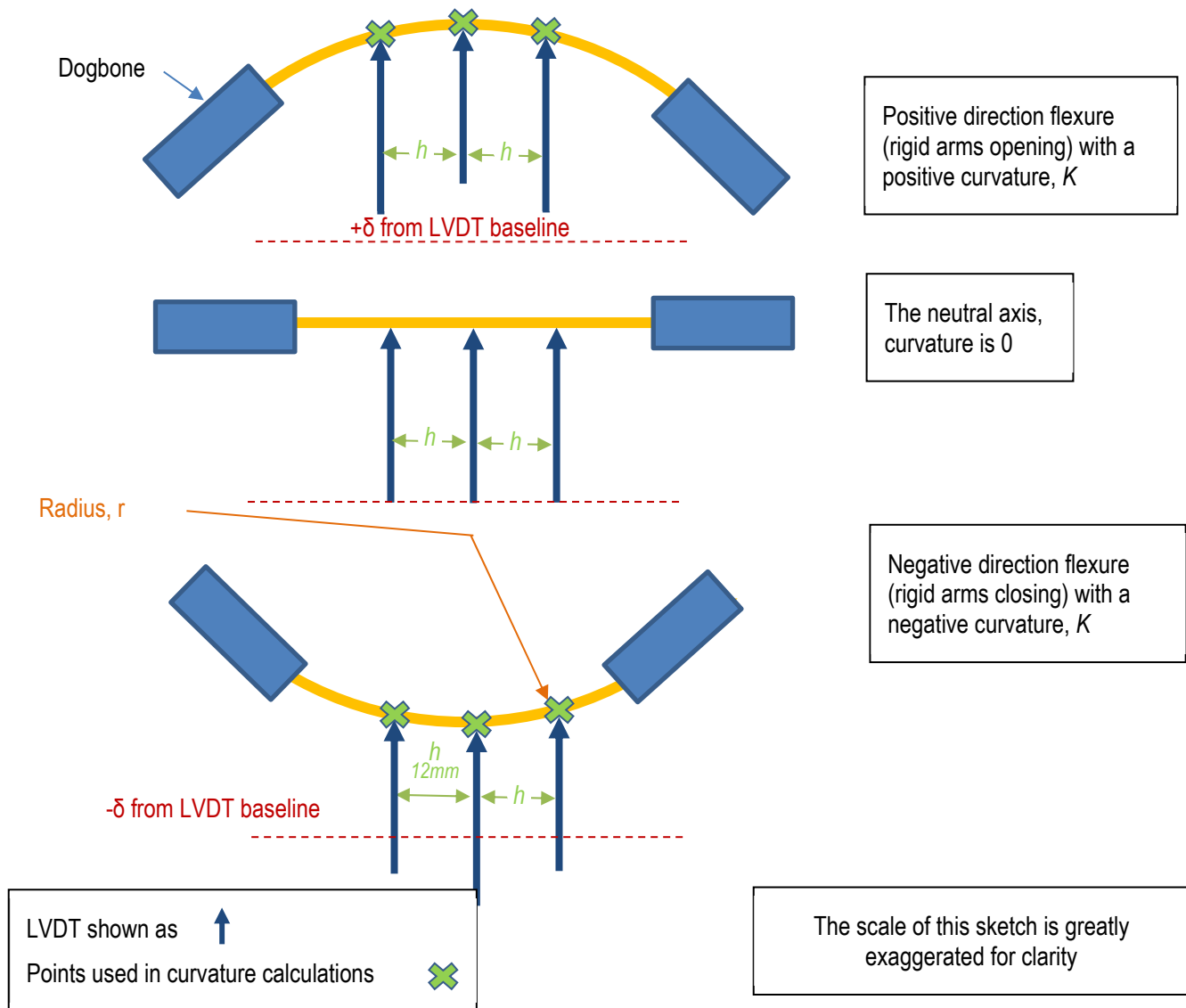
### F-3. Data Acquisition, Data Processing, Basic Information, and Extended Information

This section summarizes the full discussion provided by Wang and Wang [F-4, F-5, F-19]. The key data acquired during the CIRFT test include the number of cycles to failure and the bending moment imposed. The bending moment is calculated based on the motor stroke length applied (set by the user) and the deflection of the SNF rod segment, which is measured using three LVDTs, as shown in Figure F-3. A view of one end of a test specimen is shown in Figure F-3 with the end-block removed, allowing a view of the LVDTs. Online monitoring of the calculated flexural rigidity is used to shut down the machine at the onset of failure.



**Figure F-3. Image showing the grip design of CIRFT with one end-block removed.**

The distances built into the CIRFT machine and the length of the segment dogbone are important because they are used to calculate all load, moment, and curvature values. Important fixed physical distances include the length of the U-frame arms (101.60 mm) and the location and contact geometry of the LVDTs. Also, the motor's recorded stroke length during the test is directly applied in the data reduction, and the SNF rod outer diameter (OD) is used to calculate strain and stress.



**Figure F-4. The LVDT measurements for the curvature calculation.**

The rod curvature,  $K$ , is calculated as the inverse of the radius, assuming the SNF segment forms a short circular arc. As illustrated in Figure F-4, the known spacing between the LVDTs ( $h$ , 12 mm) is used with the measured LVDT deflection to determine the instantaneous curvature of the dogbone gauge section during the test. The raw data are denoised and further adjusted based on the type of LVDT used in the test and any bias observed in the LVDT measurements. An example of the processed data is provided in Figure F-5.

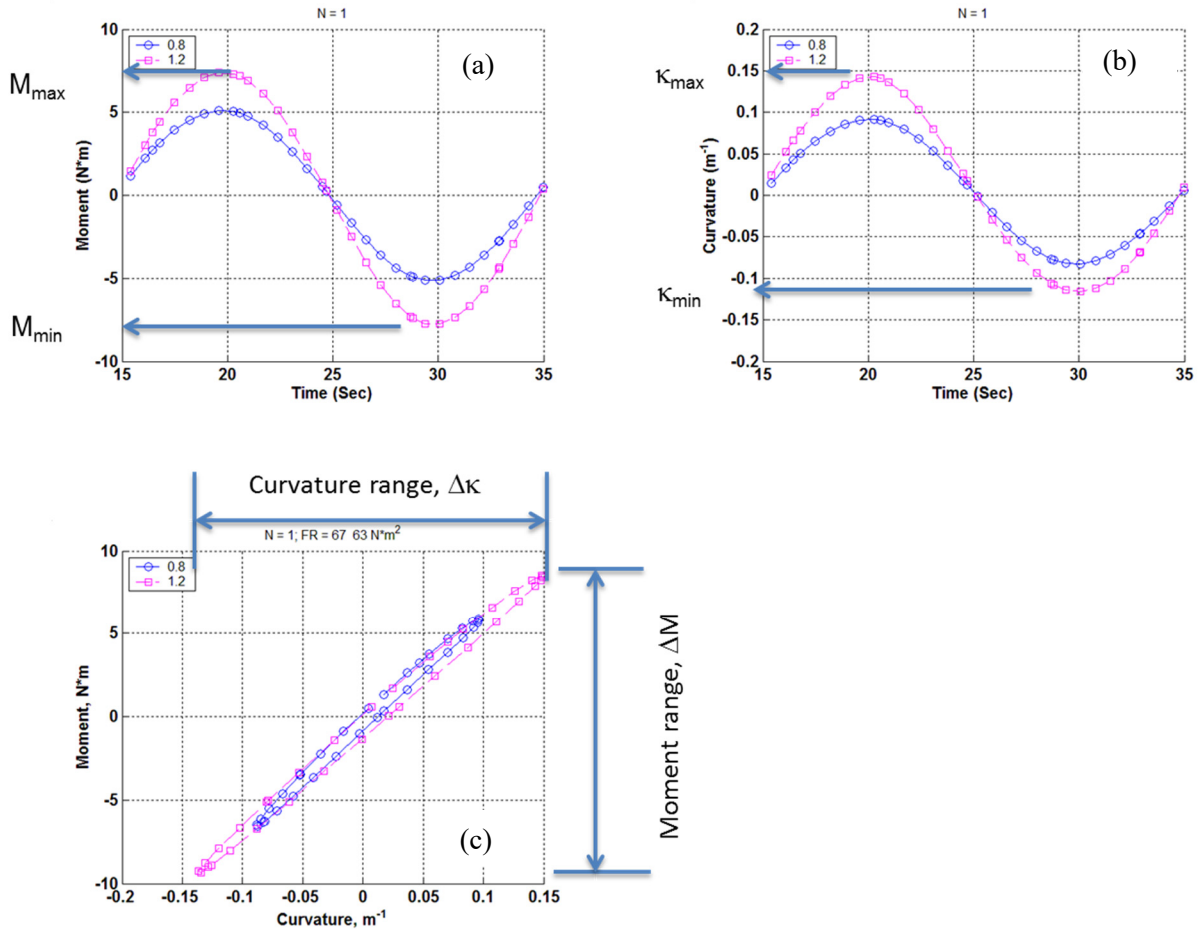


Figure F-5. An example of a single cycle from two low cycle (0.05 Hz) tests used for equipment performance confirmation showing (a) the instantaneous applied bending moment, (b) the calculated curvature, and (c) the moment-curvature hysteresis loop. The example is also representative of the type of data collected in the fatigue performance portion of the test session.

The radius,  $r$ , is calculated by determining the physical coordinates described by the measured LVDT deflections  $d_1$ ,  $d_2$ , and  $d_3$  and by scribing them with a circle:

$$\sqrt{(x_0 - d_2)^2 + y_0^2}, \quad (F-1)$$

where:

$$x_0 = \frac{-2m_a m_b h - m_a(d_2 + d_3) + m_b(d_1 + d_2)}{2(m_b - m_a)}, \quad (F-2)$$

and

$$y_0 = -\frac{1}{m_a} \left( x_0 - \frac{d_1 + d_2}{2} \right) - \frac{h}{2}, \quad (F-3)$$



where 
$$m_a = \frac{h}{d_2 - d_1} \text{ and } m_b = \frac{h}{d_3 - d_2}, \quad (\text{F-4})$$

and  $h$  is the sensor distance fixed at 12 mm.

Corrections are made to the LVDT data ( $d_1$ ,  $d_2$ ,  $d_3$ , and  $h$ ) as described in the work by Wang and Wang [F-7].

### F-3.1 Basic Calculated Information

To provide a basis for comparing the performance of different fuel rod designs, it is necessary to calculate additional parameters such as the stress and strain, and they are typically discussed in terms of their maximum amplitude for CIRFT. It is also useful to survey the flexural rigidity, which tends to decrease as the test progresses. Typically, the flexural rigidity at the beginning of the test is discussed as a comparison point among rod types. The strain and stress parameters are calculated based on standard formulae for a circular beam in bending.

The maximum gauge strain, which occurs at the maximum deflections in the cycle and at the outermost radius of the rod, is calculated as the curvature multiplied by the LVDT maximum deflection:

$$\varepsilon = \kappa \times y_{max}. \quad (\text{F-5})$$

The average moment applied to the rod is

$$M = F \times L, \quad (\text{F-6})$$

where  $F$  is the averaged value of the load applied at the timespan of interest (typically 0.001 s in the dynamic test) by the CIRFT motors, and  $L$  is the fixed U-frame loading arm length (101.60 mm).

The maximum rod stress is calculated as

$$\sigma = M \times y_{max} / I, \quad (\text{F-7})$$

where  $I$  is the area moment of inertia of the composite SNF rod calculated based on the geometry of cladding and solid pellet section.

The flexural rigidity,  $EI$ , provides a means to generate the stress-strain relationship associated with  $M$ - $\kappa$ . The average calculated bending moment ( $\Delta M$ ) and average measured curvature ( $\Delta \kappa$ ) are used to characterize the average flexural rigidity over the timespan of interest:

$$EI = \Delta M / \Delta \kappa. \quad (\text{F-8})$$

### F-3.2 Extended Calculated Information within the Context of CIRFT

In addition to the basic information discussed in Section F-3.1, other parameters of interest are developed to study the effect of particular rod characteristics on the fatigue.

SNF fuel rods are heterogeneous. Although the geometry of the irradiated rod can be estimated, it varies based on rod type, manufacture, and operation. The irradiated rod contains cracked pellets (some with HBU rims), an inner cladding oxide layer, potentially a layer of pellet bonded with the cladding ID, cladding with radiation-induced flaws, and an outer cladding oxide layer that is potentially discontinuous due to spalling. Axially, the fuel column is not continuous; it is composed of numerous short pellets. Although there could be some bonding between pellet ends as a result of an in-reactor diffusion bonding or galling process, the contacting surface areas are small as a result of the pellet chamfers and dishes, and the pellet-pellet bonding is not expected to be strong. Given these conditions, an SNF rod is far from an

ideal homogeneous material, and the idealized treatment described in previous sections is not completely accurate.

To improve understanding of the rod's performance, some of these heterogeneous effects on fatigue lifetime were explored by mining the CIRFT data, including: (1) pellet-pellet and pellet-cladding bonding rod stiffening, (2) discontinuities in cladding support conditions at pellet-pellet interfaces, (3) cladding hydride reorientation, and (4) effects of the heat treatment applied to three of the SNF rods tested, as described in the following subsections.

### F-3.2.1 Pellet Bonding Stiffening

Although the CIRFT data do not allow for separate effects testing, the measured flexural rigidity data can be trended to look for sudden shifts that could indicate pellet-pellet and pellet-cladding debonding. Results from previous testing [F-4, F-5] indicate that pellet-pellet bonding is relatively weak and likely becomes debonded after only a few CIRFT cycles. However, the pellet-cladding bond is expected to be stronger than the pellet-pellet bond. For cases in which the rod was operated in-reactor at high temperature and power, a chemical bond may be developed between the pellet OD and the cladding inner diameter (ID). Wang and Wang proposed a dual flexural rigidity (i.e., before and after the bond is disrupted) with a bonding efficiency that can be applied in rod mechanical performance modeling.

### F-3.2.2 Discontinuous Cladding Support

Although the LVDTs used on the CIRFT device only measure the gross rod deflection within the gauge section, several pellet lengths with several pellet-pellet interfaces are included in the gauge section, and any effects related to the pellet-pellet interfaces are embedded in the CIRFT data. As observed in previous test results, fractures are typically located at the pellet-pellet interfaces, which is consistent with the reduced mechanical cross section and potential interaction between the pellet end and cladding at those locations during bending. This is described by Wang and Wang as a fuel pellet “pinning” effect, as illustrated in Figure F-6.

Although it is unlikely that the localized effect can be observed in the CIRFT data, Wang and Wang investigated the effects on the cladding using finite element analysis (FEA) and found that the localized strain in the cladding at the pellet-pellet-cladding interface region is three to four times higher than that in regions supported by the body of the fuel pellet. This is caused by (1) the interaction of the pellet end with the cladding, and (2) the localized axial tension that is applied as the gap is opened.

Wang and Wang further explored the shift in the neutral axis that occurs during pinning. The neutral axis shifts constantly with each cycle, but the maximum strain still occurs at the outer radius of the cladding.

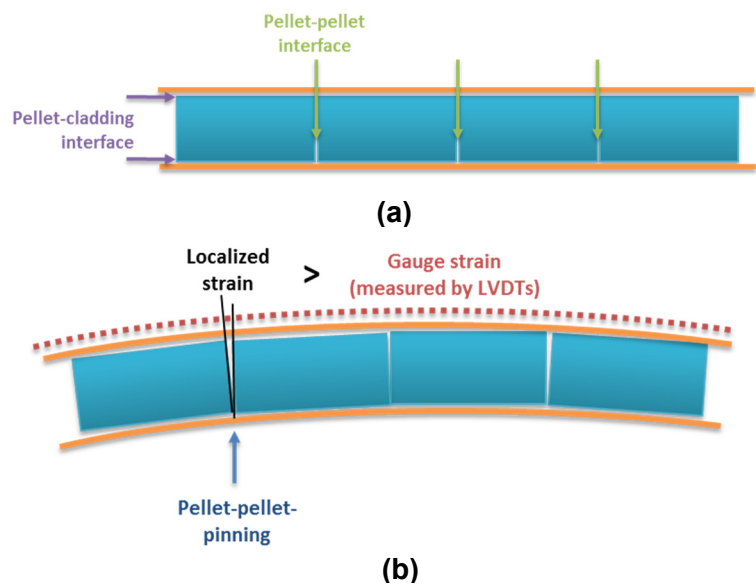


Figure F-6. Cladding and pellet stack (a) in the neutral position and (b) in bending. [F-5].



### **F-3.2.3 Cladding Hydride Reorientation Effects**

Hydrogen taken up by the fuel rod cladding in-reactor can be detrimental to performance when the hydrogen concentration exceeds the alloy's solubility and zirconium hydride platelets are precipitated within the cladding. Wang and Wang completed four CIRFT tests with cladding hydrides that had been purposely reoriented from circumferential to radial; however, a large difference in performance was not observed in fatigue lifetime, and no definitive conclusions could be made.

The sister rod tests provide additional insight with comparisons between heat-treated rods and baseline rods. However, not all sister rod heat treatments resulted in reoriented hydrides, because they were treated at more realistic temperature and cladding stress conditions. A description of the heat treatments and the degree of reorientation are provided in Appendices A and B.

### **F-3.2.4 Cladding Irradiation Defect Annealing**

During reactor operation, the cladding is hardened and embrittled through the accumulation of irradiation defects. The baseline sister rods were tested in the as-received condition, and three rods were heat-treated to subject them to the potential for irradiation defect annealing.

### **F-3.2.5 Normal Condition Impacts**

Impacts to the fuel rod are expected to reduce fatigue lifetime because (1) they are expected to disrupt pellet-pellet bonds and pellet-cladding bonds at the impact site, thus leading to a reduced flexural rigidity, (2) the rod's flexural rigidity determines the total deflection of the rod in bending, and (3) a low flexural rigidity results in larger deflections and a corresponding higher stress and strain. Thus, it is postulated that normal condition impacts could reduce the fatigue lifetime of the SNF rods.

Previous testing by Wang and Wang included non-normal impacts from a drop height of 12 in. with indeterminant results that were on the low side of the existing dataset. Future testing is expected to explore this effect with a more controlled impact method.

## F-4. Comparison Data Available from Previous ORNL Tests

The NRC funded the development of the CIRFT and performed testing on HBU SNF with Zircaloy-4 (Zirc-4) and M5 cladding from pressurized water reactors (PWRs) and Zircaloy-2 (Zirc-2) from boiling water reactors (BWRs). Fifty-three cyclic fatigue tests in a range of load amplitudes were performed on PWR rod segments, and 17 tests were performed on BWR rod segments. The burnup of the tested rod segments ranged between 45 and 67 GWd/MTU. The oxide layer thickness on the waterside surface of each segment was not specifically measured but was estimated to be between 20 to 110  $\mu\text{m}$ , with a corresponding estimated hydrogen concentration of 110–800 wppm. Wang and Wang completed four CIRFT tests in which the cladding hydrides were reoriented by pressurizing the segment and applying a thermal transient to determine whether the radial hydrides reduced the fatigue lifetime. The basic data from these tests are directly comparable with the sister rod test results and are summarized in Table F-1 [F-4].

**Table F-1. Reference Dynamic Dataset [F-4].**

Rod type	Cladding material	Parent rod-average burnup (GWd/MTU)	Test ID	Cycles to failure	Average moment (N-m)	Maximum cladding stress <sup>d</sup> (MPa)	Maximum average stress <sup>e</sup> (MPa)	Maximum average strain (%)	Flexural rigidity (N-m <sup>2</sup> )
15x15	Zirc-4	67	Demo1	4.0E+03	28.5	456	233	0.51	30.2
15x15	Zirc-4	67	Dcal <sup>c</sup>	9.6E+03	28.6	366	234	0.41	37.9
15x15	Zirc-4	67	DL2H	1.8E+03	34.1	362	279	0.40	45.6
15x15	Zirc-4	67	S1 <sup>c</sup>	4.6E+03	28.5	327	233	0.36	42.3
15x15	Zirc-4	67	S2 <sup>c</sup>	7.2E+03	28.3	318	231	0.35	43.3
15x15	Zirc-4	67	DH3	7.1E+03	33.7	282	276	0.31	57.9
15x15	Zirc-4	67	R1	5.5E+03	29.0	227	237	0.25	61.9
15x15	Zirc-4	67	S3 <sup>c</sup>	2.5E+04	24.1	214	197	0.24	54.8
15x15	Zirc-4	67	DH2	6.5E+04	18.9	170	155	0.19	53.9
15x15	Zirc-4	67	DL1	1.1E+05	14.1	104	115	0.12	65.6
15x15	Zirc-4	67	DH1	2.5E+05	11.6	99	95	0.11	56.7
15x15	Zirc-4	67	S5	1.8E+05	11.6	84	95	0.09	66.4
15x15	Zirc-4	67	R3	1.3E+05	12.6	73	103	0.08	82.6
15x15	Zirc-4	67	R2	3.9E+05	10.0	70	82	0.08	69.3
15x15	Zirc-4	67	DL3	1.0E+06	9.2	60	75	0.07	73.4
15x15	Zirc-4	67	DM2	2.3E+06	8.2	56	67	0.06	71.9
15x15	Zirc-4	67	R4	2.7E+05	7.8	54	64	0.06	70.0
15x15	Zirc-4	67	HR1 <sup>a</sup>	4.2E+04	15.2	207	124	0.28	29.3
15x15	Zirc-4	67	HR2 <sup>a,c</sup>	9.5E+03	14.7	191	120	0.26	31.6
15x15	Zirc-4	67	HR4 <sup>a</sup>	5.5E+04	14.8	158	121	0.21	37.5
15x15	Zirc-4	67	HR3 <sup>a</sup>	2.4E+05	9.0	107	74	0.14	33.6
15x15	Zirc-4	67	DM3	1.3E+07 <sup>b</sup>	7.7	51	63	0.06	73.8
15x15	Zirc-4	67	DM1	1.1E+07 <sup>b</sup>	6.7	44	55	0.05	75.6
15x15	Zirc-4	67	R5	2.2E+07 <sup>b</sup>	6.6	42	54	0.05	76.3
15x15	Zirc-4	67	DL2	6.4E+06 <sup>b</sup>	4.2	22	34	0.03	91.5
17x17	M5	45	TH5	2.8E+04	11.2	312	129	0.32	16.6
17x17	M5	45	TH6	1.3E+04	13.4	308	154	0.32	20.1
17x17	M5	45	MOX17	1.2E+04	11.1	266	128	0.28	19.3

<sup>a</sup> The specimens were pressurized and subjected to a thermal transient to induce cladding hydride reorientation prior to conducting the unpressurized CIRFT test.

<sup>b</sup> The test was discontinued without specimen fracture.

<sup>c</sup> Samples were tested statically prior to dynamic testing.

<sup>d</sup> Stress calculated using the modified equivalent stress approach in Reference [F-4] to represent the cladding surface stress

<sup>e</sup> Stress calculated using the equivalent stress approach per Eq. (F-7) where fuel rod OD for 15x15, 17x17 and 9x9 fuel rods are 10.76 mm, 9.6 mm and 11.43 mm, respectively [F-21], meaning  $I_{15x15} = 6.58\text{E-}10 \text{ m}^4$ ,  $I_{17x17} = 4.2\text{E-}10 \text{ m}^4$ , and  $I_{9x9} = 8.34\text{E-}10 \text{ m}^4$ .

Table F-1. Reference Dynamic Dataset [F-4] (continued).

Rod type	Cladding material	Parent rod-average burnup (GWd/MTU)	Test ID	Cycles to failure	Average moment (N-m)	Maximum cladding stress (MPa)	Maximum average stress <sup>e</sup> (MPa)	Maximum average strain (%)	Flexural rigidity (N-m <sup>2</sup> )
17x17	M5	45	TH3	1.5E+04	10.6	264	122	0.27	18.5
17x17	M5	45	TH2	5.7E+04	11.0	255	127	0.14	20.1
17x17	M5	45	MOX14	8.7E+04	6.2	254	71	0.26	11.3
17x17	M5	45	MOX7	1.6E+04	13.9	239	160	0.25	26.9
17x17	M5	52	NA7	1.3E+04	13.5	232	155	0.30	27.1
17x17	M5	45	MOX8	1.3E+04	11.0	206	127	0.21	24.9
17x17	M5	45	TH1	5.7E+04	8.8	204	101	0.21	19.9
17x17	M5	52	NA1	1.6E+04	11.0	194	127	0.25	26.2
17x17	M5	45	MOX13	2.7E+04	8.7	171	100	0.18	23.6
17x17	M5	45	MOX15	2.0E+04	8.5	167	98	0.17	23.5
17x17	M5	45	MOX2	3.7E+04	8.5	161	98	0.17	24.3
17x17	M5	45	MOX12	4.2E+04	8.7	158	100	0.16	25.6
17x17	M5	45	TH4	2.5E+06	6.3	151	73	0.16	19.2
17x17	M5	52	NA2	2.2E+04	8.8	149	101	0.19	27.4
17x17	M5	45	MOX10	3.9E+04	8.7	144	100	0.15	28.2
17x17	M5	45	MOX11	4.2E+04	8.7	142	100	0.15	28.1
17x17	M5	45	MOX9	9.0E+04	6.3	121	73	0.13	24.0
17x17	M5	52	NA4	6.1E+04	6.3	84	73	0.11	35.0
17x17	M5	45	MOX16	3.7E+03	13.2	374	152	0.39	16.3
17x17	M5	45	MOX5	4.5E+05	4.8	68	55	0.07	32.6
17x17	M5	45	MOX6	5.4E+05	3.8	64	44	0.07	27.6
17x17	M5	45	MOX4	2.2E+06	3.9	50	45	0.05	36.1
17x17	M5	52	NA6	4.3E+05	4.0	46	46	0.06	40.3
17x17	M5	45	TH2	3.8E+06 <sup>b</sup>	6.2	134	71	0.14	21.6
17x17	M5	52	NA5	5.1E+06 <sup>b</sup>	4.0	54	46	0.07	34.0
9x9	Zirc-2	57	LM1 <sup>c</sup>	9.4E+03	23.4	386	160	0.42	31.7
9x9	Zirc-2	57	LM17	1.3E+04	28.1	365	192	0.40	40.1
9x9	Zirc-2	57	LM16	1.4E+04	28.6	280	195	0.31	53.3
9x9	Zirc-2	57	LM13	2.1E+04	21.4	228	146	0.25	49.0
9x9	Zirc-2	57	LM10	5.2E+04	18.9	210	129	0.23	47.0
9x9	Zirc-2	57	LM7	1.2E+05	13.9	149	95	0.16	48.9
9x9	Zirc-2	57	LM2	1.7E+05	11.5	114	78	0.12	52.6
9x9	Zirc-2	57	LM3	4.9E+05	9.0	104	61	0.11	45.3
9x9	Zirc-2	57	LM15	4.4E+05	9.0	96	61	0.11	48.6
9x9	Zirc-2	57	LM9	7.3E+05	9.1	92	62	0.10	51.2
9x9	Zirc-2	57	LM14	3.9E+05	9.0	85	61	0.09	55.9
9x9	Zirc-2	57	LM5	2.5E+05	7.6	71	52	0.08	56.1
9x9	Zirc-2	57	LM11	3.6E+05	7.7	69	53	0.08	57.6
9x9	Zirc-2	57	LM6	1.8E+06	6.5	66	44	0.07	51.5
9x9	Zirc-2	57	LM8	4.7E+06	6.6	55	45	0.06	62.9
9x9	Zirc-2	57	LM12	7.6E+06 <sup>b</sup>	6.1	88	42	0.10	36.3
9x9	Zirc-2	57	LM17	3.4E+06 <sup>b</sup>	7.5	87	51	0.10	44.7

<sup>a</sup> The specimens were pressurized and subjected to a thermal transient to induce cladding hydride reorientation prior to conducting the unpressurized CIRFT test.

<sup>b</sup> The test was discontinued without specimen fracture.

<sup>c</sup> Samples were tested statically prior to dynamic testing.

<sup>d</sup> Stress calculated using the modified equivalent stress approach in Reference [F-4] to represent the cladding surface stress

<sup>e</sup> Stress calculated using the equivalent stress approach per Eq. (F-7) where fuel rod OD for 15x15, 17x17 and 9x9 fuel rods are 10.76 mm, 9.6 mm and 11.43 mm, respectively [F-21], meaning  $I_{15x15} = 6.58E-10 \text{ m}^4$ ,  $I_{17x17} = 4.2E-10 \text{ m}^4$ , and  $I_{9x9} = 8.34E-10 \text{ m}^4$ .

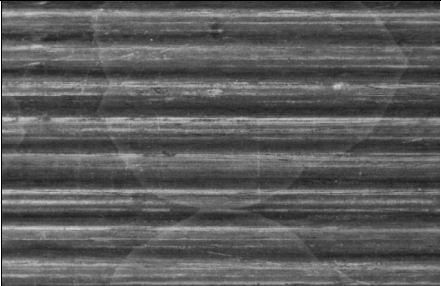
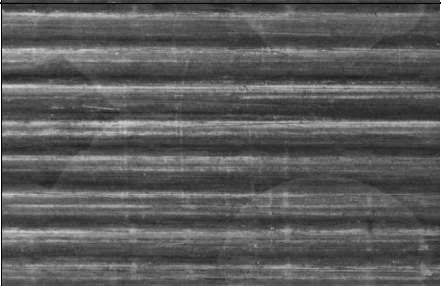

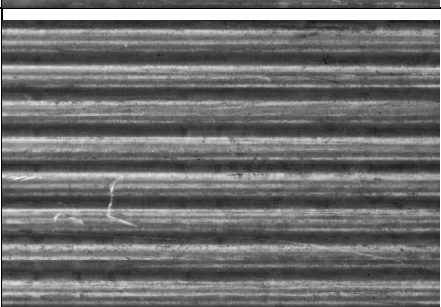
## F-5. Description of the Sister Rods Tested

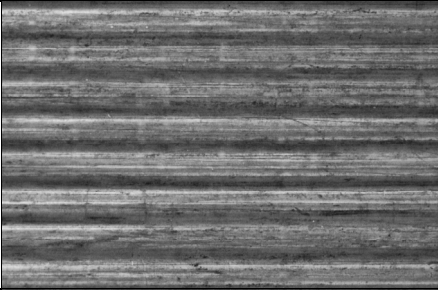
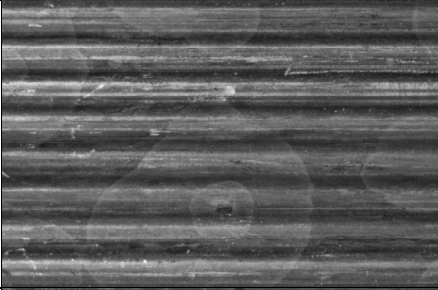
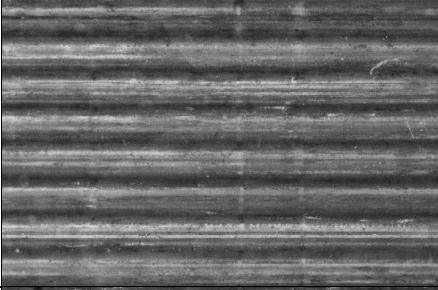

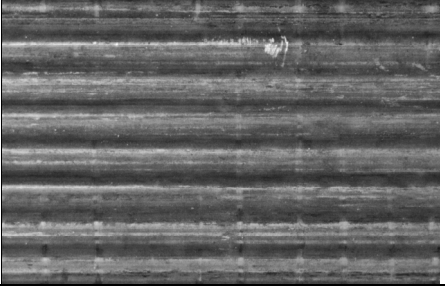
Additional descriptions of the rods used in these tests are provided in the sister rod test plan [F-3] and the nondestructive test results [F-6]. All rods were operated by Dominion Energy at the North Anna Power Station to high rod average burnup ( $>45$  GWd/MTU). Table F-2 summarizes the parent assembly operation and lattice location for the rods test using CIRFT.

In Phase 1 of the sister rod test program [F-1, F-2], seven of ORNL's 15 sister rods were selected for paired testing: one baseline fuel rod and one heat-treated fuel rod of each cladding type (M5, ZIRLO, and Zirc-4/LT-Zirc-4), plus an extra ZIRLO-clad rod for additional datapoints, because no ZIRLO-clad rods were tested in previous campaigns. Baseline rods are tested in the condition in which they were received at ORNL, and full-length heat-treatment (FHT) rods are subjected to a thermal transient before testing, as described in Appendix A, to simulate dry storage conditions. Three full-length fuel rods have been heat-treated to date—one Zirc-4-clad (F35P17), one ZIRLO-clad (3F9N05), and one M5-clad (30AE14)—and the results from the heat-treated rods were compared with the results from the baseline rods to determine whether the fatigue lifetime is affected by dry storage thermal transients.

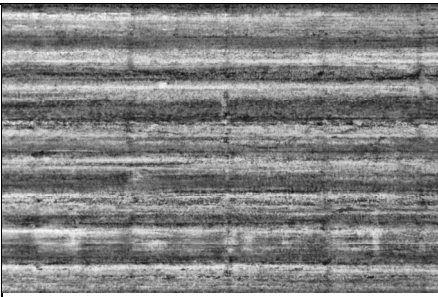
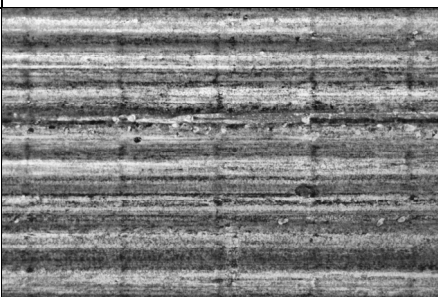
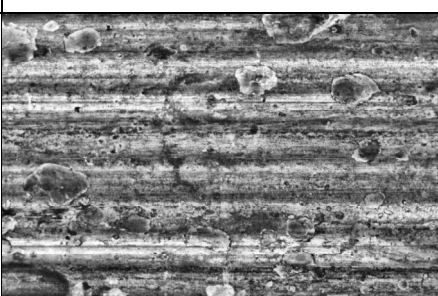
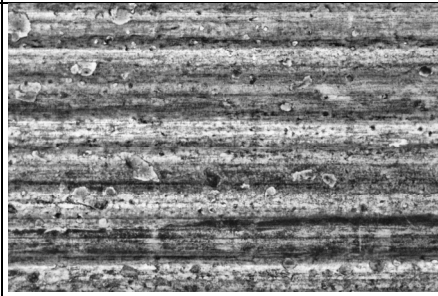
The CIRFT uses specimens that are 152.4 mm (6 in.) long that were taken from various elevations along the SNF rods. Because rod burnup varies as a function of elevation, the rod average burnup is used in conjunction with the gamma scans of the rod [F-6] to estimate the average burnup of the CIRFT segment, as listed in Table F-2. Full-circumference flattened images—as defined in nondestructive examination (NDE) report [F-6]—of the pretest waterside surface condition of the CIRFT segments are also provided in Table F-2.

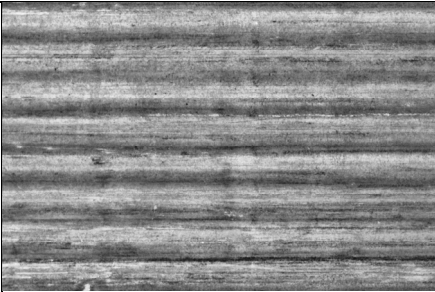
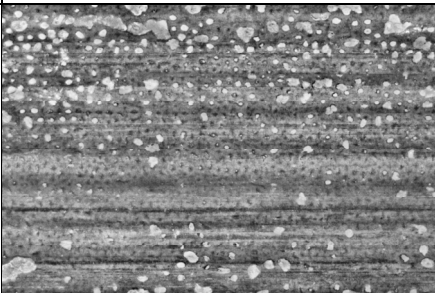
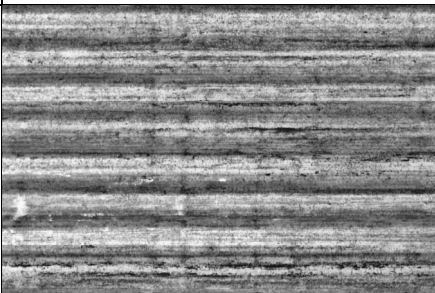
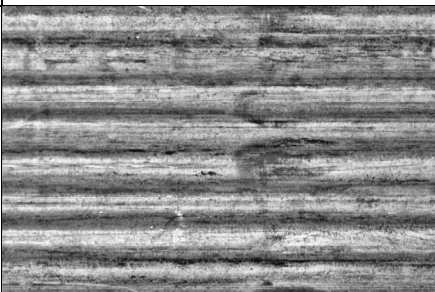
Table F-2. Sister rod segments selected for CIRFT.

Clad material	Donor assembly	Sister rod lattice location	Assembly average burnup (GWd/MTU)	Rod average burnup (GWd/MTU)	Heat treatment applied to the rod	Measured rod internal pressure (MPa)	Measured rod void volume (cc)	Specimen lower elevation (mm)	Specimen upper elevation (mm)	Average specimen burnup (GWd/MTU)	Rod 360° appearance near the CIRFT gauge section pretest
The M5-clad rods exhibited very light waterside oxide that is visible as irregular, somewhat circular patches, with some areas including an interior patch that appears to have peeling oxide. Grid-to-rod-fretting (GTRF) marks are visible in some grid elevations, along with rod removal scratches.											
M5	30A	D05	52.0	54	No	3.46	10.63	697	850	58	
	30A	D05	52.0	54	No	3.46	10.63	2,050	2,203	59	
	30A	D05	52.0	54	No	3.46	10.63	2,630	2,783	59	
	30A	D05	52.0	54	No	3.46	10.63	3,732	3,886	24	 Pellet-pellet gaps throughout

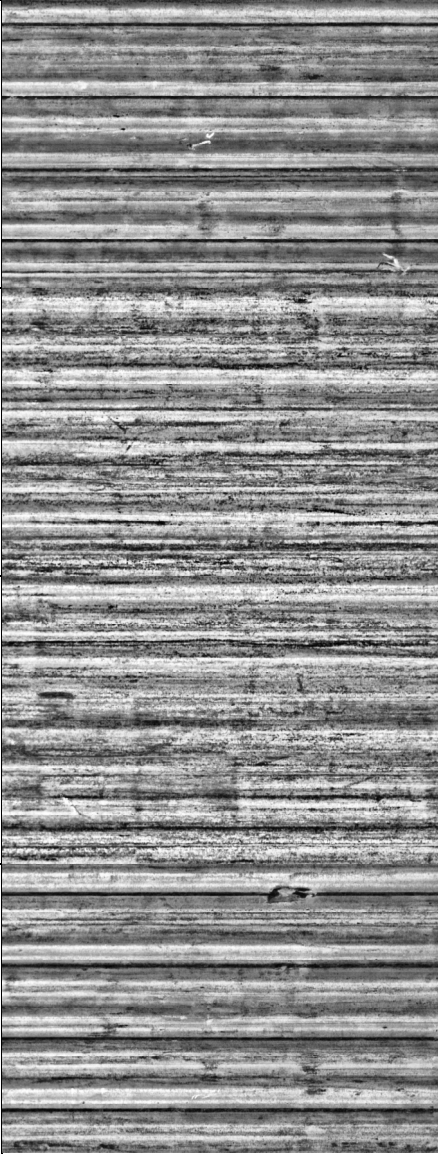
Clad material	Donor assembly	Sister rod lattice location	Assembly average burnup (GWd/MTU)	Rod average burnup (GWd/MTU)	Heat treatment applied to the rod	Measured rod internal pressure (MPa)	Measured rod void volume (cc)	Specimen lower elevation (mm)	Specimen upper elevation (mm)	Average specimen burnup (GWd/MTU)	Rod 360° appearance near the CIRFT gauge section pretest
M5	30A	D05	52	54	No	3.46	10.63	3,452	3,605	38	
	30A	E14	52	54	Yes	3.22	10.99	672	825	56	
	30A	E14	52	54	Yes	3.22	10.99	2,850	3,003	60	
	30A	E14	52	54	Yes	3.22	10.99	3,156	3,309	56	
	30A	E14	52	54	Yes	3.22	10.99	3,003	3,156	58	

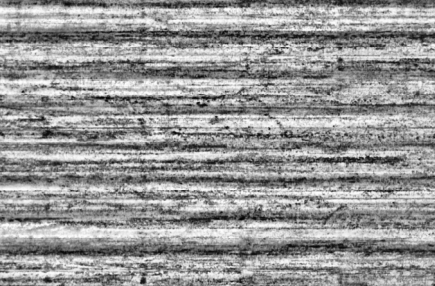
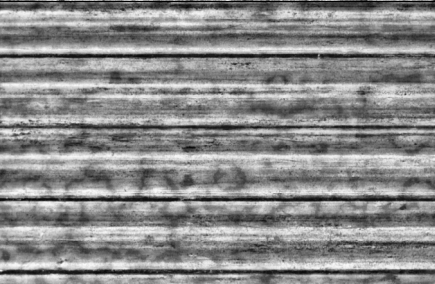
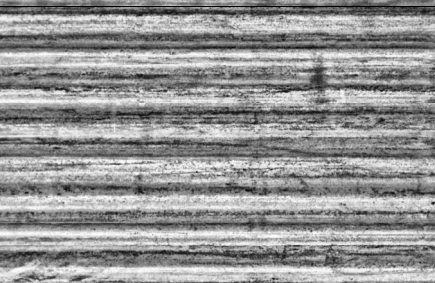
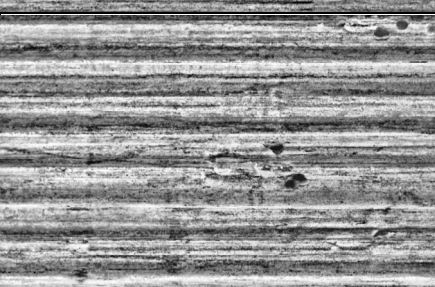
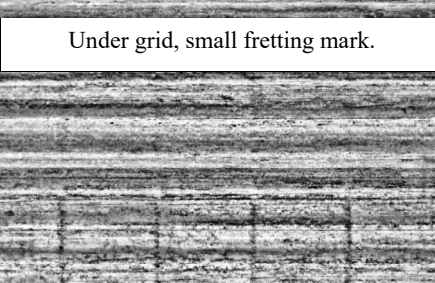


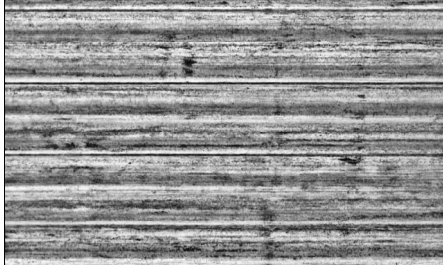
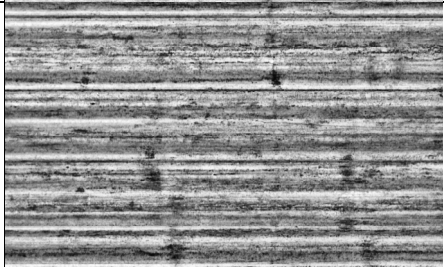

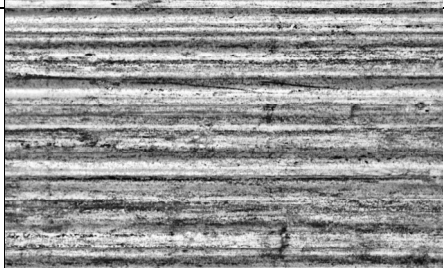
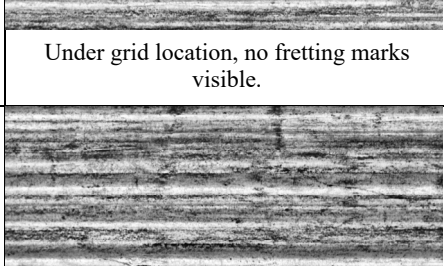
Clad material	Donor assembly	Sister rod lattice location	Assembly average burnup (GWd/MTU)	Rod average burnup (GWd/MTU)	Heat treatment applied to the rod	Measured rod internal pressure (MPa)	Measured rod void volume (cc)	Specimen lower elevation (mm)	Specimen upper elevation (mm)	Average specimen burnup (GWd/MTU)	Rod 360° appearance near the CIRFT gauge section pretest
Assemblies 3A1 and F35 (Zirc-4 / LT Zirc-4 cladding types) appeared to have the greatest amount of oxide buildup/spalling among the sister rods. No visible signs of through-wall damage or large areas of clad degradation were found, but some areas of significant oxidation have a flake-like appearance, and spalling is evident at some elevations. Some shallow GTRF marks are visible, and some features that appear to be GTRF marks oxidized in later cycles are visible.											
LT Zirc-4	3A1	F05	50	51	No	3.73	12.94	1,853	2,006	56	
	3A1	F05	50	51	No	3.73	12.94	2,025	2,178	56	
	3A1	F05	50	51	No	3.73	12.94	3,214	3,367	48	 Under grid location, no fretting marks visible.
	3A1	F05	50	51	No	3.73	12.94	3,367	3,520	44	

Clad material	Donor assembly	Sister rod lattice location	Assembly average burnup (GWd/MTU)	Rod average burnup (GWd/MTU)	Heat treatment applied to the rod	Measured rod internal pressure (MPa)	Measured rod void volume (cc)	Specimen lower elevation (mm)	Specimen upper elevation (mm)	Average specimen burnup (GWd/MTU)	Rod 360° appearance near the CIRFT gauge section pretest
Assemblies 3A1 and F35 (Zirc-4 / LT Zirc-4 cladding types) appeared to have the greatest amount of oxide buildup/spalling among the sister rods. No visible signs of through-wall damage or large areas of clad degradation were found, but some areas of significant oxidation have a flake-like appearance and spalling is evident at some elevations. Some shallow GTRF marks are visible, and some features that appear to be GTRF marks that have oxidized in later cycles are visible.											
Zirc-4	F35	P17	58	60	Yes	4.68	13.32	2,027	2,180	52	
	F35	P17	58	60	Yes	4.68	13.32	1,855	2,008	53	
	F35	P17	58	60	Yes	4.68	13.32	3,159	3,312	47	
	F35	P17	58	60	Yes	4.68	13.32	3,312	3,465	43	



Clad material	Donor assembly	Sister rod lattice location	Assembly average burnup (GWd/MTU)	Rod average burnup (GWd/MTU)	Heat treatment applied to the rod	Measured rod internal pressure (MPa)	Measured rod void volume (cc)	Specimen lower elevation (mm)	Specimen upper elevation (mm)	Average specimen burnup (GWd/MTU)	Rod 360° appearance near the CIRFT gauge section pretest
The ZIRLO-clad rods have a moderate-to-heavy oxide layer, with some oxide peeling observed. GTRF marks are present on most rods and range in severity from shallow to deep. No visible signs of through-wall cladding damage were observed. Darker regions are present at grid elevations, indicating either CRUD or possibly a thinner oxidation layer (attributed to better heat transfer in those areas resulting from flow turbulence).											
ZIRLO	3D8	E14	55	59	No	4.18	11.73	719	872	64	
	3D8	E14	55	59	No	4.18	11.73	2,412	2,565	64	
	3D8	E14	55	59	No	4.18	11.73	2,963	3,116	62	
	3D8	E14	55	59	No	4.18	11.73	1,178	1,331	63	
											Under grid location, GTRF mark aligned at maximum strain location

Clad material	Donor assembly	Sister rod lattice location	Assembly average burnup (GWd/MTU)	Rod average burnup (GWd/MTU)	Heat treatment applied to the rod	Measured rod internal pressure (MPa)	Measured rod void volume (cc)	Specimen lower elevation (mm)	Specimen upper elevation (mm)	Average specimen burnup (GWd/MTU)	Rod 360° appearance near the CIRFT gauge section pretest
ZIRLO	3D8	E14	55	59	No	4.18	11.73	3,225	3,378	56	
	3F9	N05	52	54	Yes	3.98	12.74	719	872	59	
	3F9	N05	52	54	Yes	3.98	12.74	2,329	2,482	59	
	3F9	N05	52	54	Yes	3.98	12.74	2,710	2,863	57	
	3F9	N05	52	54	Yes	3.98	12.74	3,440	3,593	45	

Clad material	Donor assembly	Sister rod lattice location	Assembly average burnup (GWd/MTU)	Rod average burnup (GWd/MTU)	Heat treatment applied to the rod	Measured rod internal pressure (MPa)	Measured rod void volume (cc)	Specimen lower elevation (mm)	Specimen upper elevation (mm)	Average specimen burnup (GWd/MTU)	Rod 360° appearance near the CIRFT gauge section pretest
ZIRLO	6U3	K09	53	55	no	3.64	11.78	2,310	2,463	59	
	6U3	K09	53	55	no	3.64	11.78	2,463	2,616	59	
	6U3	K09	53	55	no	3.64	11.78	2,635	2,788	58	
	6U3	K09	53	55	no	3.64	11.78	3,200	3,353	50	
	6U3	K09	53	55	no	3.64	11.78	3,353	3,506	46	

## F-6. Selection of CIRFT Test Conditions

In specifying the loading conditions for the CIRFT tests, the previous data for M5 and Zirc-4 clad fuel rods were surveyed [F-4,F-5] and several objectives were identified for the sister rod tests:

- Demonstrate that M5 and Zirc-4 clad sister rod fatigue performance is consistent with the data given in the established database for those cladding alloys
- Demonstrate whether FHT changes the fatigue lifetime of the cladding/rod when compared with non-FHT segments
- Demonstrate whether GTRF marks result in a reduced fatigue lifetime when they are aligned with the point of peak cladding deflection during the test
- Establish a range of tests for rods that have ZIRLO cladding consistent with the data given in the established database for other cladding alloys and demonstrate whether the ZIRLO-clad rods are consistent with other rods

The sister rods are tested statically and dynamically as paired samples with similar burnup and oxide thicknesses.

- a. **Baseline rod specimens:** one specimen tested statically followed by a dynamic test at a relatively high load (~175 N-m), one specimen tested dynamically at a moderate load (~10–12 N-m), and one specimen tested dynamically at a low load (~5–6 N-m)
- b. **Heat-treated rod specimens:** one specimen tested statically followed by a dynamic test at the same load used for the baseline specimen, one specimen tested dynamically at the same moderate load used for the baseline specimen, and one specimen tested dynamically at the same low load used for the baseline specimen

Table F-3 lists the selected test type, test load, and paired specimens.



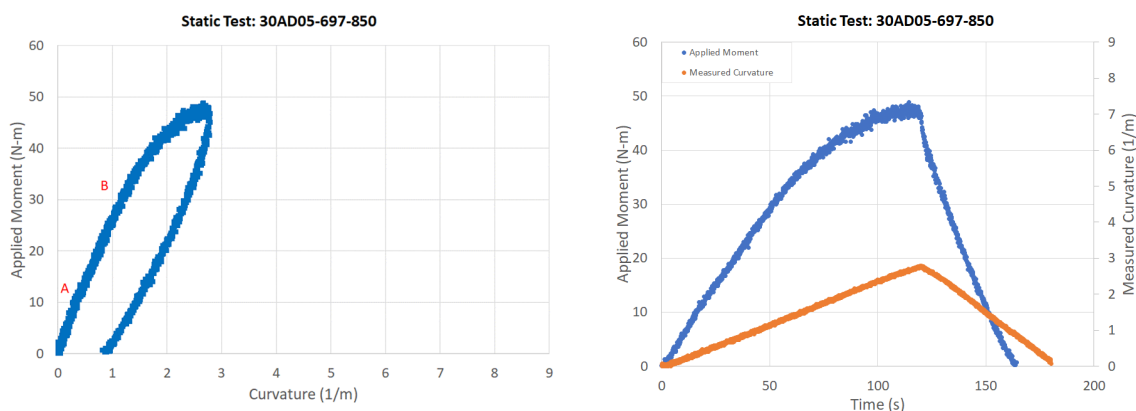
Table F-3. CIRFT specimen and test pairing

Baseline specimens					Heat-treated specimens							
Specimen ID		Cladding type	Estimated specimen average burnup (GWd/MTU)		Specimen ID		Cladding type	Estimated specimen average burnup (GWd/MTU)		Test Type	Nominal test moment applied (N-m)	Notes
30AD05	0697	0850	M5	58	30AE14	0672	0825	M5	56	Static followed by Dynamic	17.8	---
30AD05	2050	2203		59	30AE14	3156	3309		56	Dynamic	6.1	---
30AD05	2630	2783		59	30AE14	2850	3003		60	Dynamic	12.2	---
30AD05	3732	3886		24						Dynamic	--	pellet-pellet gaps – not yet tested
30AD05	3452	3605	M5	38	30AE14	3003	3156	M5	58	Cumulative	--	Future test
3A1F05	1853	2006	LT Zirc-4	56	F35P17	1855	2008	Zirc-4	53	Static followed by Dynamic	17.8	---
3A1F05	3367	3520		44	F35P17	2027	2180		52	Dynamic	5.1	Replacement; originally allocated as a cumulative test specimen
3A1F05	2025	2178		56						Dynamic	10.2	Originally allocated for 5.1 N-m, but mistakenly tested at 10.2 N-m
3A1F05	3214	3367		48	F35P17	3159	3312		47	Dynamic	10.2	
					F35P17	3312	3465	Zirc-4	43	Cumulative	--	Future test
3D8E14	0719	0872	ZIRLO	64	3F9N05	719	872	ZIRLO	59	Static followed by Dynamic	17.8	---
3D8E14	2412	2565		64	3F9N05	2329	2482		59	Dynamic	6.1	---
3D8E14	2963	3116		62	3F9N05	2710	2863		57	Dynamic	10.2	---
3D8E14	1178	1331		63						Dynamic	6.1	---
6U3K09	2310	2463		59						Dynamic	14.3	Additional higher load data point
6U3K09	2463	2616		59						Dynamic	10.2	Provides a good comparison with 3F9N05-2710-2863 based on segment burnup
6U3K09	2635	2788		58						Dynamic	7.6	Provides a good comparison with 3F9N05-2329-2482 based on segment burnup
6U3K09	3200	3353		50						Dynamic	10.2	Provides a comparison with 3F9N05-2710-2863 based on segment burnup
6U3K09	3353	3506		46						Dynamic	13.3	Additional higher load data point
3D8E14	3225	3378	ZIRLO	56	3F9N05	3440	3593	ZIRLO	45	Cumulative	--	Future test

## F-7. Test Results

### F-7.1 Static Tests

The static test is performed to measure the range of flexure of representative specimens for each sister rod cladding type: M5, ZIRLO, and Zirc-4 or LT Zirc-4. Six specimens—one of each cladding type and heat treatment—were tested in static mode to measure the flexural rigidity before testing the fatigue response in dynamic mode. An example of the data typically acquired is shown in Figure F-7; all were flexed beyond the knee in the curve, which is labeled as point B in Figure F-7(a). The static flexural rigidity is calculated on the linear portion of the curve from approximately points A to B; this is consistent with the definition of EI2 in Reference [F-20].



(a) Applied moment as a function of the measured curvature

(b) Applied moment and measured curvature as a function of time

**Figure F-7. The static test data for 30AD05-0697-0850 represent the typical result**

A deep investigation of the static test data revealed that specimen F35P17-1855-2008 failed during the static test. Rod F35P17 is a Zirc-4 clad rod that was heat treated prior to CIRFT testing. During the static test, there was an observed drop in the applied moment that correlated with an increase in the measured curvature. In addition, in subsequent dynamic fatigue testing the measured applied moment was lower than expected based on the measured flexural rigidity before failure. There are indications of oxide spalling on the specimen tested (see Figure F-25), which may have contributed to the failure of the rod. Based on these observations, the only data from the static test considered valid for this specimen is the pre-failure static flexural rigidity, which is reported in Table F-4; subsequent dynamic test data are not valid and are not to be included in the reported CIRFT dataset.

During the static tests of 30AE14-0672-0825 and 3D8E14-0719-0872, the LVDTs were not responding as expected, appearing to be stuck at times, and they did not provide consistent curvature or rigidity information. Therefore, data from these static tests are not reported in Table F-4.

The results of the remaining valid static tests are provided in Table F-4 with a comparison of the flexural rigidity results from the dynamic tests (Section F-7.2). Generally, the dynamically measured A-B rigidity of the statically-tested specimens should be lower than the statically measured rigidity because the rod is usually flexed past the yield point during the static test. This was observed in the 3 samples that had valid rigidity measurements in both the static and dynamic tests (30AD05-0697-0850, 3A1F05-1853-2006 and 3F9N05-0719-0872), though in two cases the difference is within the measurement uncertainty.

**Table F-4. Static test results.**

Cladding material	Heat-treated?	Estimated specimen-average burnup (GWd/MTU)	Specimen ID	Maximum Applied Moment (N-m)	Applied moment from A to B (N-m)	Flexural rigidity in A to B region (N-m <sup>2</sup> )	Dynamically applied moment (N-m) <sup>a</sup>	Dynamically measured flexural rigidity (after static flexure) (N-m <sup>2</sup> ) <sup>a</sup>
M5	No	58	30AD05-0697-0850	47.4	11.1-30.9	23.7 ± 7.8	15.8	15.6 ± 1.2
M5	Yes	56	30AE14-0672-0825	Not reported due to data acquisition issue			15.55	20.5 ± 4.2
LT Zirc-4	No	56	3A1F05-1853-2006	49.8	16.0 – 35.4	20.3 ± 6.5	15.92	19.3 ± 3.9
Zirc-4	Yes	66	F35P17-1855-2008	Not reported due to data acquisition issue	8.8 – 24.8	20.6 ± 7.2	N/A <sup>c</sup>	N/A <sup>c</sup>
ZIRLO	No	64	3D8E14-0719-0872	Not reported due to data acquisition issue			15.3	18.4 <sup>b</sup>
ZIRLO	Yes	59	3F9N05-0719-0872	46.6	17.2 to 31.9	21.9 ± 9.2	15.53	18.0 ± 3.6

<sup>a</sup> Data are discussed in Section F-7.2.

<sup>b</sup> Because of invalid curvature measurement, the flexural rigidity is estimated as the average of other four measurements.

<sup>c</sup> Specimen failed in static test.

## F-7.2 Dynamic Tests

All Phase 1 CIRFT dynamic tests were completed except for one sample with pellet-to-pellet gaps. Six specimens were cycled in static mode before being tested dynamically, a process is referred to as *static/dynamic testing*. The results from the static/dynamic tests are not strictly comparable with the other tests since some changes in the rod condition may have occurred during the static test. The CIRFT fatigue data (applied moment, cycles to failure, maximum strain amplitude, maximum stress amplitude as discussed in Section F-3.1), maximum cladding stress amplitude (based on the modified equivalent stress approach in [F-4]), and dynamic flexural rigidity are provided in Table F-5.

Figure F-8 plots the applied bending moment, with the number of cycles to failure measured for completed tests with the available previous data [F-4, F-5]. The stress and strain amplitudes can be plotted as functions of the number of cycles to failure to map the fatigue limits of the composite rods. Figure F-9 plots the strain amplitude as a function of the number of cycles to failure for tests where an extended analysis of the test data is available. The stress amplitude based on the composite rod maximum stress, per Eq. (F-7), is plotted as function of cycles to failure in Figure F-10 and the maximum cladding stress amplitude is plotted as a function of cycles to failure in Figure F-11. Except for outliers 3A1F05-3214-3367 and F35P17-3159-3312, the results are consistent with previous data for the same size of fuel rods (17×17), although when trended with stress, the sister rod fatigue lifetime is on the lower side of other lifetime estimates [F-9, F-10, F-11]. Some data are below the O'Donnell-Langer fatigue curve [F-9], as shown in Figure F-10 and Figure F-11. However, some caution should be taken when comparing the CIRFT results to the O'Donnell-Langer fatigue curve, especially for the composite rod maximum stress based on Eq. (F-7), because of the differences in sample types. O'Donnell-Langer was developed based on fatigue testing of zirconium alloy coupons, whereas the CIRFT testing is performed on irradiated composite rod specimens. The F35P17-3159-3312 test includes some erratic load cell data, but at this time, there is no evidence that the test was flawed.

Flexural rigidity is also measured during the dynamic test at the specific test conditions. The flexural rigidity of the specimen can change over the duration of the CIRFT test; a rod subjected to many bending cycles is expected to have a lower flexural rigidity than an uncycled rod, especially at large applied moments, and the rigidity reported herein is evaluated using data from the beginning of the test. The results of the dynamic flexural rigidity measurements are provided in Table F-5. For one of the static tests (3D8E14-0719-0872), the data required to calculate the curvature, strain, and flexural rigidity were unavailable, so this data is estimated as the average of the other static tests. The flexural rigidity measured for the sister rod specimens is plotted as a function of the estimated specimen burnup in Figure F-12, along with the measured flexural rigidity of other 17×17 rods tested at ORNL using CIRFT [F-7, F-8]; there is no observed trend with burnup. The flexural rigidity (including the measurement uncertainties from Appendix G) was also evaluated as a function of the applied bending moment (Figure F-13) and the decreasing trend is consistent with previous data. Because of the large uncertainties in the tests at low applied moment and because all the samples at high applied moment were tested statically prior to dynamic testing, only the samples tested at applied moments between 8 and 14 N-m are used in calculating the average dynamic flexural rigidity, which is 27 N-m<sup>2</sup>.

As discussed in Section F-7.1, the static specimens are tested in dynamic mode after the static test, but the dynamic results for these specimens are not strictly comparable with the dynamic-only test results. The results of the dynamic tests of these specimens are provided for information.

While most of the data are consistent with previous data from other 17 × 17 rods, two specimens failed earlier than expected: 3A1F05-3214-3367 (LT Zirc-4 clad) and F35P17-3159-3312 (Zirc-4 clad). At the tested rod elevations, both specimens have estimated oxide thicknesses ~140 μm. Other specimens were tested from nearby elevations on both rods, but only one was tested at a similar load: 3A1F05-2025-2178 failed at 48,200 cycles but only had a local oxide thickness of ~80 μm. Other Sister Rod segments tested have oxide thicknesses <70 μm (M5 and ZIRLO clad segments). For the Zirc-4 clad rod, the difference in



the performance could also be a result of the main geometric difference of the rods—the pellet length—and if so, then further data analysis focused on pellet length could clarify the effect.

### **F-7.3 Cumulative Effects Tests**

No tests have been completed to date. A fixture is under development and is discussed in Section F-8.

Table F-5. Sister rod CIRFT test results to date.

Rod type	Cladding material	Estimated specimen-average burnup (GWd/MTU)	Specimen ID	Curvature (1/m)	Cycles to failure	Applied moment (N-m) ( $\pm 0.9$ N-m)	Maximum Average Stress <sup>f</sup> (MPa) ( $\pm 10.7$ MPa)	Maximum Cladding Stress <sup>g</sup> (MPa)	Maximum Strain (%)	Dynamic flexural rigidity (N-m <sup>2</sup> )
17×17	M5	58	30AD05-0697-0850 <sup>a</sup>	$1.0 \pm 0.18$	3,368	15.8	186.0	437	$0.47 \pm 0.09$	$15.6 \pm 1.2$
17×17	M5	59	30AD05-2050-2203	$0.18 \pm 0.10$	133,000	5.1	61.9	76	$0.08 \pm 0.04$	$28.7 \pm 25.8$
17×17	M5	59	30AD05-2630-2783	$0.38 \pm 0.11$	22,300	10.7	129.6	164	$0.18 \pm 0.05$	$28.0 \pm 8.4$
17×17	M5	56	30AE14-0672-0825 <sup>a,c</sup>	$0.76 \pm 0.15$	1,630	15.6	187.0	328	$0.36 \pm 0.07$	$20.5 \pm 4.2$
17×17	M5	60	30AE14-2850-3003 <sup>c</sup>	$0.46 \pm 0.11$	9,800	10.6	127.0	193	$0.22 \pm 0.05$	$23.6 \pm 6.5$
17×17	M5	56	30AE14-3156-3309 <sup>c</sup>	$0.21 \pm 0.10$	113,000	5.0	59.5	92	$0.10 \pm 0.05$	$23.2 \pm 18.9$
17×17	Zirc-4	66	F35P17-2027-2180 <sup>c</sup>	$0.15 \pm 0.10$	1,340,000	4.0	47.8	66	$0.07 \pm 0.04$	$26.8 \pm 34.8$
17×17	Zirc-4	62	F35P17-3159-3312 <sup>c,d</sup>	$0.32 \pm 0.10$	773	8.6	101.0	122	$0.15 \pm 0.05$	$30.7 \pm 12.5$
17×17	LT Zirc-4	48	3A1F05-3214-3367	$0.41 \pm 0.11$	3,450	8.8	105.9	178	$0.19 \pm 0.05$	$21.6 \pm 6.7$
17×17	LT Zirc-4	56	3A1F05-1853-2006 <sup>a</sup>	$0.82 \pm 0.16$	1,300	15.9	191.5	357	$0.39 \pm 0.07$	$19.3 \pm 3.9$
17×17	LT Zirc-4	56	3A1F05-2025-2178	$0.38 \pm 0.11$	48,200	8.8	105.9	165	$0.18 \pm 0.05$	$23.2 \pm 7.5$
17×17	LT Zirc-4	44	3A1F05-3367-3520	$0.14 \pm 0.09$	214,000	4.0	48.6	59	$0.06 \pm 0.04$	$29.7 \pm 42.2$
17×17	ZIRLO	64	3D8E14-0719-0872 <sup>a</sup>	$0.58^2 \pm 0.12$	9,589	15.3	181.0	362	$0.39^b$	$18.4^b$
17×17	ZIRLO	64	3D8E14-2412-2565 <sup>c</sup>	$0.18 \pm 0.10$	191,000	5.0	60.1	70	$0.08 \pm 0.04$	$31.3 \pm 31.0$
17×17	ZIRLO	62	3D8E14-2963-3116	$0.31 \pm 0.10$	39,700	8.7	104.2	136	$0.15 \pm 0.05$	$28.1 \pm 10.5$
17×17	ZIRLO	63	3D8E14-1178-1331	$0.16 \pm 0.10$	212,000	4.9	58.4	69	$0.08 \pm 0.04$	$30.9 \pm 32.4$
17×17	ZIRLO	59	3F9N05-0719-0872 <sup>a,c</sup>	$0.86 \pm 0.16$	3,540	15.5	186.3	374	$0.41 \pm 0.08$	$18.0 \pm 3.6$
17×17	ZIRLO	59	3F9N05-2329-2482 <sup>c</sup>	$0.21 \pm 0.10$	189,000	4.8	57.3	92	$0.10 \pm 0.05$	$22.6 \pm 19.3$
17×17	ZIRLO	57	3F9N05-2710-2863 <sup>c</sup>	$0.40 \pm 0.11$	33,000	8.7	104.7	173	$0.19 \pm 0.05$	$21.8 \pm 6.9$
17×17	ZIRLO	59	6U3K09-2310-2463	$0.42 \pm 0.11$	1.75E+04	12.7	152.3	182	$0.20 \pm 0.05$	$30.2 \pm 8.5$
17×17	ZIRLO	59	6U3K09-2463-2616	$0.27 \pm 0.10$	3.92E+04	8.9	106.5	119	$0.13 \pm 0.05$	$32.4 \pm 13.3$
17×17	ZIRLO	58	6U3K09-2635-2788	$0.17 \pm 0.10$	1.10E+05	6.4	76.8	75	$0.08 \pm 0.04$	$37.1 \pm 21.7$
17×17	ZIRLO	50	6U3K09-3200-3353	$0.31 \pm 0.10$	3.49E+04	8.8	105.3	127	$0.15 \pm 0.05$	$30.0 \pm 11.8$
17×17	ZIRLO	46	6U3K09-3353-3506	$0.43 \pm 0.11$	1.41E+04	11.7	140.2	187	$0.21 \pm 0.05$	$27.0 \pm 7.4$

<sup>a</sup> Dynamically tested following a static test.

<sup>b</sup> Estimated based on average flexural rigidity of valid static/dynamic tests.

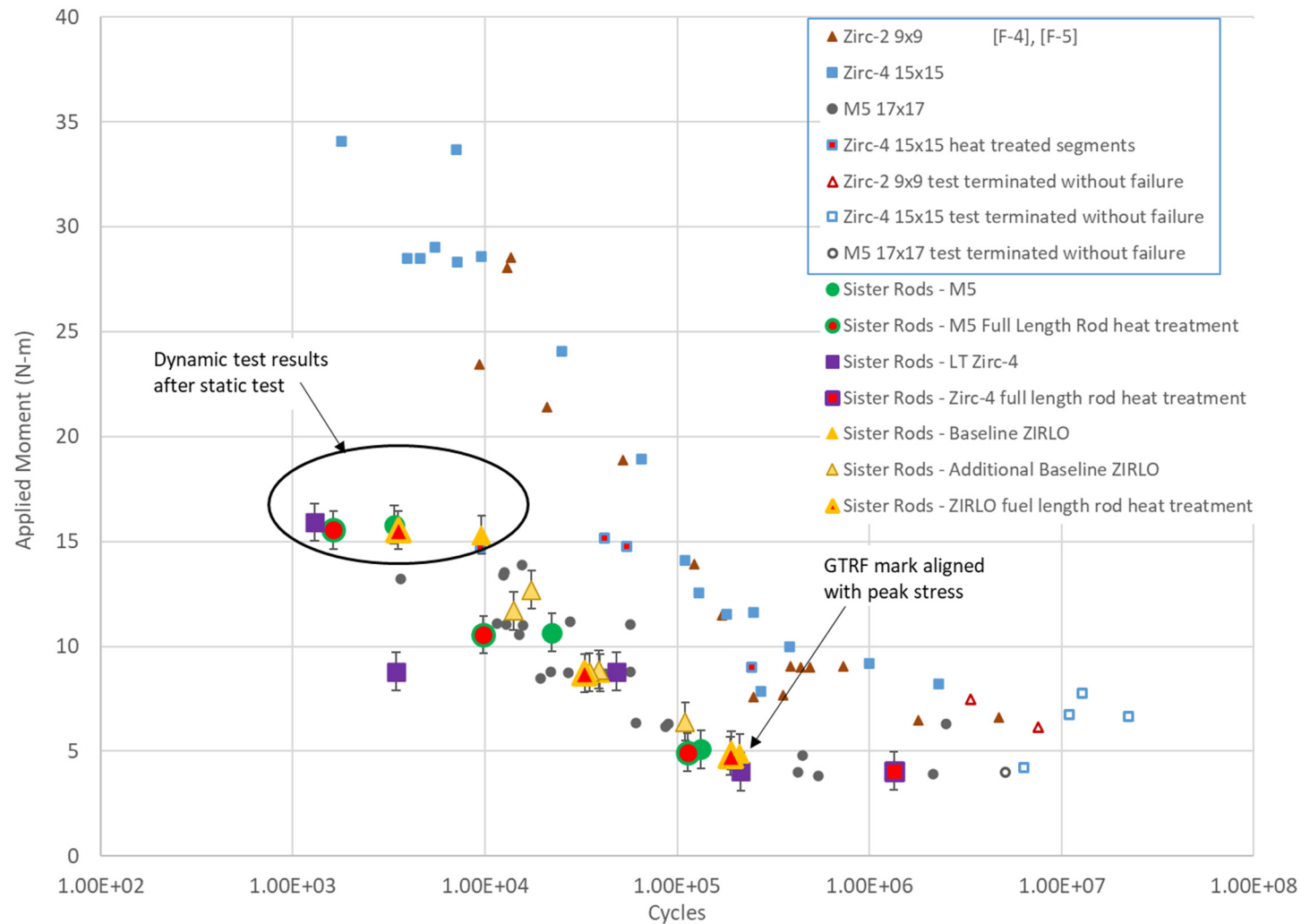
<sup>c</sup> Specimen from heat-treated rod.

<sup>d</sup> Erratic load cell data were recorded during the test. The applied moment might have been higher.

<sup>e</sup> Specimen had a GTRF mark in the gauge section that was aligned (as was possible) with the expected maximum strain location.

<sup>f</sup> Stress calculated using the equivalent stress approach per Eq. (F-7). Measured ODs used in calculation – typically around 9.5 mm.

<sup>g</sup> Stress calculated using the modified equivalent stress approach in Reference [F-4] to represent the cladding surface stress.



**Figure F-8. Results of CIRFT tests plotted with reference data, applied moment vs. cycles to failure. The error bars on the sister rod data represent the calculated uncertainty (0.8 N-m) in Section G-3.3, Appendix G (non-sister rod data from [F-4], [F-5]).**

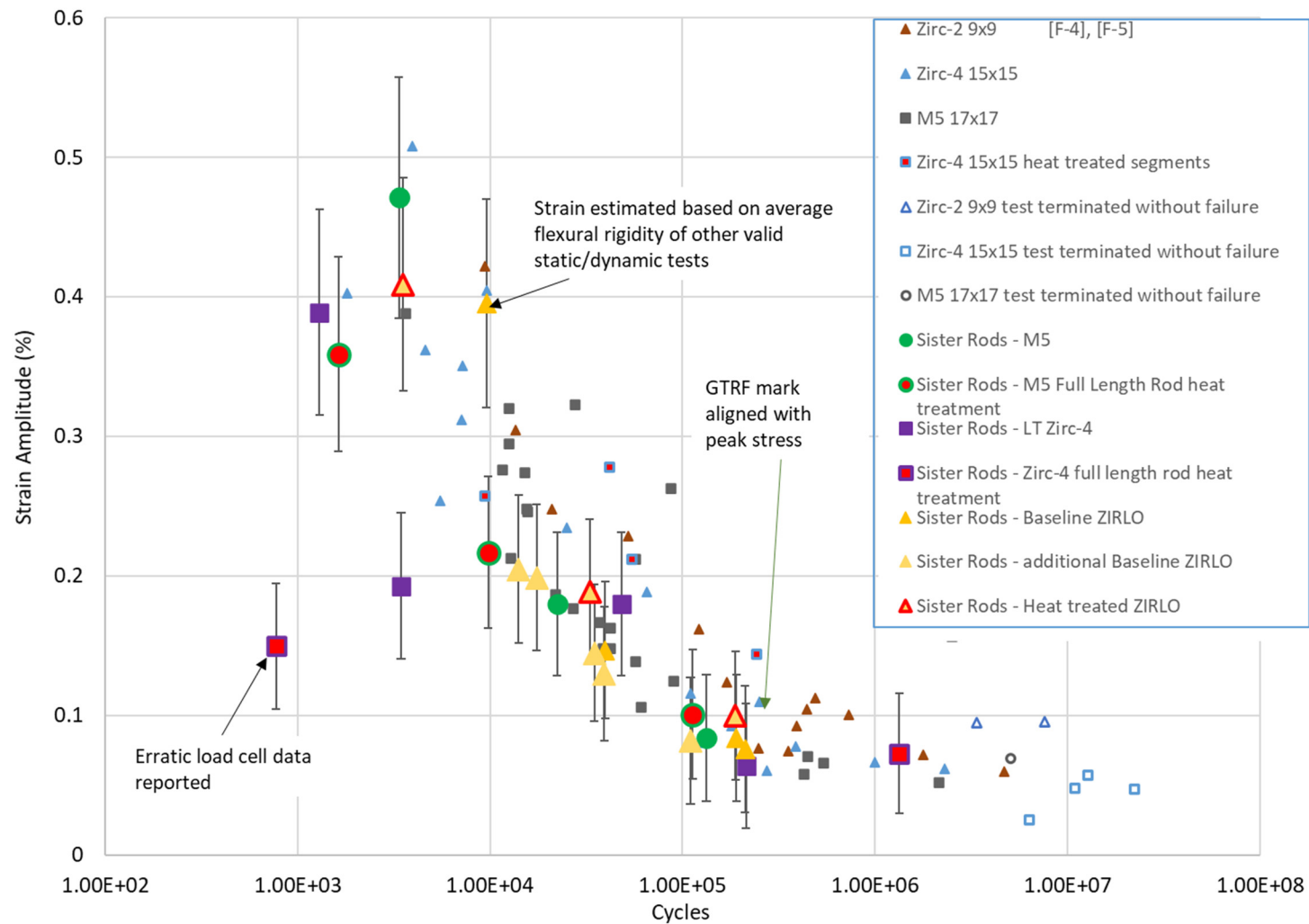
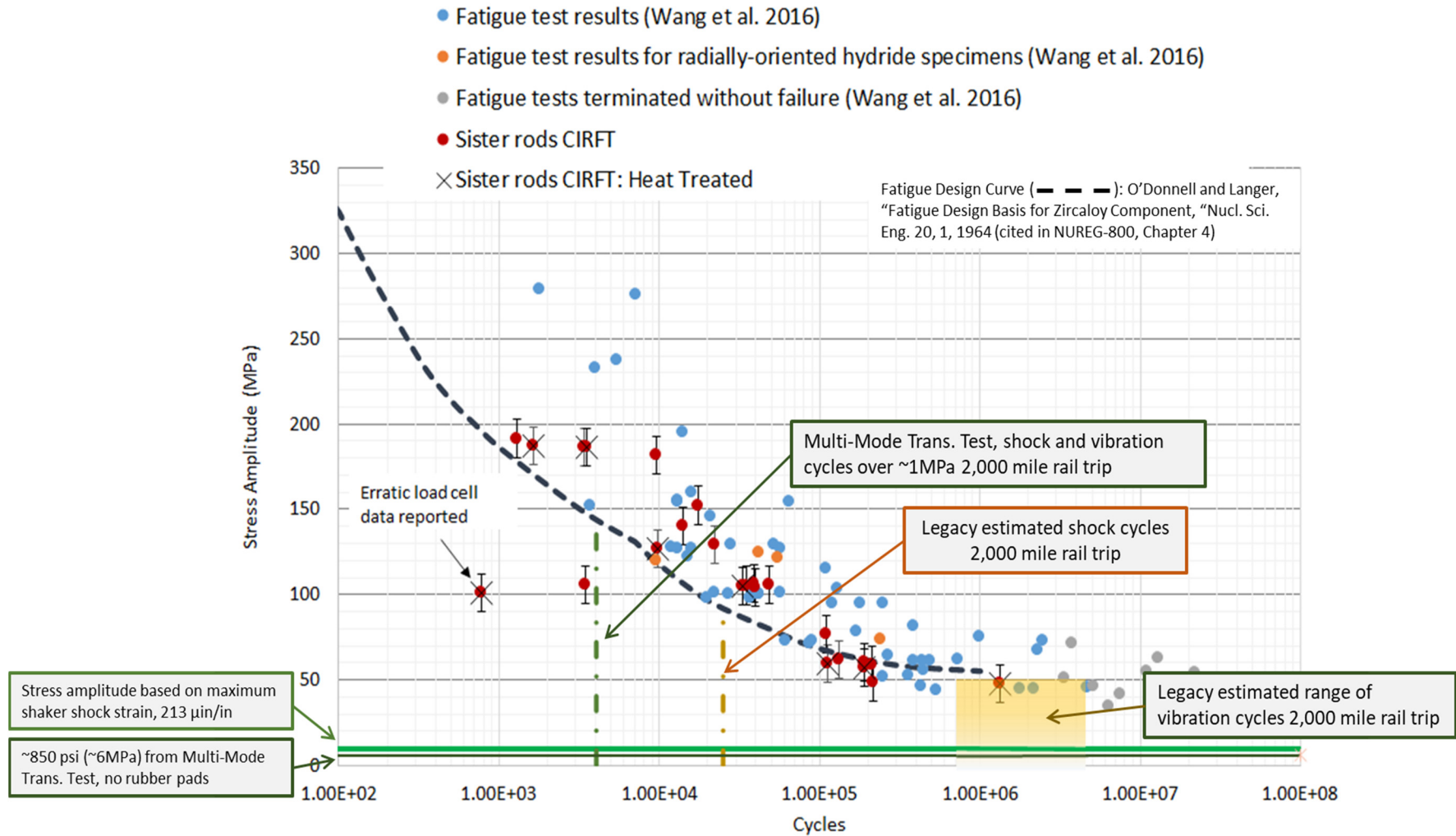


Figure F-9. Results of CIRFT tests completed to date, strain amplitude vs. cycles to failure. The error bars on the sister rod data represent the calculated uncertainty in Section G-3.4, Appendix G (non-sister rod data from [F-4], [F-5]).



**Figure F-10. Average stress amplitude of the composite rod based on Eq. (F-7), as a function of cycles to failure for the sister rods. The error bars on the sister rod data represent the calculated uncertainty in Section G-3.5, Appendix G.**

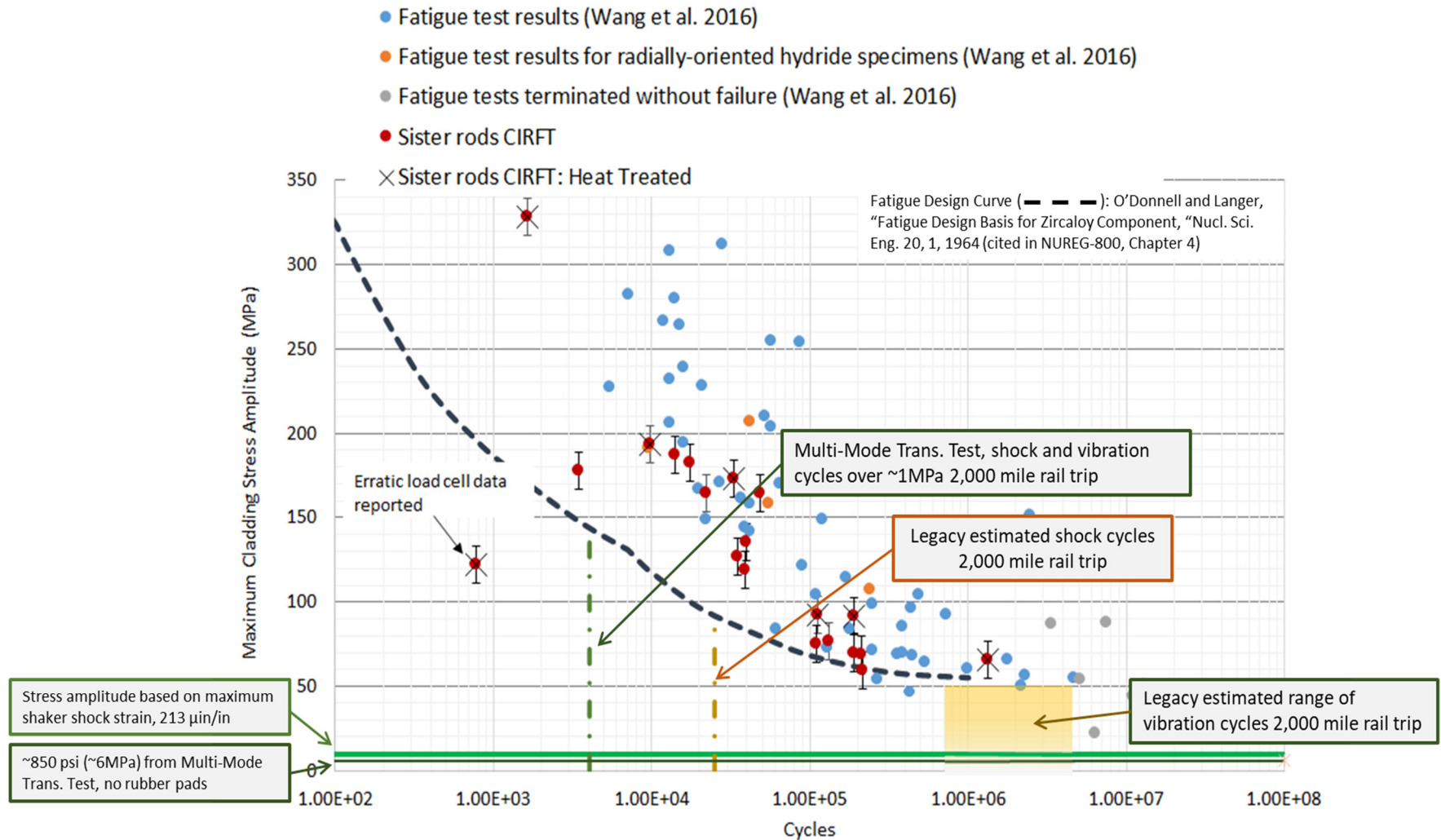


Figure F-11. Cladding stress amplitude as a function of cycles to failure for the sister rods. The error bars on the sister rod data represent the calculated uncertainty in Section G-3.5, Appendix G.

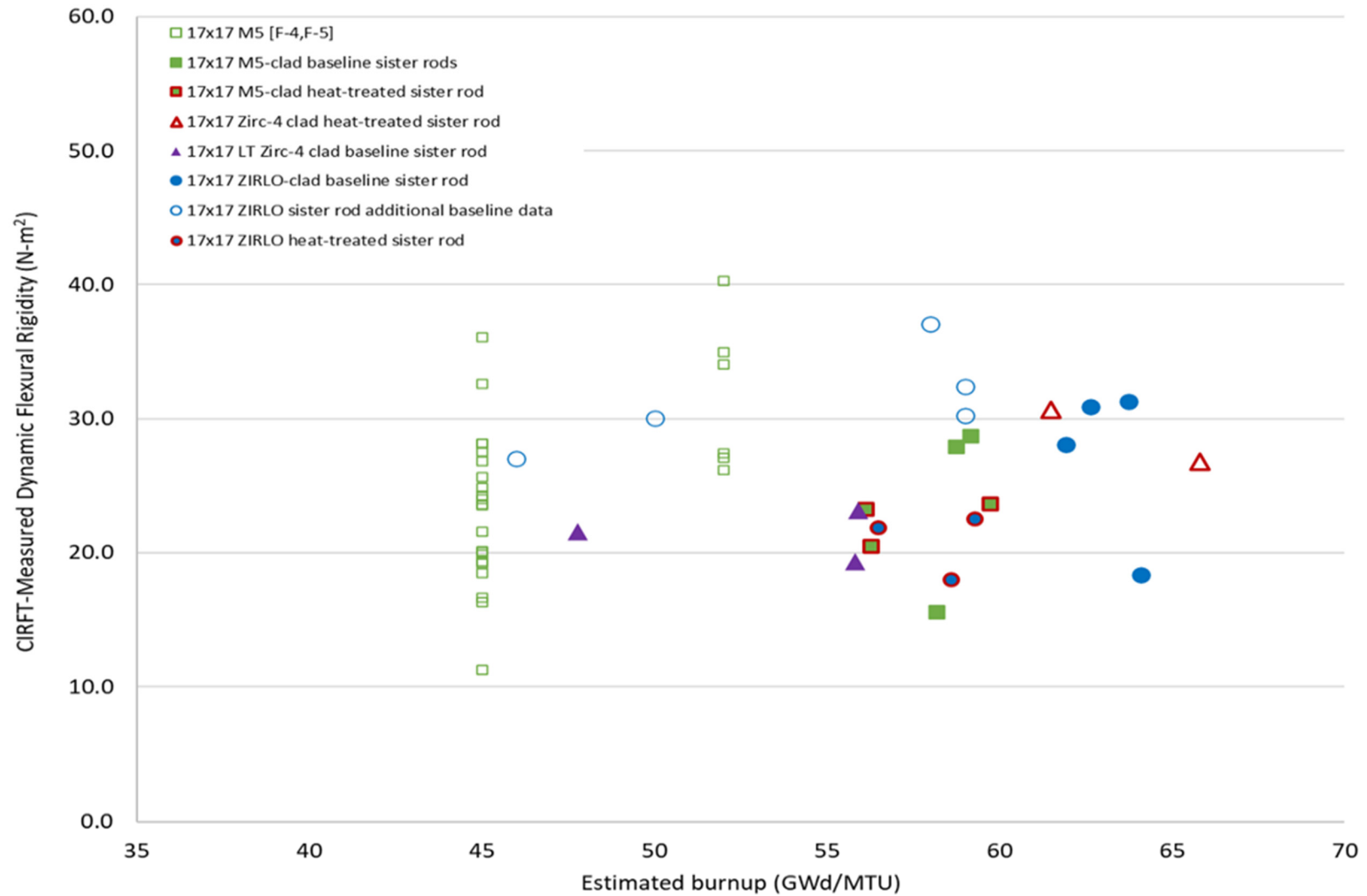


Figure F-12. CIRFT-measured flexural rigidity of the sister rod segments tested as a function of estimated segment burnup plotted with previous CIRFT data.

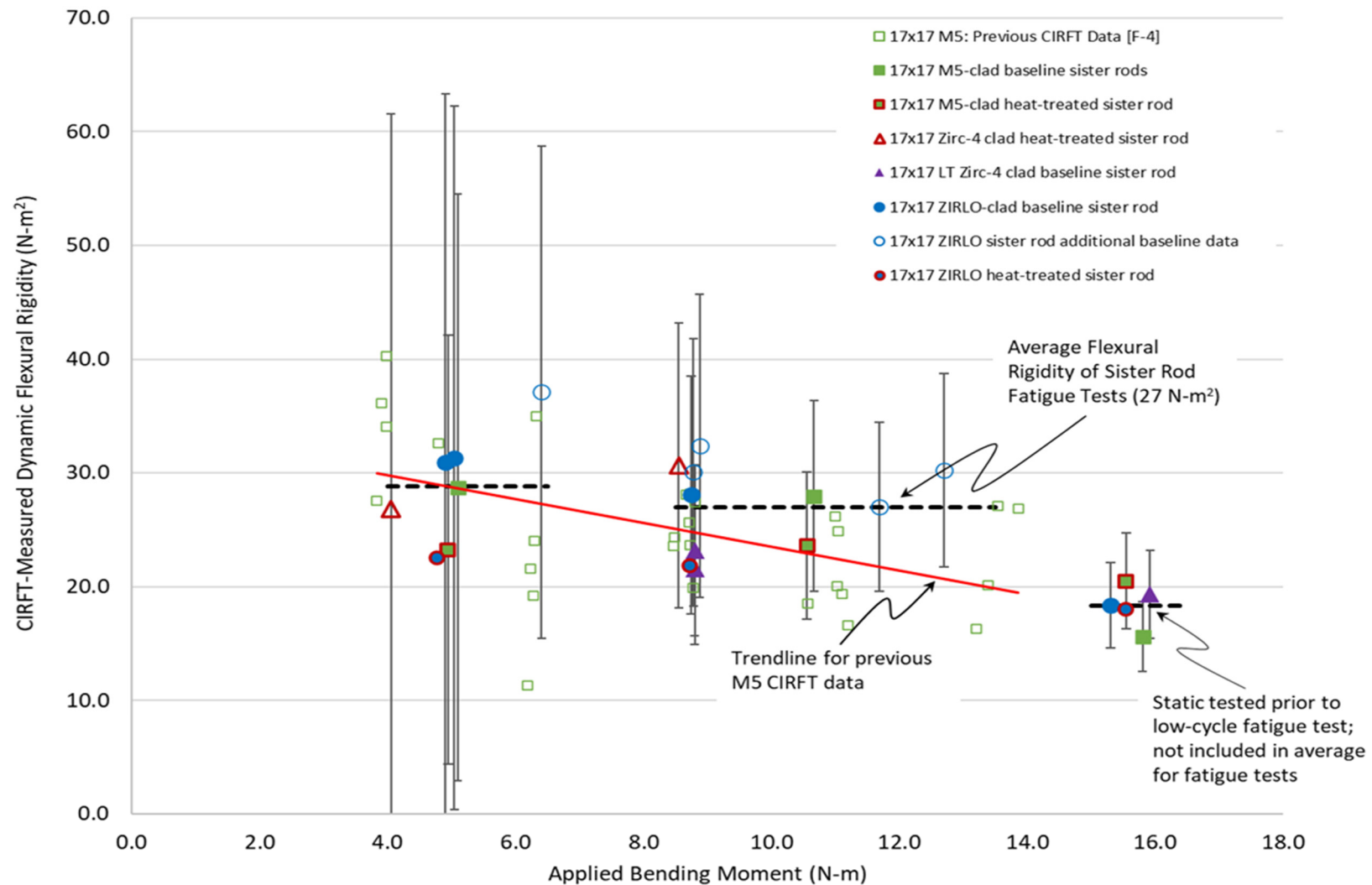


Figure F-13. Trend of CIRFT-measured dynamic flexural rigidity with applied bending moment. The error bars on the sister rod data represent the calculated uncertainty in Section G-3.6, Appendix G.



## F-7.4 Comparisons of Paired Specimens

The paired results are tabulated in Table F-6. Averages are provided for burnup, cycles to failure, strain, and flexural rigidity for comparison purposes. For the M5-clad and ZIRLO-clad segments, the heat-treated rods generally have a shorter fatigue lifetime and lower flexural rigidity. Revisiting Figure F-12, the small but consistent difference in flexural rigidity between the baseline and heat-treated rods is clear. The reverse seems to be true for the Zirc-4-clad and LT Zirc-4-clad pairs; the heat-treated Zirc-4-clad segments have a higher flexural rigidity and a longer fatigue lifetime than the baseline LT Zirc-4-clad segments. However, there are several differences in the parent rods, and these two rods are not good matches for comparing heat-treatment effects. One potential explanation for the difference in performance is the pellet length. As shown in Table 4 of the NDE report [F-6], the pellets in the Zirc-4-clad rod are ~13.6 mm long, whereas the pellets in all other sister rods are ~10 mm long. It is possible that the increased stiffness is related to the longer pellet length.

Figure F-8 further illustrates a reduced fatigue lifetime related to the heat treatments. This effect is seen for all M5-clad and ZIRLO-clad heat-treated specimens. However, when the cycles to failure are plotted with the calculated strain amplitude, the offset related to the heat-treatment is eliminated, as shown in Figure F-9. Since the rods have nearly the same geometry, the calculated strain would normally be expected to provide the same offset between baseline and heat-treated specimen results. However, for CIRFT, the strain is calculated based on the measured rod deflection and flexural rigidity. Because the heat-treated rods have a lower flexural rigidity, the stress and strain corresponding to the same bending moment are higher. Thus, plotting the fatigue lifetime by strain amplitude resolves the offset and the heat-treated specimen's fatigue lifetime is consistent with the baseline specimen's performance given the same amount of applied stress and strain.

On the basis of the CIRFT rigidity measurements alone, as shown in Figure F-13, the observed difference between the heat-treated and baseline could be considered within measurement uncertainty. However, given the good alignment of the strain-amplitude results and the results of mechanical tests (Appendix E), the heat treatments clearly resulted in a lower flexural rigidity that led to a shorter fatigue lifetime for the same applied load. There are at least three potential sources for a reduction in flexural rigidity with FHT: (1) a permanent increase in cladding OD and a pellet-cladding gap that resulted from the increased pressure at temperature during the heat-treatment, (2) the annealing of irradiation defects resulting from the FHT, and (3) the reorientation of precipitated hydrides in the cladding during the heat-treatment that make it more susceptible to cladding fracture. The latter source is unlikely since the amount of hydride reorientation resulting from the sister rod heat treatments (Appendices A and B) varied by cladding alloy; only very short, reoriented hydrides were observed on the Zirc-4/LT Zirc-4-clad rods, isolated hydrides were observed at the ID/OD on the ZIRLO-clad rods, and many reoriented hydrides were observed on the M5-clad rods. Since reorientation was not observed for all heat-treated rods, the difference in flexural rigidity and fatigue lifetime is not likely to be related to hydride reorientation. However, irradiation defect annealing could have occurred during FHT (particularly on the M5-clad rod as discussed in Appendix A), resulting in a lower overall rigidity of the FHT rod, leading to a shorter fatigue lifetime. The other two potential sources are being investigated.

One specimen with visible GTRF marks was tested with the marks aligned (as was possible) with the highest cladding strain location, and the GTRF marks did not reduce the fatigue lifetime. The GTRF marks on this specimen are not considered representative or bounding; the specimen was selected based on availability only and further tests should be completed to fully explore the effect.

Table F-6. Results arranged by paired specimens (baseline rods vs. heat-treated rods) for static/dynamic and dynamic CIRFT.

Baseline rods								Heat-treated rods						
Specimen ID		Cladding type	Estimated specimen average burnup (GWd/MTU)	Cycles to failure	Dynamic flexural rigidity (N-m <sup>2</sup> )	Applied strain amplitude (%)		Specimen ID		Cladding type	Estimated specimen average burnup (GWd/MTU)	Cycles to failure	Dynamic flexural rigidity (N-m <sup>2</sup> )	Applied strain amplitude (%)
30AD05 0697 0850 <sup>a</sup>		M5	58	3,368	15.6	0.47		30AE14 0672 0825 <sup>a</sup>		M5	56	1,630	20.5	0.36
30AD05 2050 2203			59	133,000	28.7	0.08		30AE14 3156 3309			56	113,000	23.2	0.10
30AD05 2630 2783			59	22,300	28.0	0.18		30AE14 2850 3003			60	9,800	23.6	0.22
Average			59	52,889	24.1	0.24					57	41,477	22.4	0.23
3A1F05 1853 2006 <sup>a</sup>		LT Zirc-4	56	1,300	19.3	0.39		F35P17 1855 2008 <sup>a,c,e</sup>		Zirc-4	53	525	28.7 <sup>b</sup>	0.16 <sup>b</sup>
3A1F05 3367 3520			44	214,000	29.7	0.06		F35P17 2027 2180			52	1,340,000	26.8	0.07
3A1F05 2025 2178			56	48,200	23.2	0.18								
3A1F05 3214 3367			48	3,450	21.6	0.19		F35P17 3159 3312 <sup>c</sup>			47	773	30.7	0.15
Average			51	66,738	24.8	0.14					51	447,099	28.8	0.11
3D8E14 0719 0872 <sup>a</sup>		ZIRLO	64	9,589	18.4 <sup>b</sup>	0.39 <sup>b</sup>								
3D8E14 2412 2565 <sup>d</sup>			64	191,000	31.3	0.08								
3D8E14 2963 3116			62	39,700	28.1	0.15								
3D8E14 1178 1331			63	212,000	30.9	0.08								
6U3K09 2310 2463			59	17,500	30.2	0.20		3F9N05 0719 0872 <sup>a</sup>		ZIRLO	59	3,540	18.0	0.41
6U3K09 2463 2616			59	39,200	32.4	0.13		3F9N05 2329 2482			59	189,000	22.6	0.10
6U3K09 2635 2788			58	110,000	37.1	0.08		3F9N05 2710 2863			57	33,000	21.8	0.19
6U3K09 3200 3353			50	34,900	30.0	0.15								
6U3K09 3353 3506			46	14,100	27.0	0.21								
Average			60	50,400	31.4	0.15					58	75,180	21.8	0.19

<sup>a</sup> Dynamically tested following a static test.

<sup>b</sup> Estimated.

<sup>c</sup> Erratic load cell data were recorded during the test. The applied moment and strain amplitude was likely higher.

<sup>d</sup> Specimen had a GTRF mark in the gauge section that was aligned (as possible) with the expected maximum strain location.

<sup>e</sup> Deeper examination indicates that this specimen broke during the static test and therefore the dynamic test results are invalid.

## F-7.5 Imaging of the Fractured Specimens

To provide additional information regarding how the specimens fractured, magnified images were obtained using the Irradiated Microsphere Gamma Analyzer facility at the Irradiated Fuels Examination Laboratory. The images provide information about the location where the fatigue crack propagated to fracture and about whether the fracture occurred at a pellet-pellet interface.

In many cases, the locations of the highest strains appear on the specimen surface as dull oval areas, as shown on Figure F-15. Rods with higher oxide thicknesses had some additional spalling during the test, which is particularly visible in LT Zirc-4 clad rods such as 3A1F05-1853-2006 (Figure F-28).

The M5-clad specimens tended to break cleanly around the circumference of the rod, but the break occurred in the body of the pellet, rather than at the pellet-pellet interface. Three of the six specimens broke in the center third of the specimen, whereas the other three broke near or inside a dogbone grip.

The ZIRLO-clad specimens broke differently, depending upon the parent rod. The baseline 3D8E14 specimens tended to break cleanly around the circumference of the rod but at approximately a 30-degree angle. Three of the four specimens broke at pellet-pellet interfaces, and the cladding fracture extended into the body of a pellet. Three of the four specimens broke in the center third, and one broke near the dogbone. All 6U3K09 specimens broke circumferentially: three of the five broke near or inside the dogbone grip, and three of the five broke at pellet-pellet interfaces. Two of the 6U3K09 specimens had double fractures—a partial circumference break in the center third, with the full fracture near the dogbone. All specimens from FHT rod 3F9N05 broke in the center third of the specimen: two had a flat circumferential break at the pellet-pellet interface, and one broke in the body of a pellet at approximately a 30-degree angle.

The Zirc-4-clad specimens all broke dramatically in the same way, with a flat circumferential crack around half the rod that was sheared around the half of the rod and at a pellet-pellet interface. One specimen fractured in the center third of the dogbone, and two fractured near the dogbone grip. The Zirc-4 clad fractures are jagged, and the sheared sections span a full pellet length or more, although the crack appears to have nucleated at a pellet-pellet interface. The baseline LT Zirc-4-clad specimens look similar to the LT Zirc-4 specimens at higher rod elevations, and at lower elevations they also look similar to the ZIRLO rods. Two baseline LT Zirc-4-clad specimens fractured in the center third of the specimen, and three fractured at pellet-pellet interfaces.

There does not appear to be a difference in the fracture mode of the baseline and heat-treated rods. The specimens with lower than expected fatigue lifetimes did not fracture in an anomalous manner.

Table F-7 summarizes the visual observations of CIRFT-fractured dogbones.

**Table F-7. Summary of visual observations of CIRFT-fractured dogbones.**

Rod type	Cladding material	Estimated specimen-average burnup (GWd/MTU)	Specimen ID	Fracture location	Cladding fracture orientation	Pellet fracture appearance
17×17	M5	58	30AD05-0697-0850	Center third	Circumferential	Pellet body
17×17	M5	59	30AD05-2050-2203	In grip	Circumferential	Pellet body
17×17	M5	59	30AD05-2630-2783	Near grip	Circumferential with some flaring and uneven ends	Pellet body but very near end
17×17	M5	56	30AE14-0672-0825	Center third	Circumferential with some flaring and uneven ends	Pellet body
17×17	M5	60	30AE14-2850-3003	Near grip	Circumferential	Pellet body
17×17	M5	56	30AE14-3156-3309	Center third	Circumferential with partial shearing	Pellet body
17×17	Zirc-4	66	F35P17-1855-2008	Center third	Partially sheared	At pellet end and through body
17×17	Zirc-4	66	F35P17-2027-2180	Near grip	Partially sheared	At pellet end
17×17	Zirc-4	62	F35P17-3159-3312	Near grip	Partially sheared	At pellet end
17×17	LT Zirc-4	48	3A1F05-3214-3367	In grip	Partially sheared	Pellet end
17×17	LT Zirc-4	56	3A1F05-1853-2006	Near grip	Circumferential at ~30-degree angle	Just off pellet end
17×17	LT Zirc-4	56	3A1F05-2025-2178	Center third	circumferential	Pellet end
17×17	LT Zirc-4	44	3A1F05-3367-3520	Center third	Partially sheared	Pellet body
17×17	ZIRLO	64	3D8E14-0719-0872	Near grip	Circumferential with partial shearing	Pellet end
17×17	ZIRLO	64	3D8E14-2412-2565	Center third	Circumferential at ~30-degree angle	Pellet body
17×17	ZIRLO	62	3D8E14-2963-3116	Center third	circumferential	Pellet end
17×17	ZIRLO	63	3D8E14-1178-1331	Center third	Circumferential. GTRF mark obliterated.	Pellet end
17×17	ZIRLO	59	3F9N05-0719-0872 <sup>3</sup>	Center third	Circumferential at ~30-degree angle	Pellet body
17×17	ZIRLO	59	3F9N05-2329-2482	Center third	Circumferential	Pellet end
17x17	ZIRLO	57	3F9N05-2710-2863	Center third	Circumferential	Pellet end
17×17	ZIRLO	59	6U3K09-2310-2463	Center and near grip; double fracture	Circumferential	Pellet end
17×17	ZIRLO	59	6U3K09-2463-2616	Near grip	Circumferential	Pellet end
17×17	ZIRLO	58	6U3K09-2635-2788	At grip	Circumferential	Pellet end
17×17	ZIRLO	50	6U3K09-3200-3353	Center third and near grip, double fracture	Circumferential	Pellet body
17×17	ZIRLO	46	6U3K09-3353-3506	Near grip	Circumferential	Pellet body

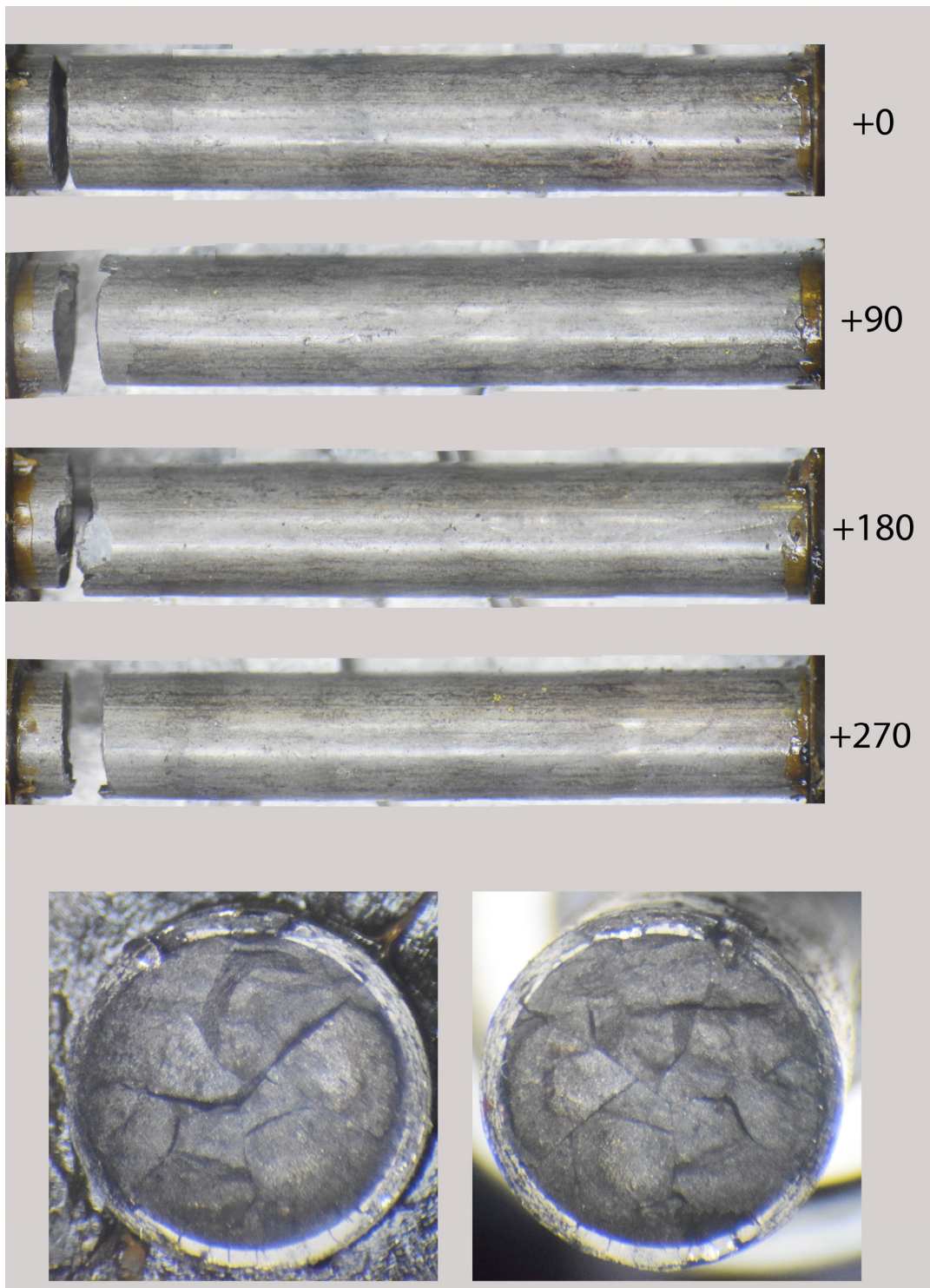


Figure F-14. 6U3K09-3353-3506 post-fatigue test condition.



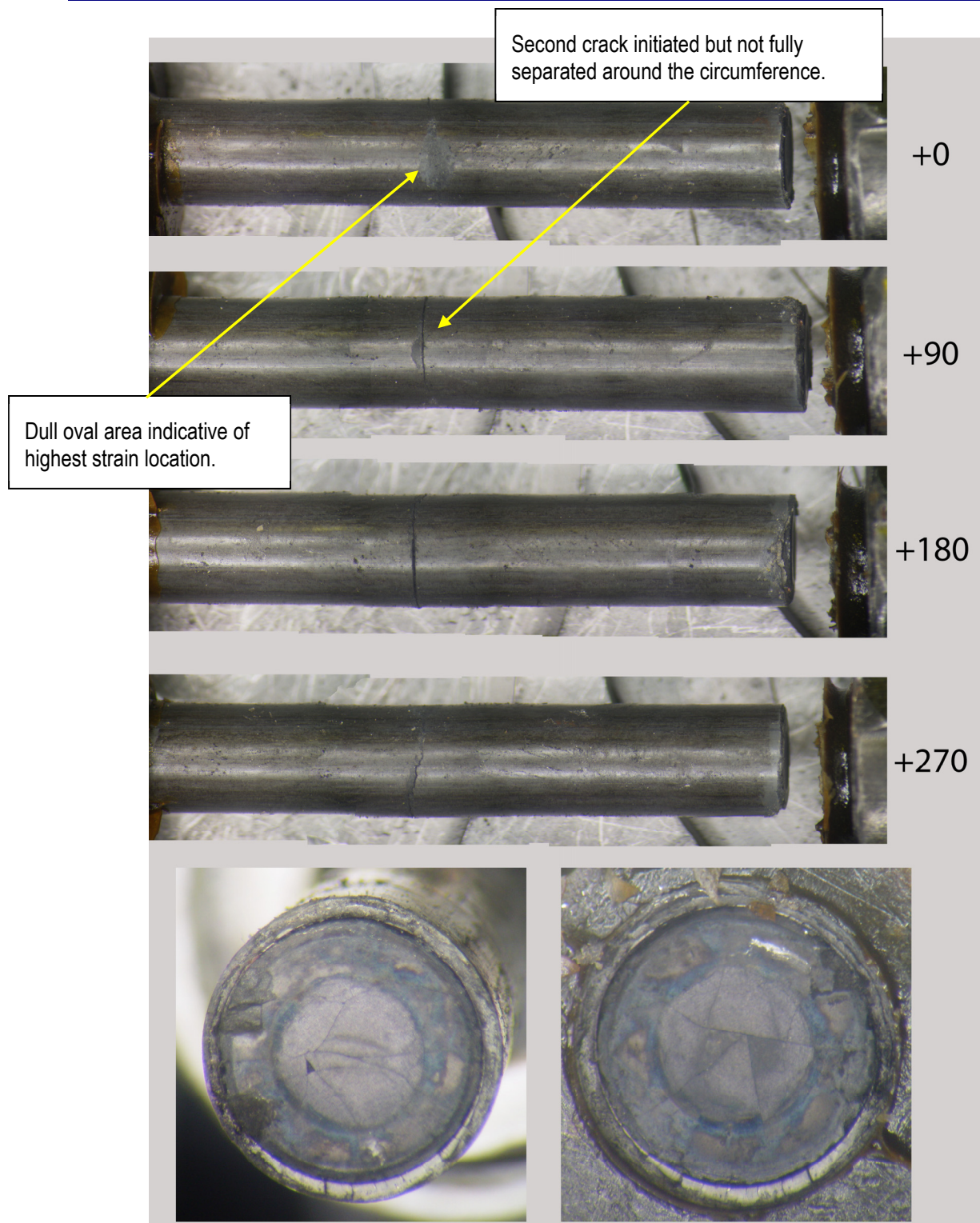
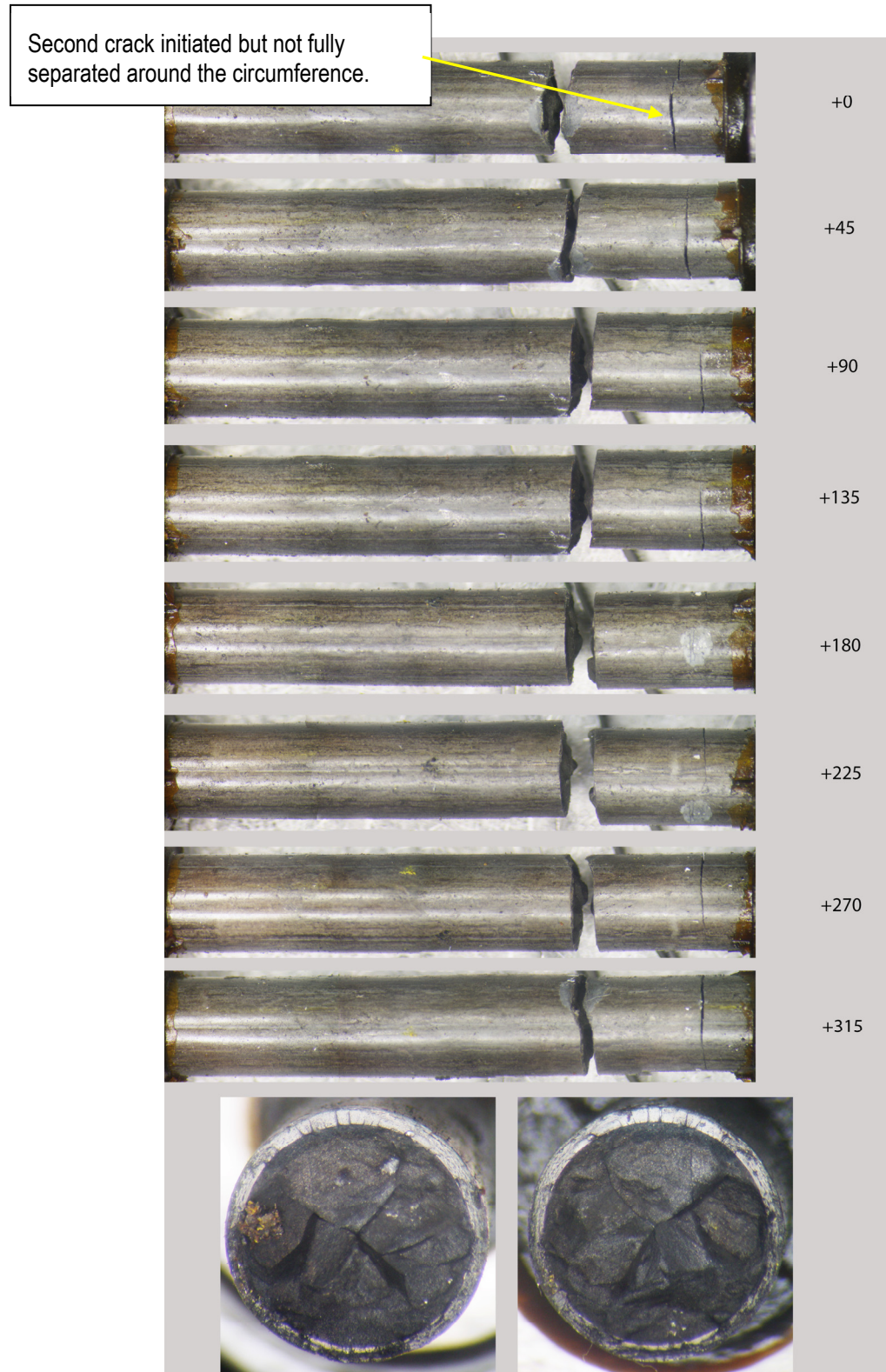
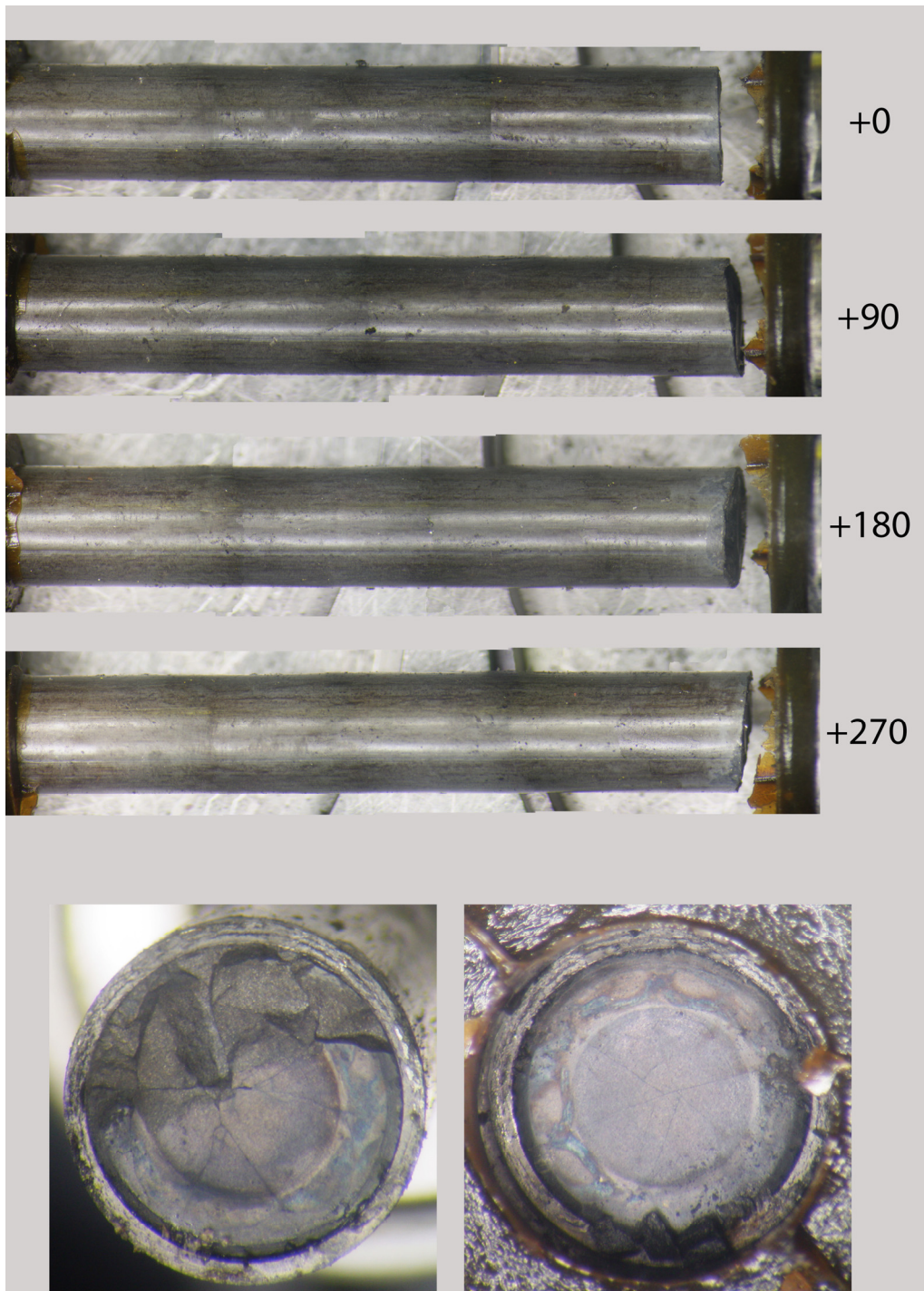


Figure F-15. 6U3K09-2310-2463 post-fatigue test condition.



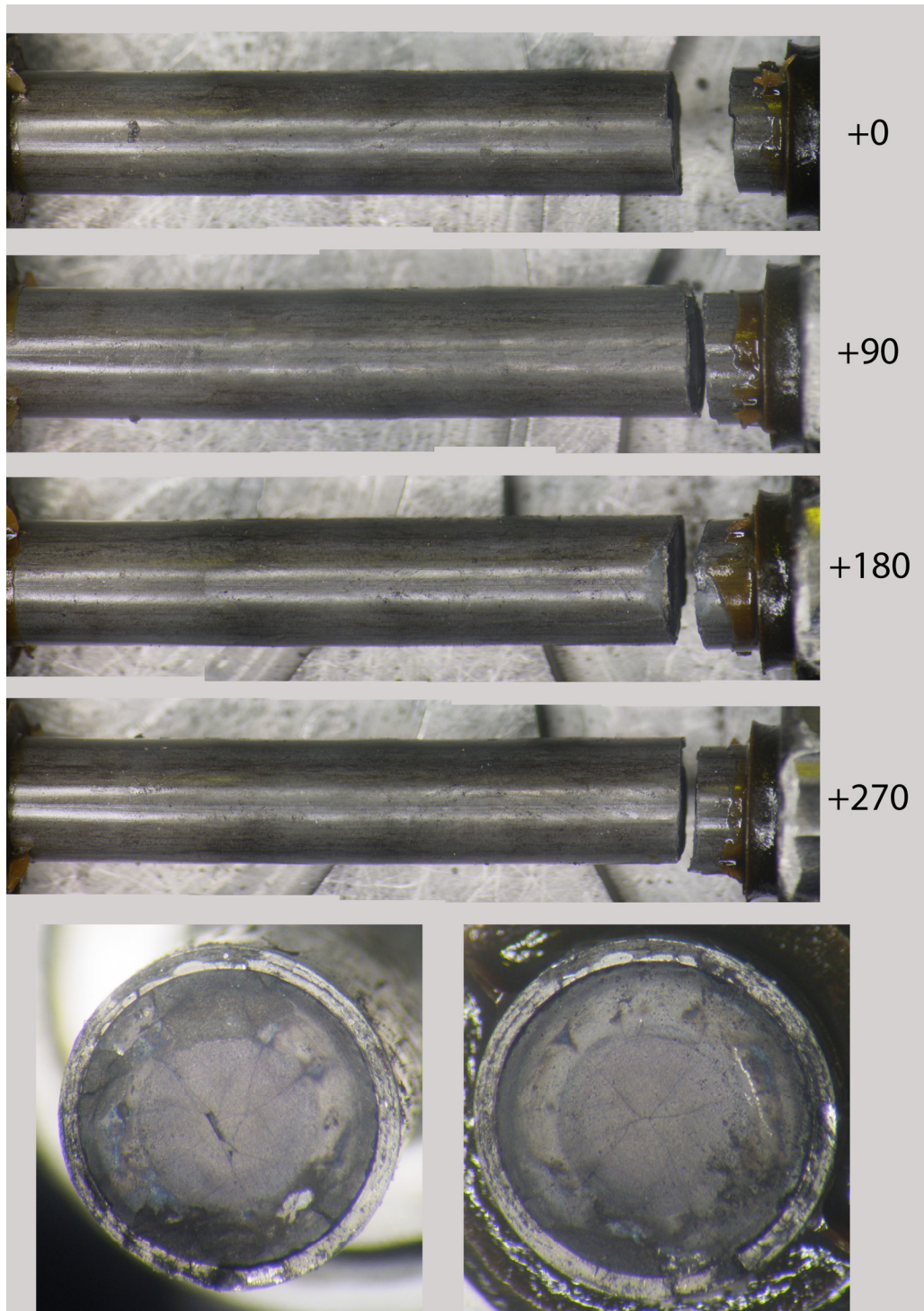
**Figure F-16. 6U3K09-3200-3353 post-fatigue test condition.**





**Figure F-17. 6U3K09-2635-2788 post-fatigue test condition.**





**Figure F-18. 6U3K09-2463-2616 post-fatigue test condition.**

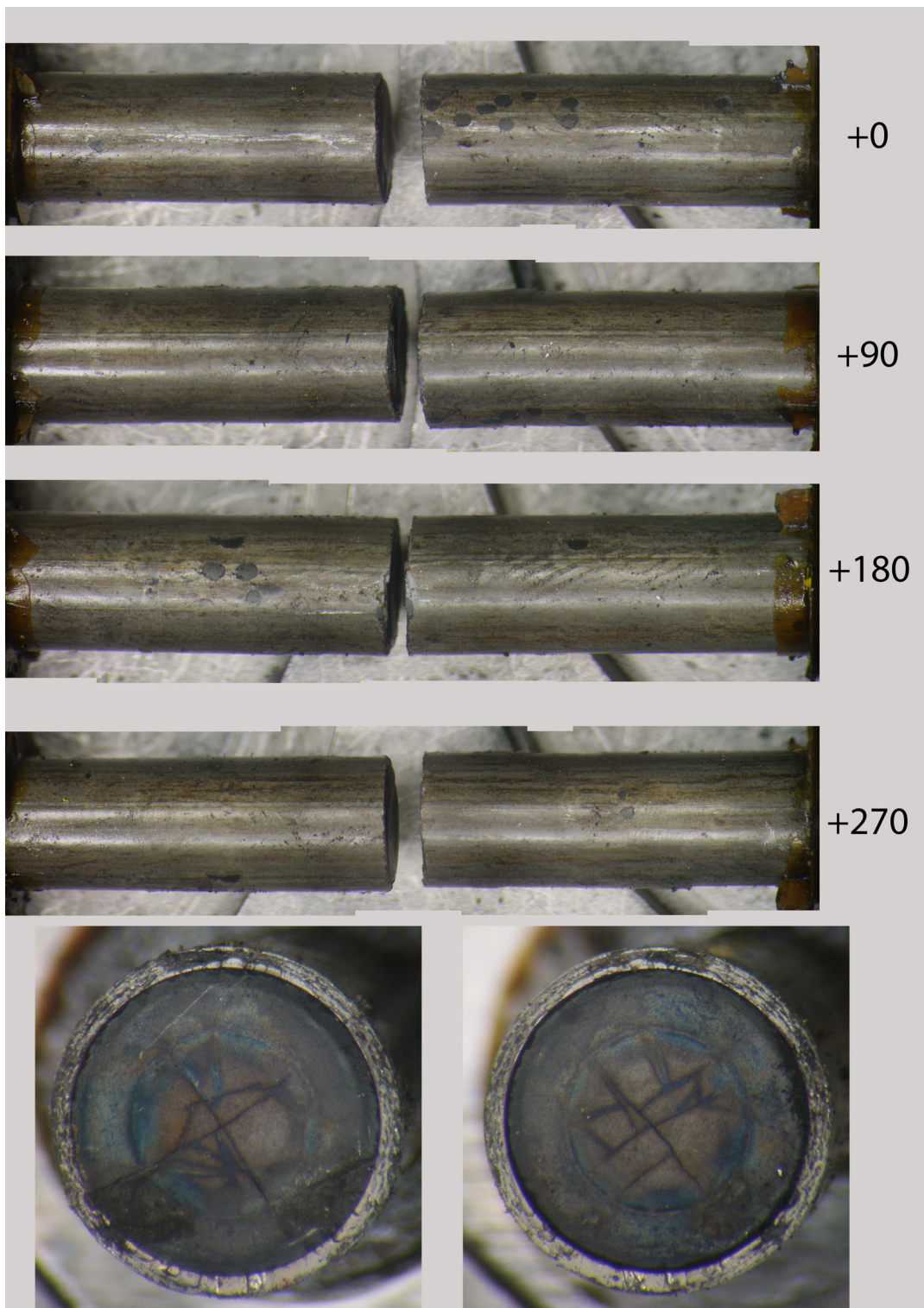


Figure F-19. 3F9N05-2710-2863 post-fatigue test condition.



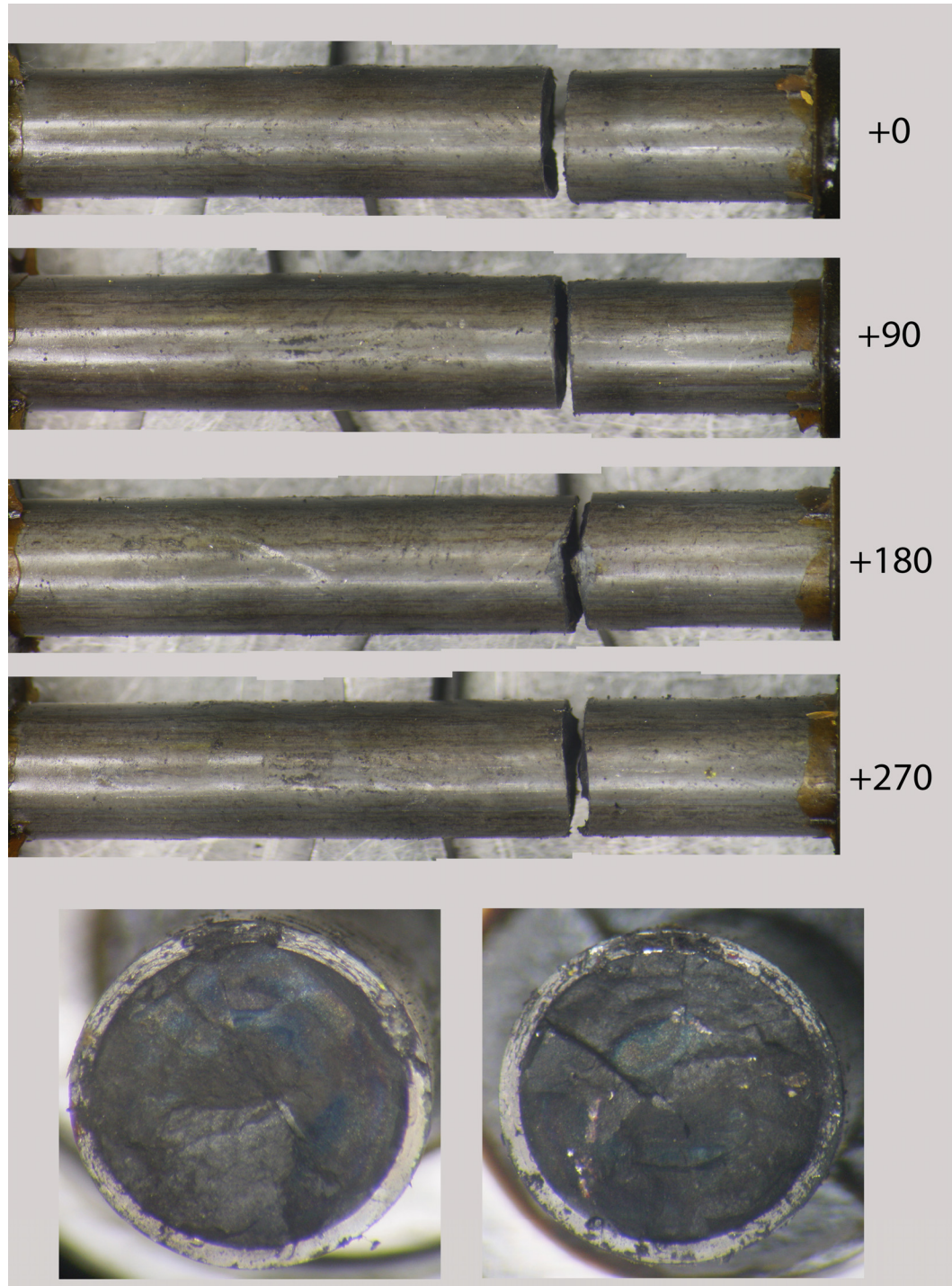


Figure F-20. 3F9N05-2329-2482 post-fatigue test condition.

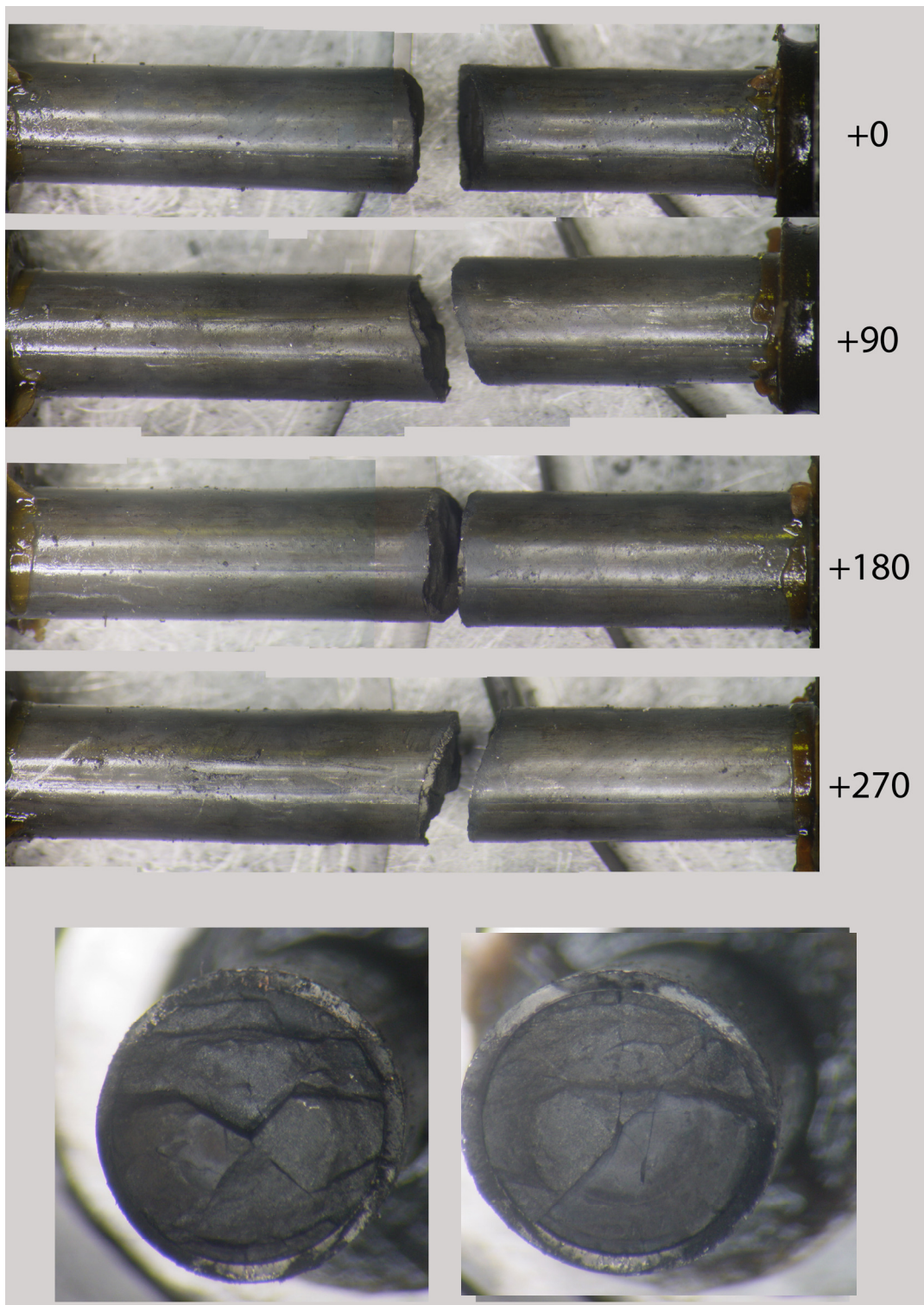


Figure F-21. 3F9N05-0719-0872 post-fatigue test condition.



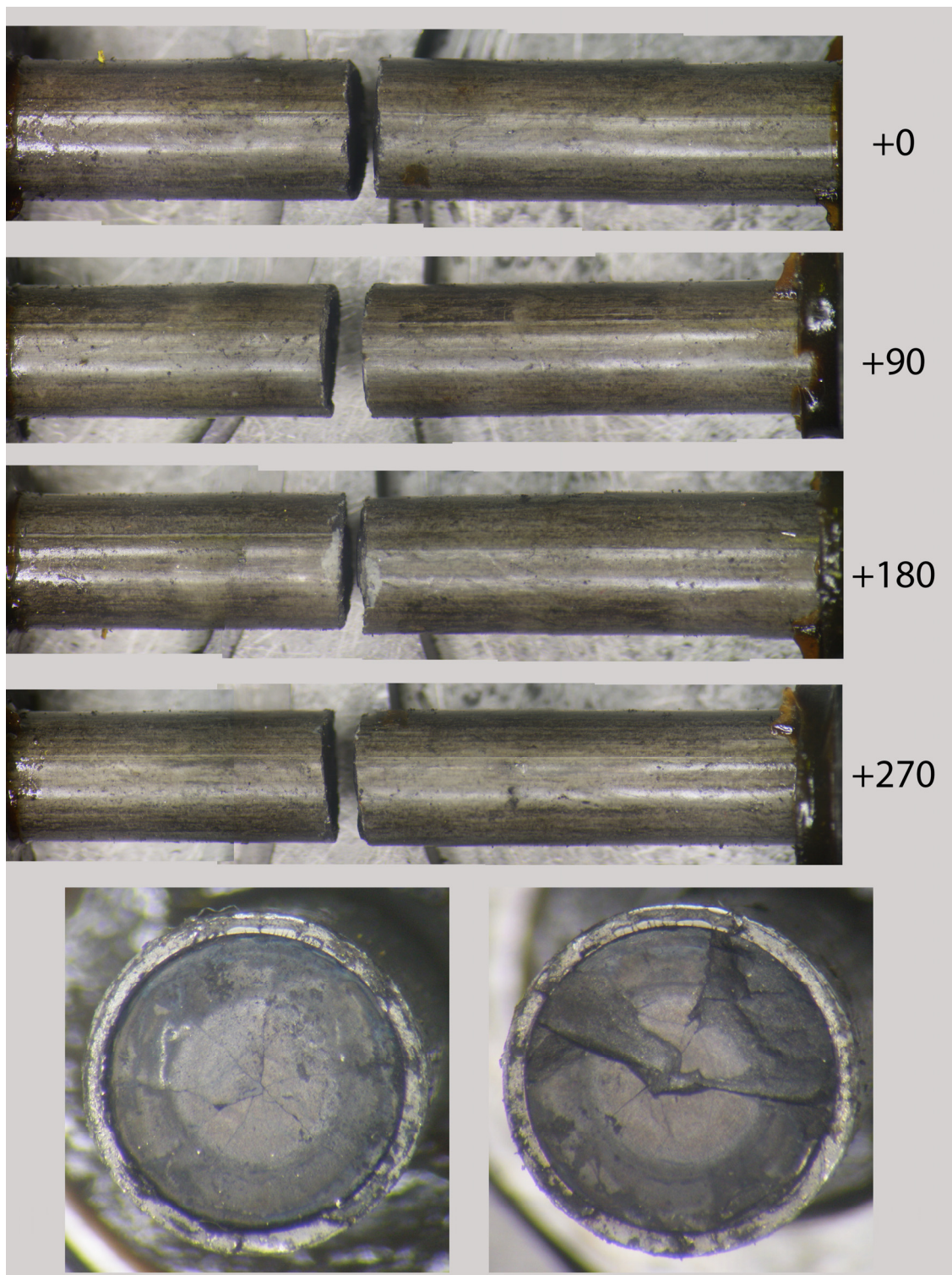


Figure F-22. 3D8E14-2963-3116 post-fatigue test condition.

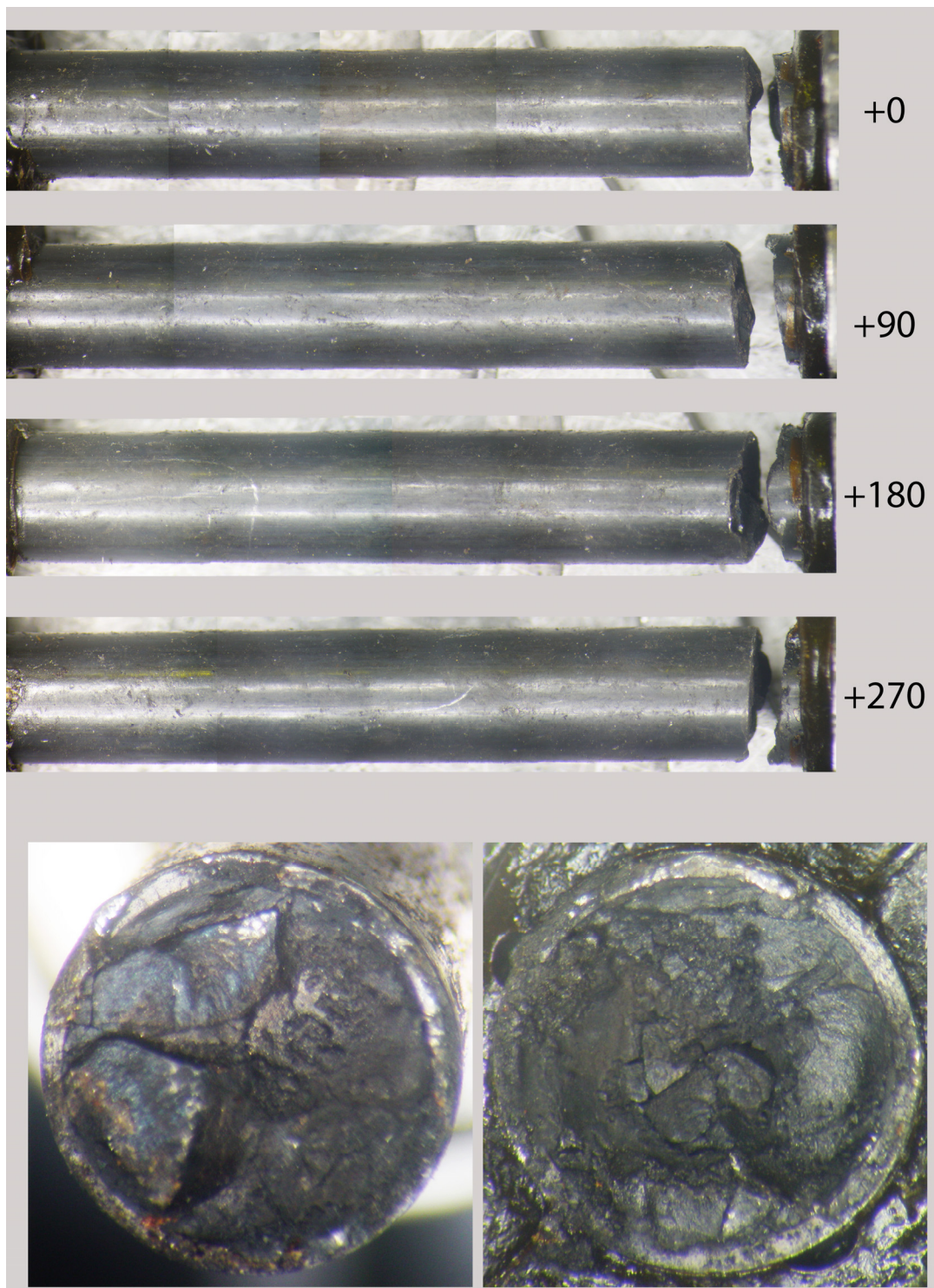


Figure F-23. 30AD05-2630-2783 post-fatigue test condition.



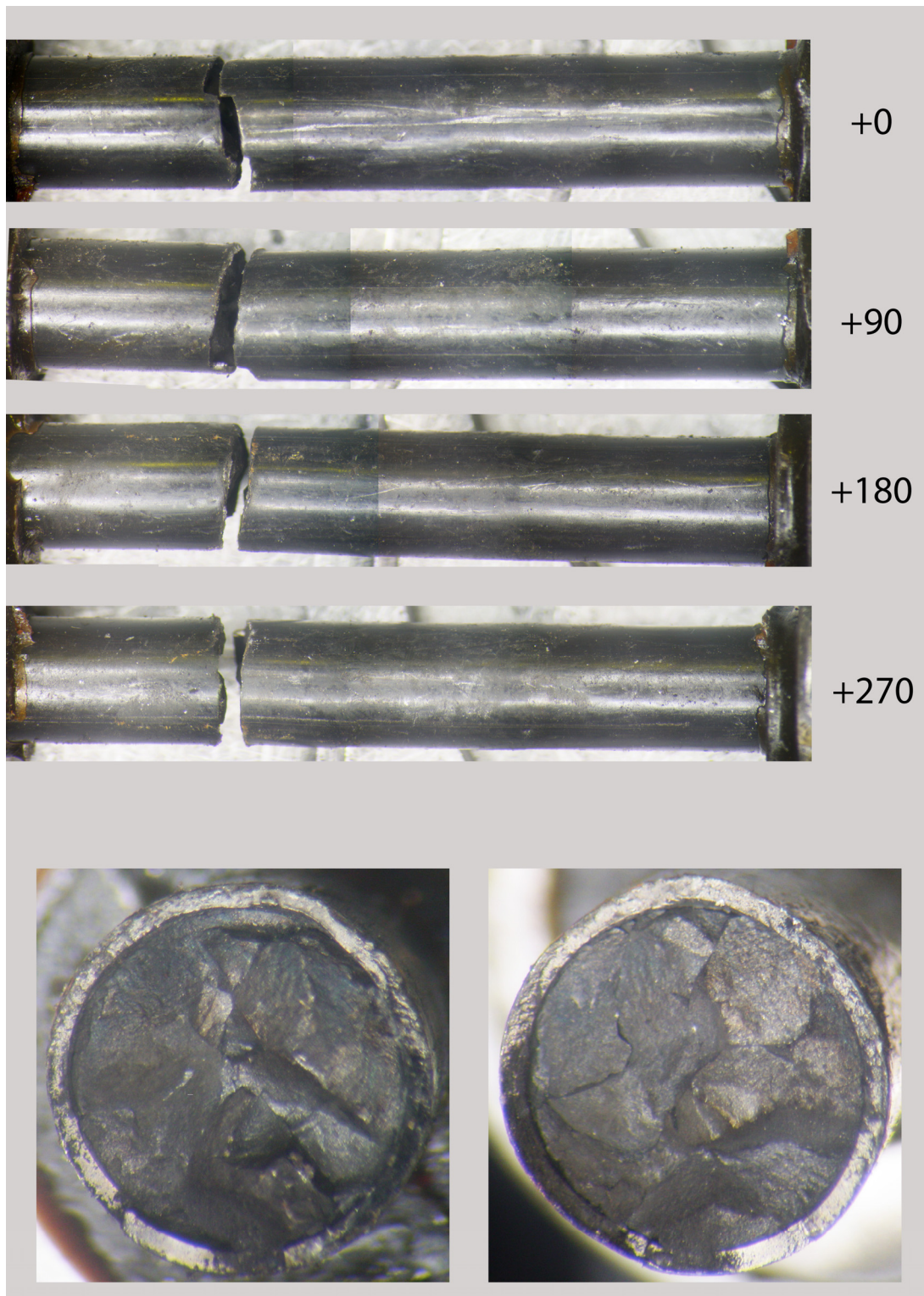
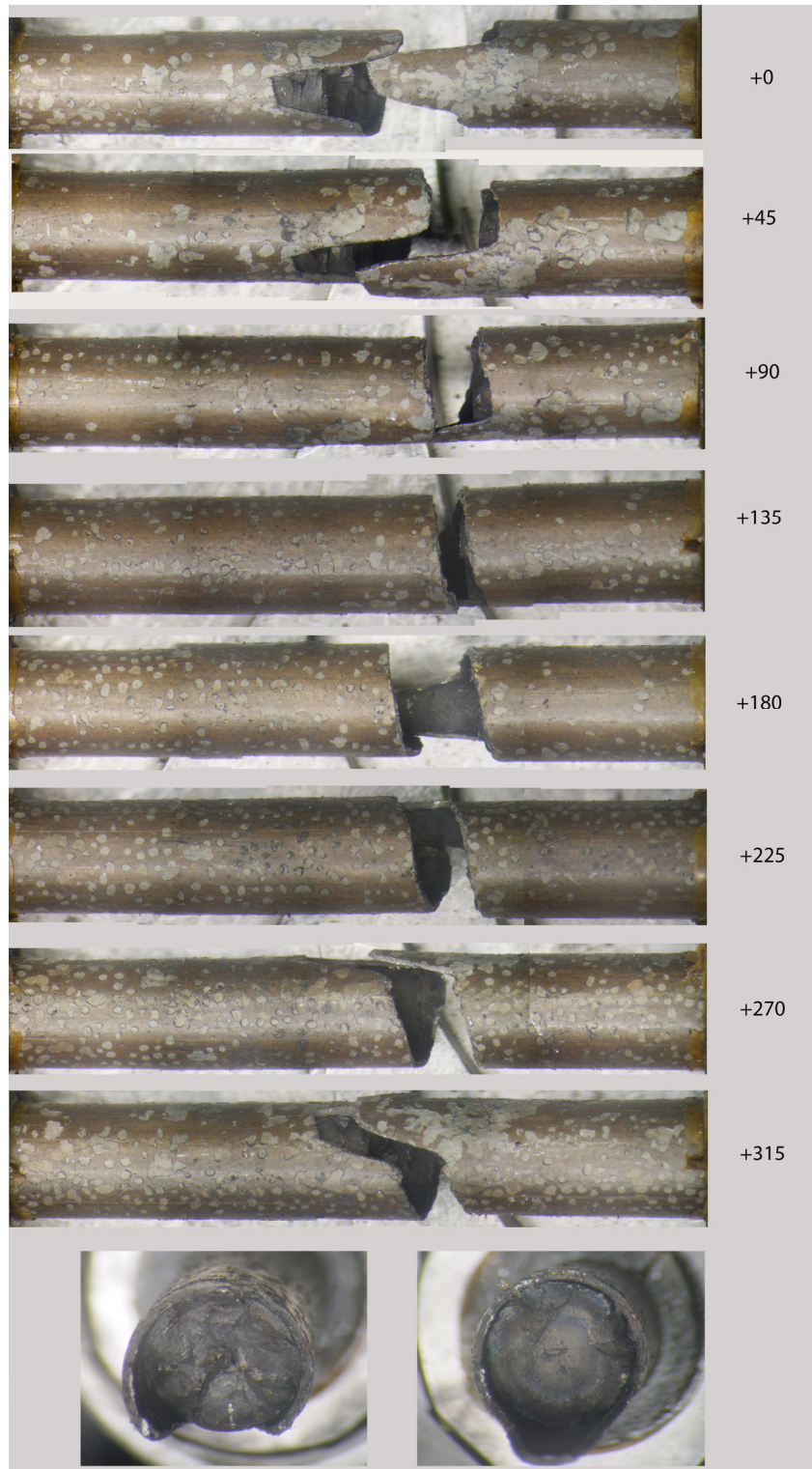


Figure F-24. 30AE14-0672-0825 post-fatigue test condition.



**Figure F-25. F35P17-1855-2008 post-fatigue test condition.**



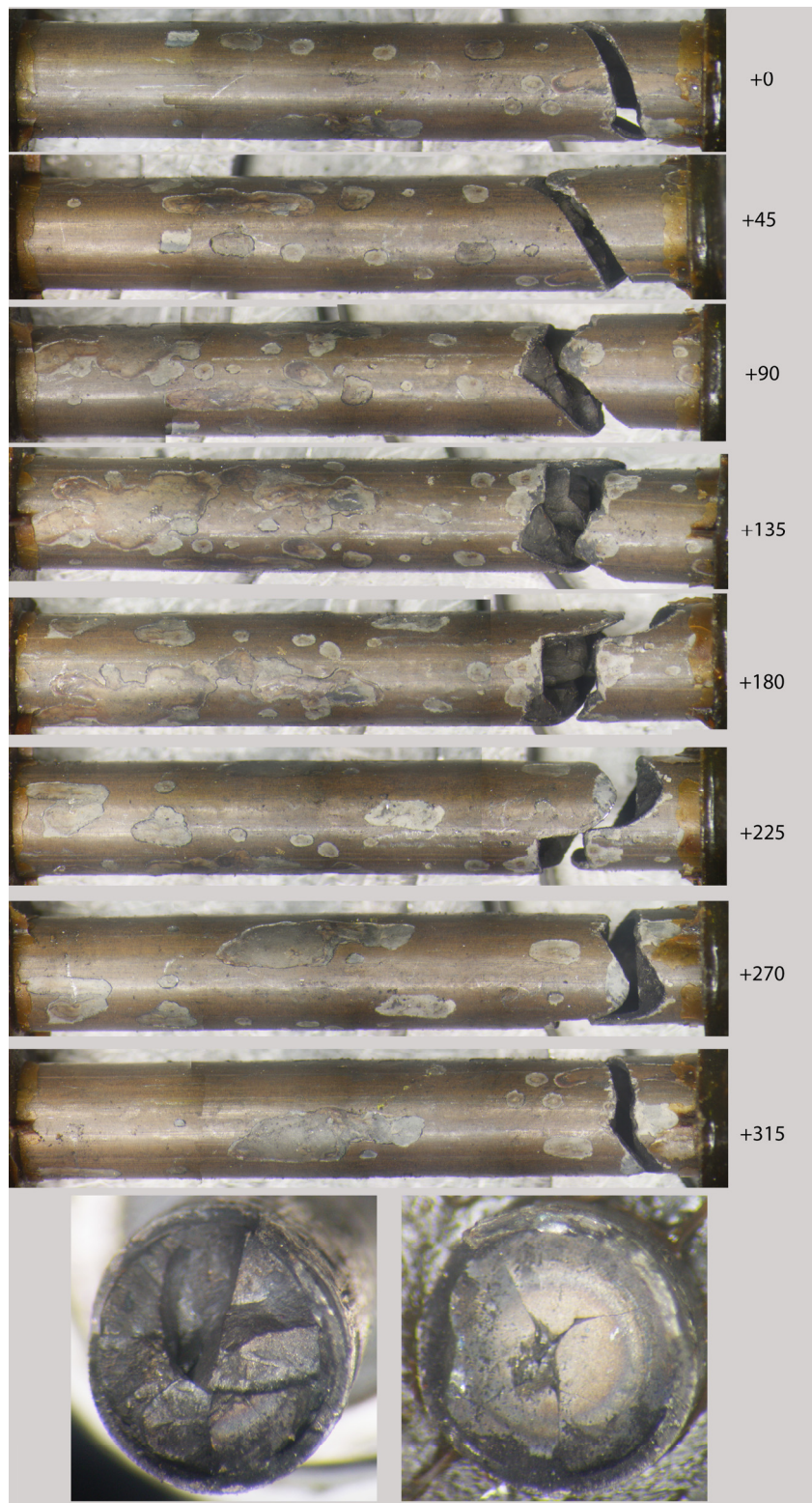


Figure F-26. F35P17-3159-3312 post-fatigue test condition.

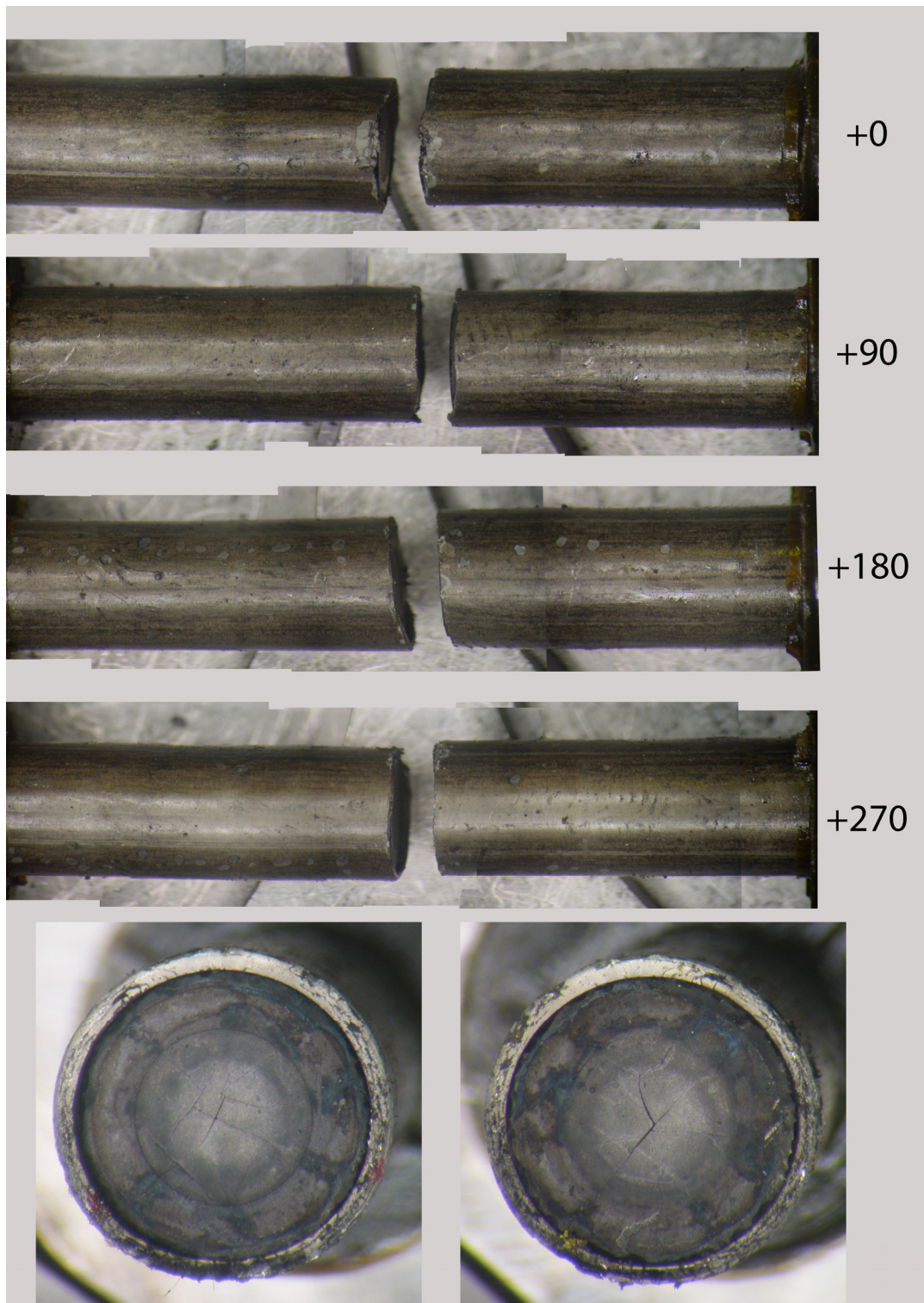


Figure F-27. 3A1F05-2025-2178 post-fatigue test condition.



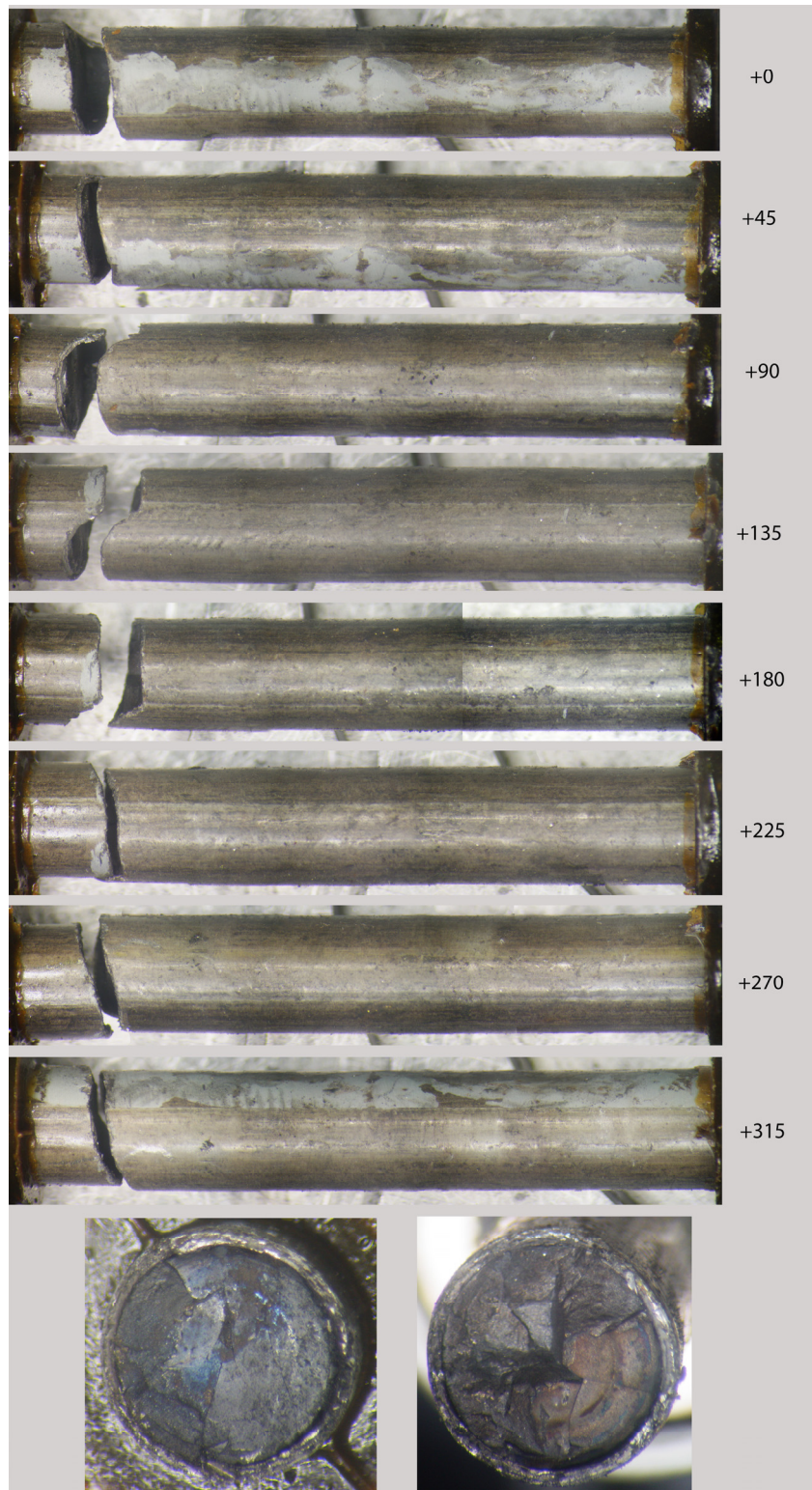


Figure F-28. 3A1F05-1853-2006 post-fatigue test condition.

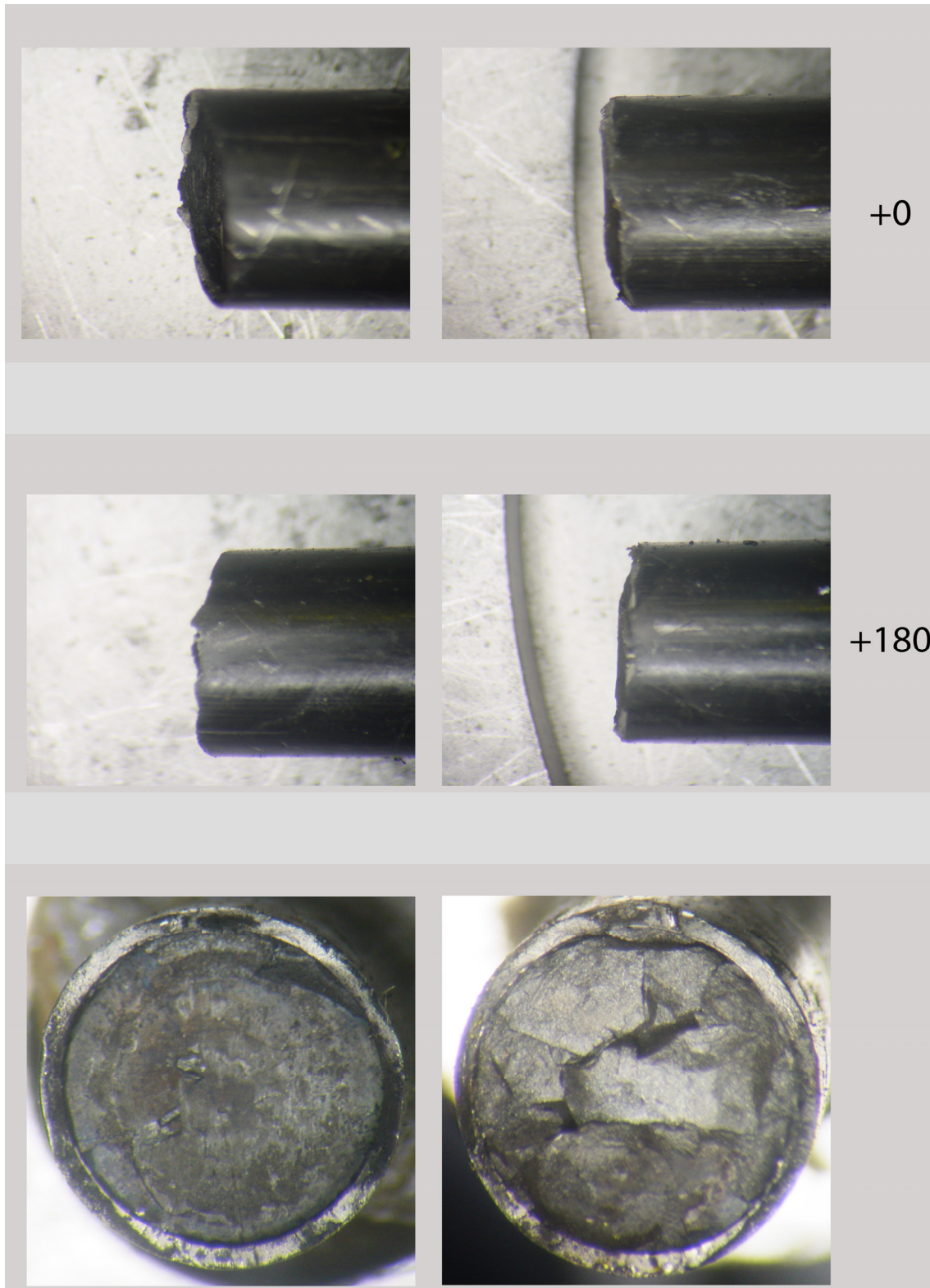


Figure F-29. 30AD05-0697-0850 post-fatigue test condition (broken ends only).



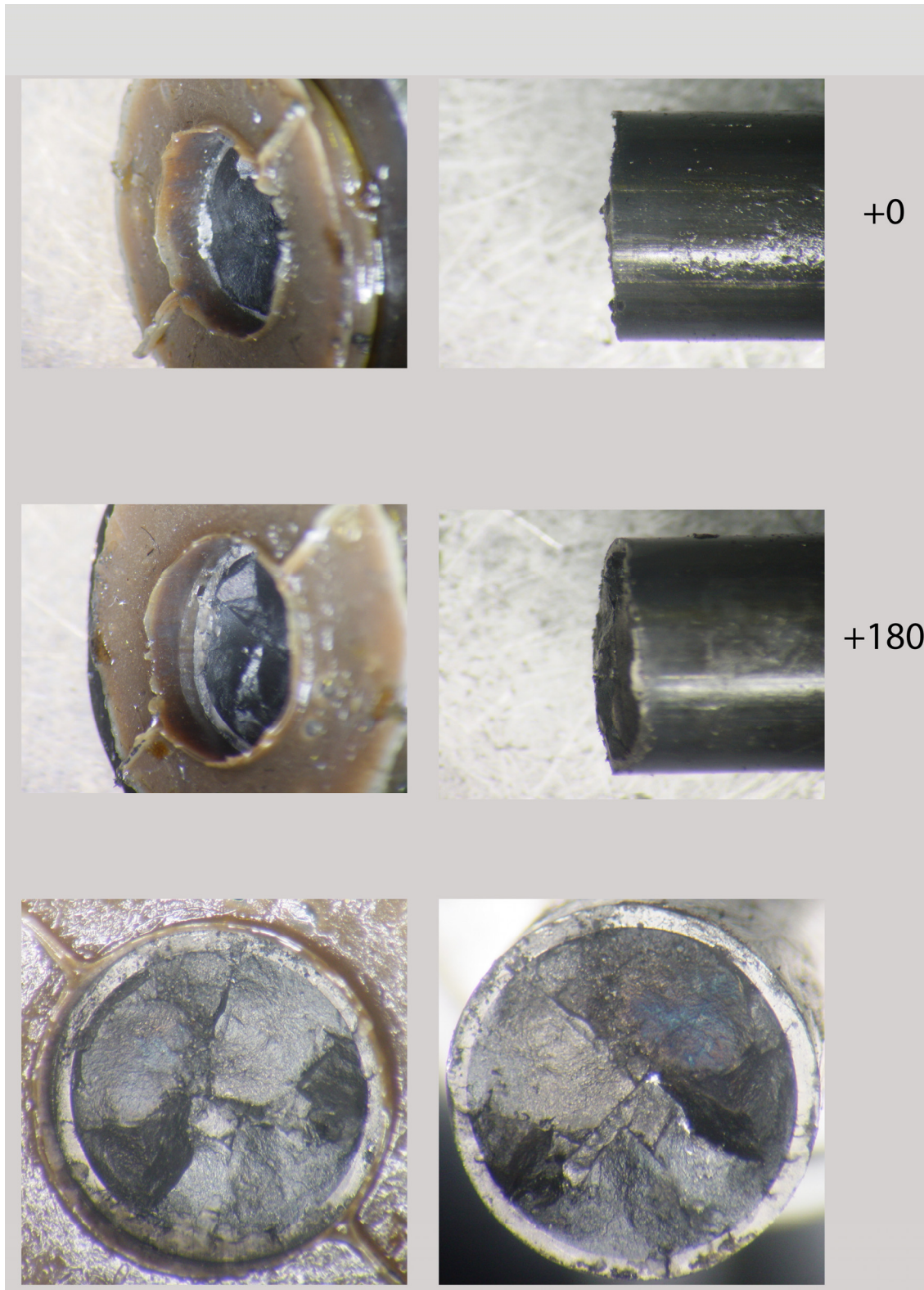


Figure F-30. 30AD05-2050-2203 post-fatigue test condition (broken ends only).

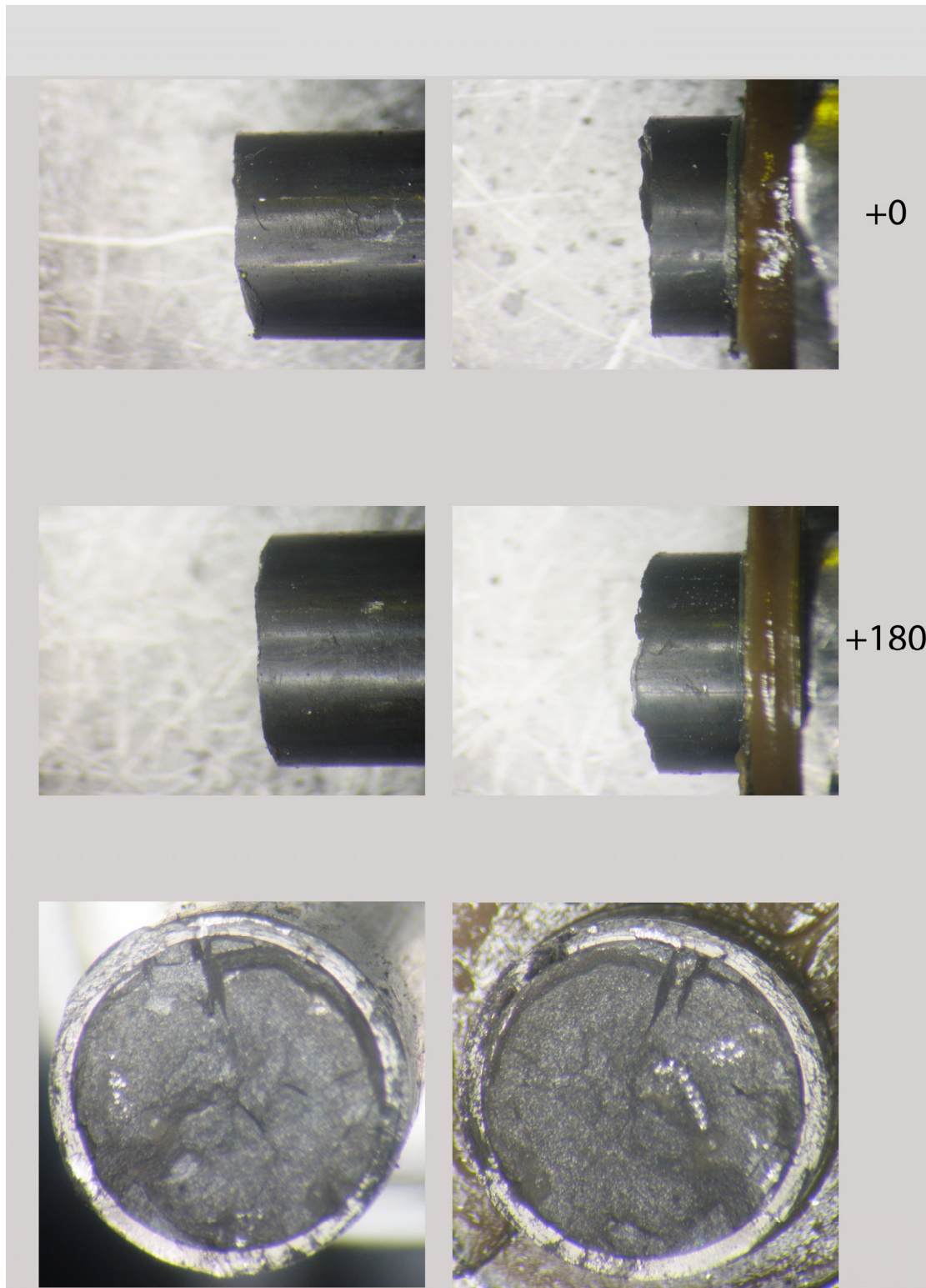


Figure F-31. 30AE14-2850-3003 post-fatigue test condition (broken ends only).



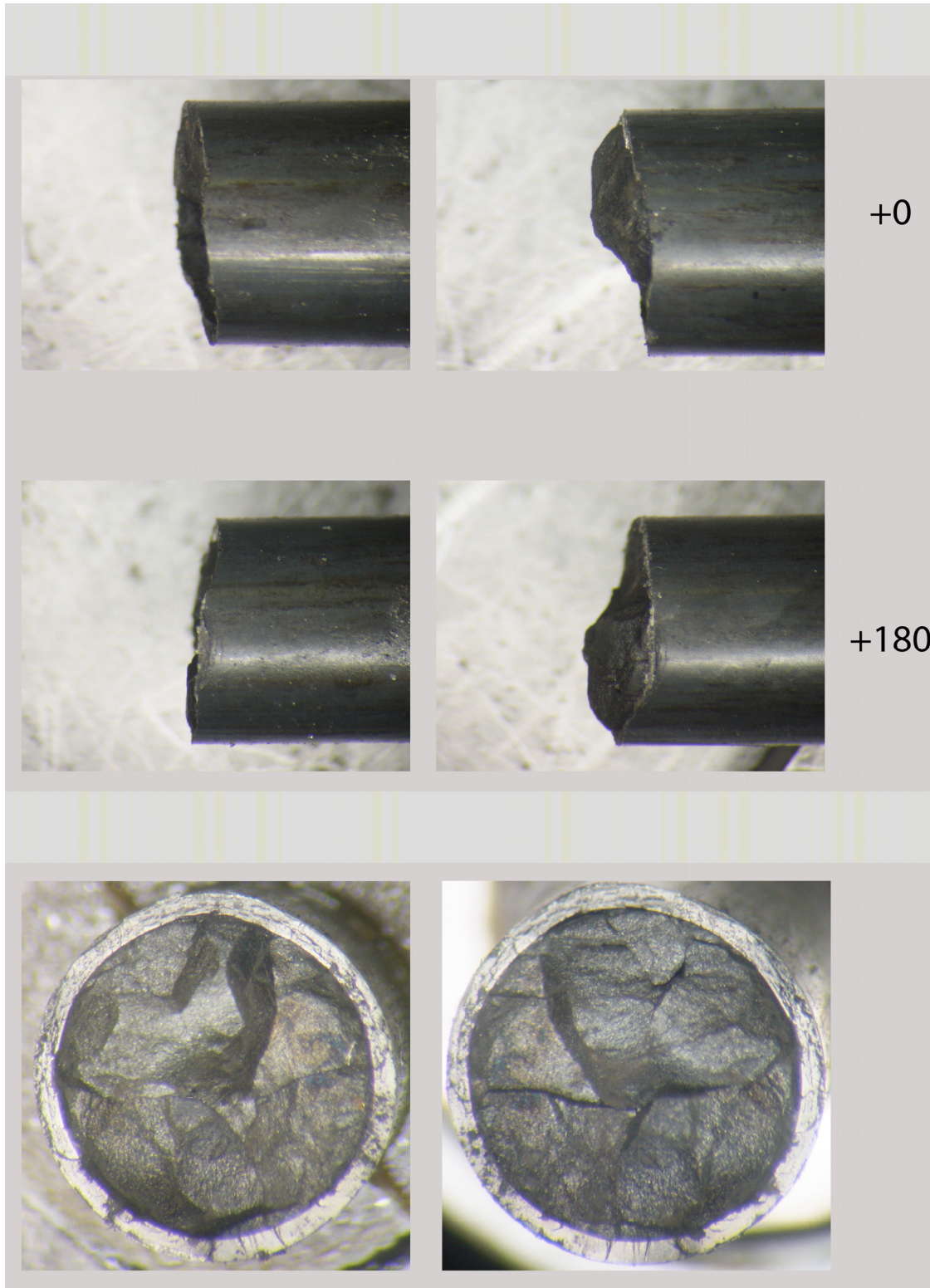


Figure F-32. 30AE14-3156-3309 post-fatigue test condition (broken ends only).

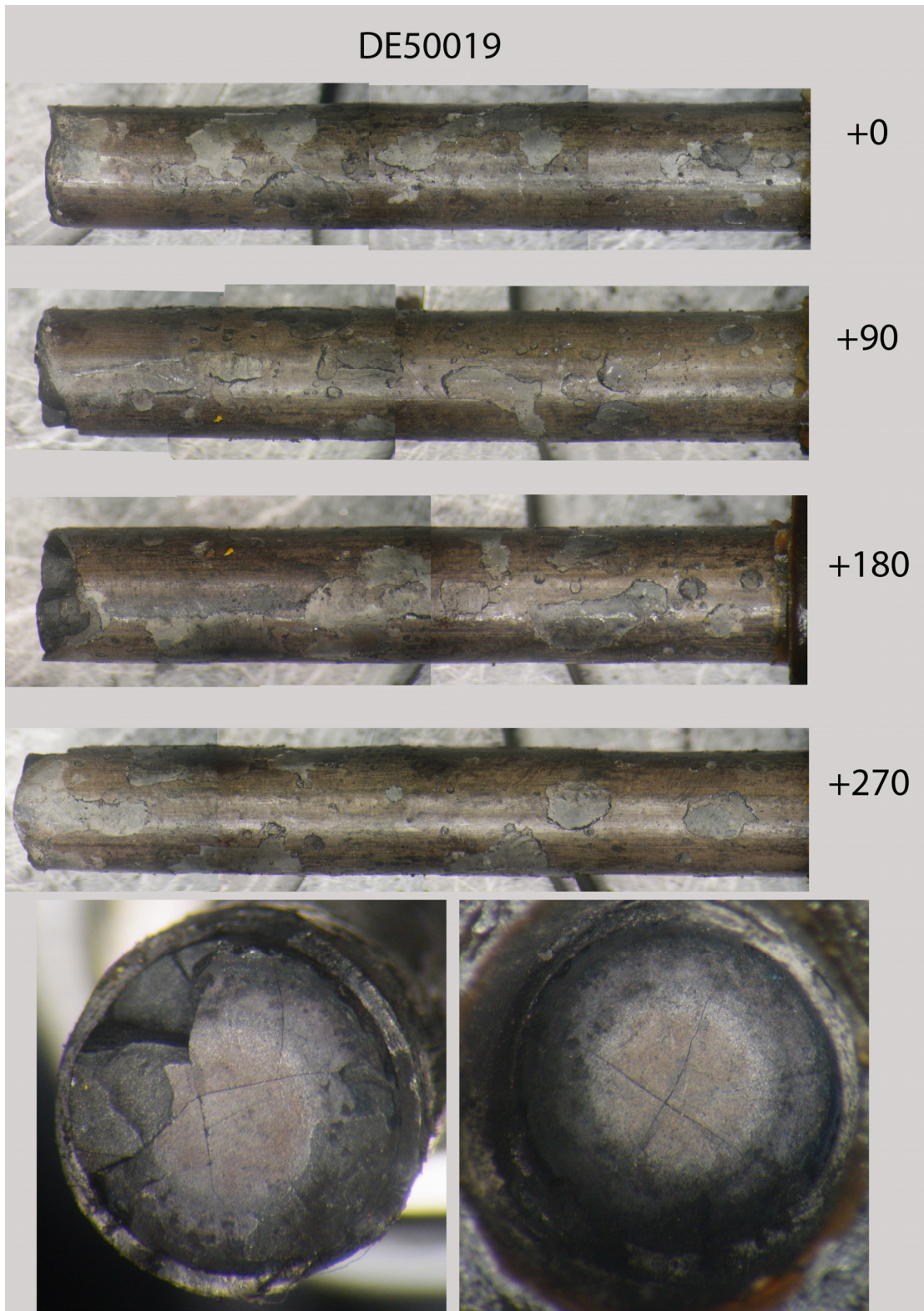


Figure F-33. 3A1F05-3214-3367 post-fatigue test condition.



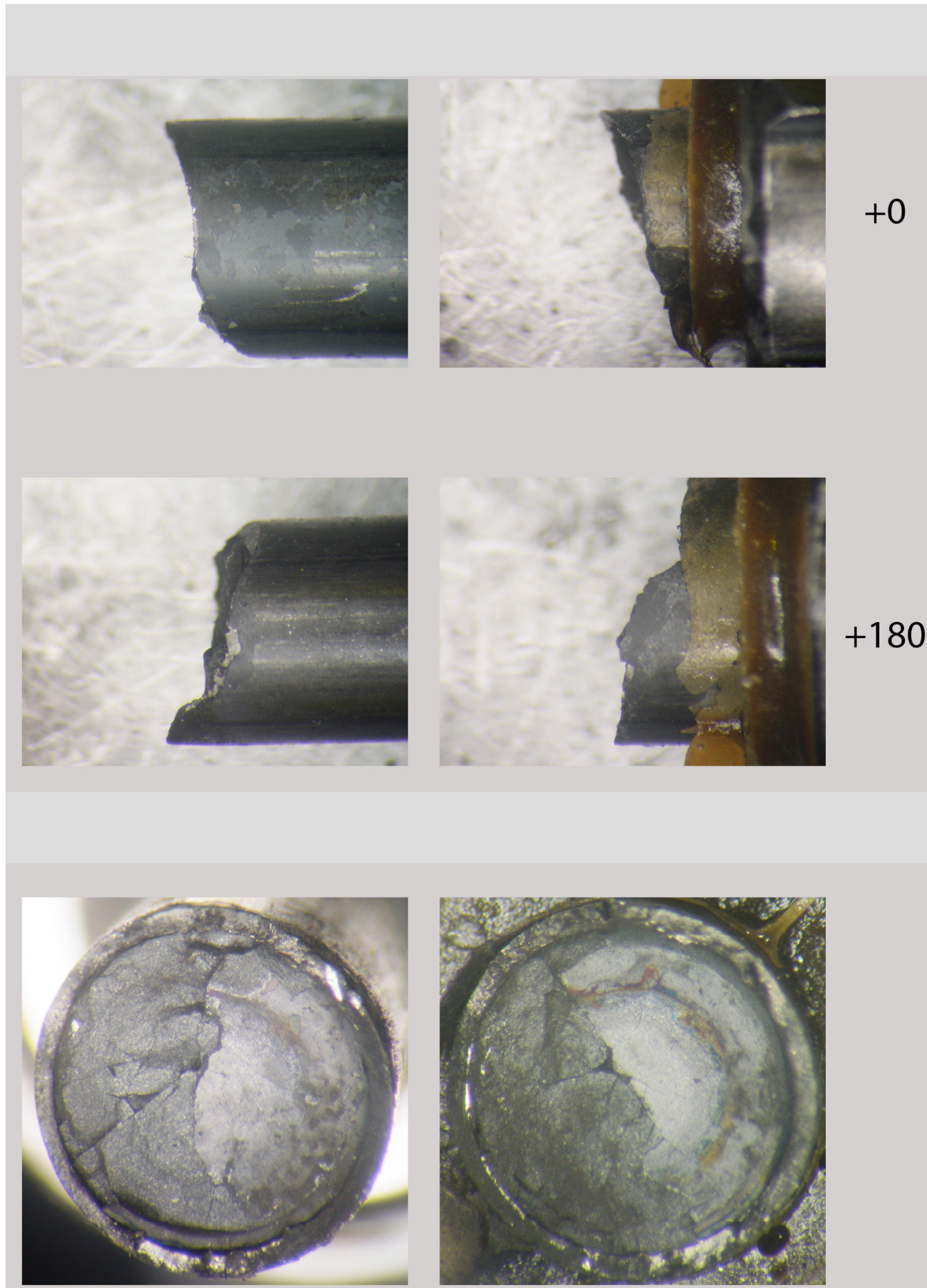


Figure F-34. 3D8E14-719-872 post-fatigue test condition.

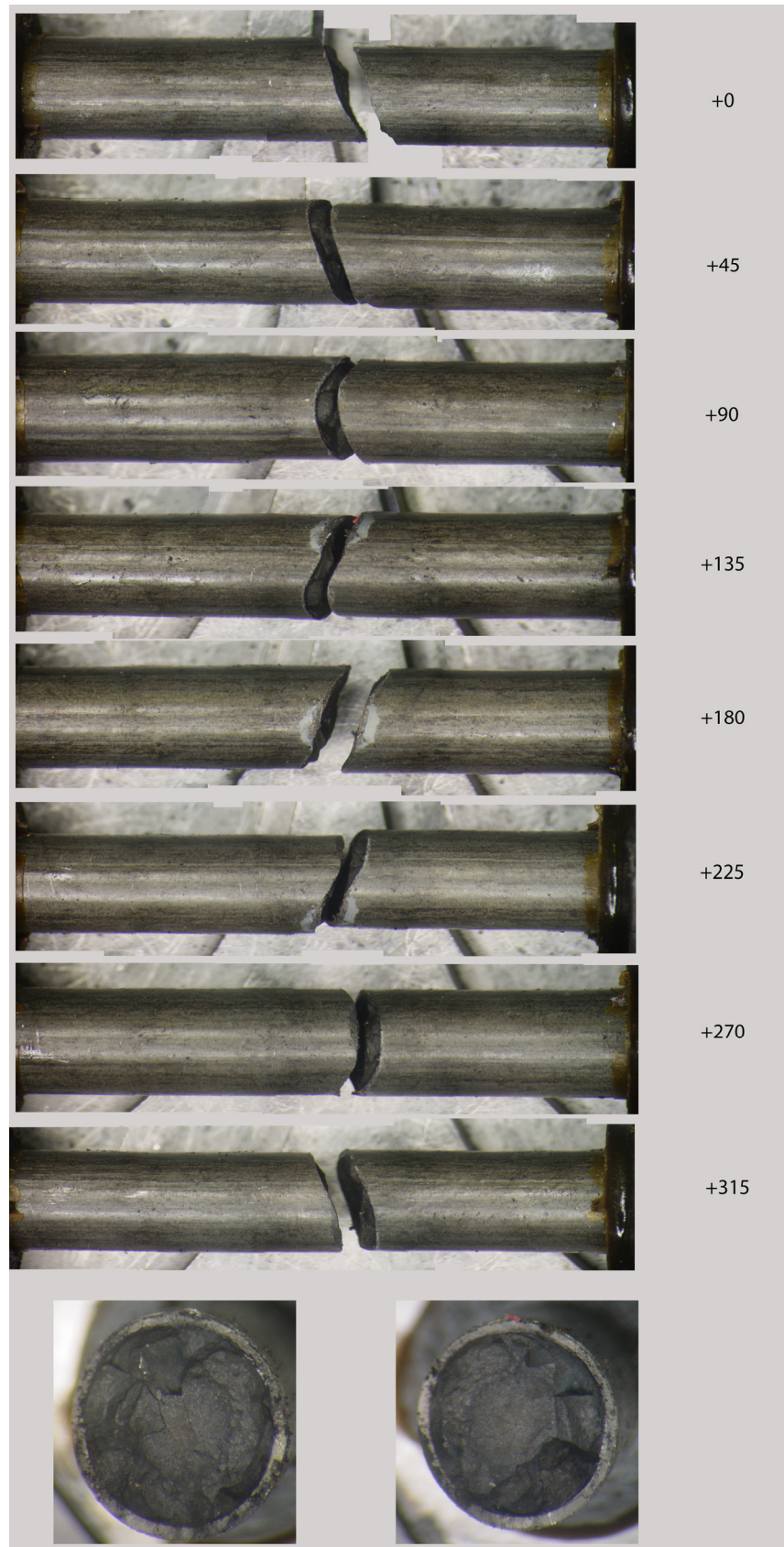


Figure F-35. 3D8E14-2412-2565 post-fatigue test condition.



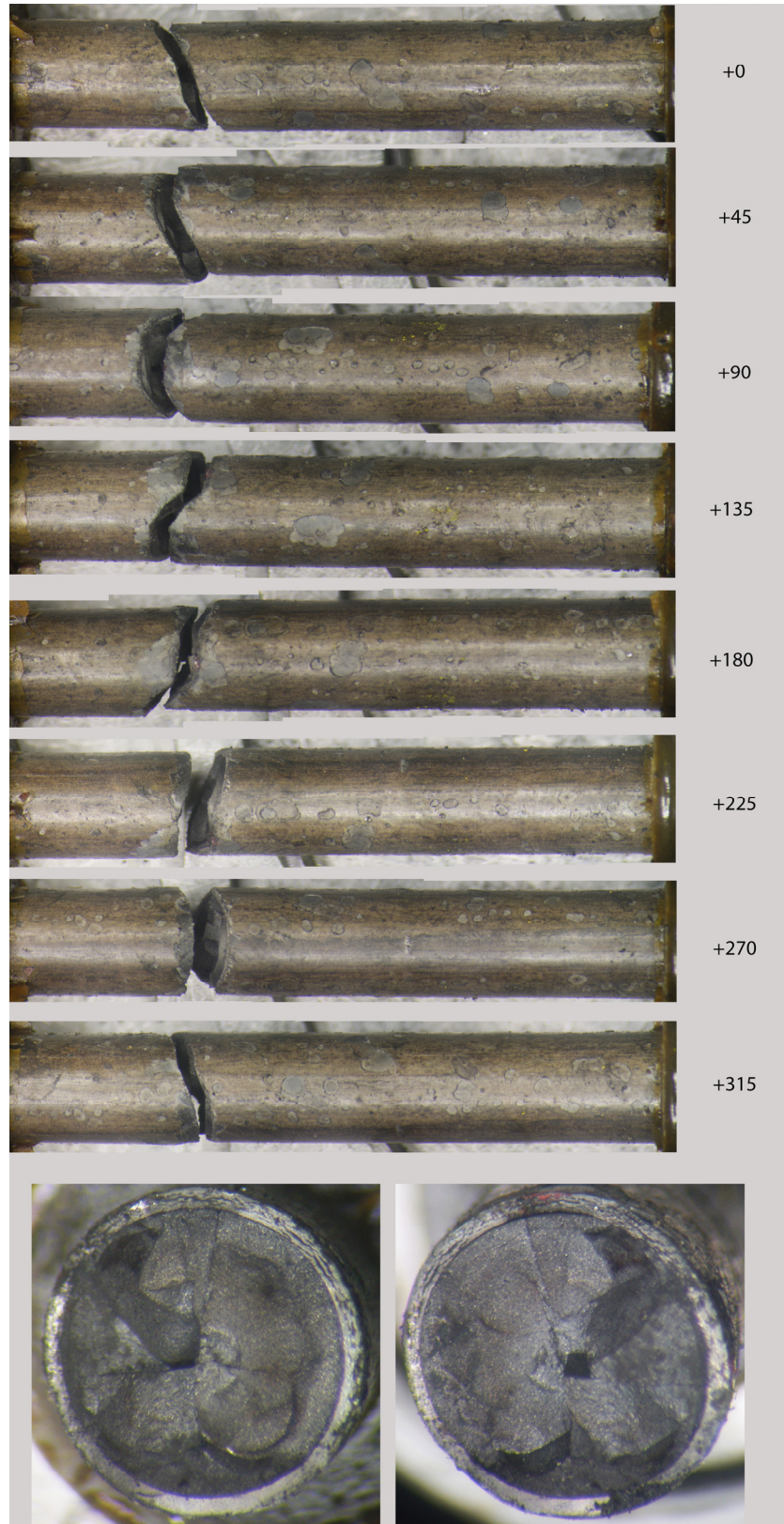


Figure F-36. 3A1F05-3367-3520 post-fatigue test condition.

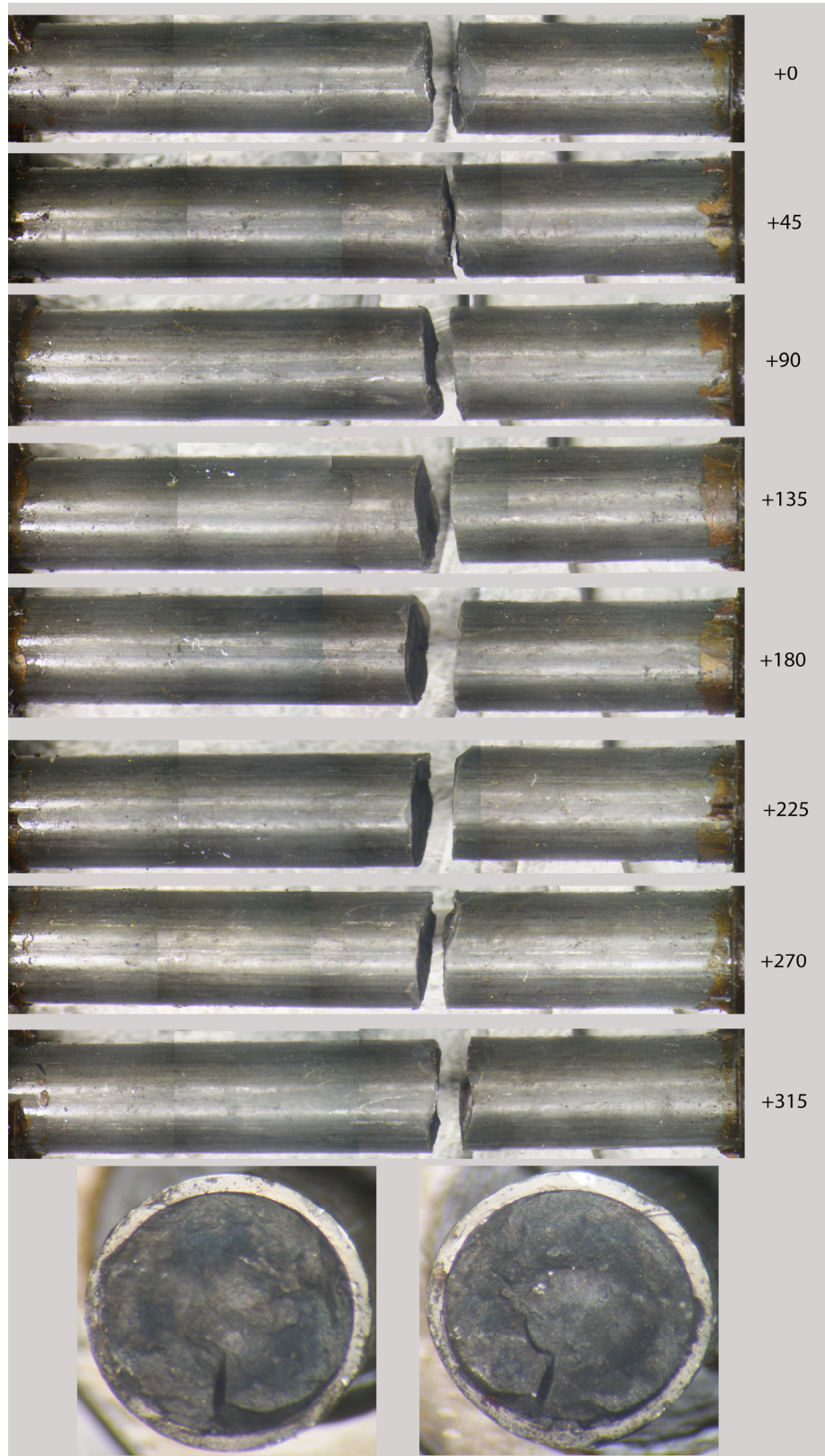


Figure F-37. 3D8E14-1178-1331 post-fatigue test condition.



## F-7.6 Scanning Electron Microscope (SEM) Characterization of Fracture

To gain insight into the fatigue failure mechanism, the fracture surfaces of a subset of the samples are being evaluated using SEM. There are several goals for the SEM characterization: (1) to provide a more thorough investigation of the two specimens that failed at a lower-than-expected-number of cycles, (2) to determine whether surface features like oxide spalling are associated with fatigue initiation, (3) to further investigate the role of pellet-pellet interfaces and pellet-clad bonding, (4) to determine the direction of fracture (from waterside to pellet-side, or vice versa), (5) to further investigate the role of precipitated hydrides in the fracture, and (6) to characterize the mode of fracture (brittle or ductile) and identify accessible materials. Table F-8 lists the samples to be characterized.

A CIRFT specimen is prepared for SEM characterization by cutting the tip off of one side of the fractured specimen. The cut is made a few millimeters from the fractured end, and the sample is then defueled. The sample is then attached to a metallic mount using conductive adhesive, avoiding the fracture surfaces. After curing, the sample is transferred out of the hot cell to the SEM enclosure. Once in the SEM, a montage of the entire circumference is created at a relatively low magnification ( $\sim 25\times$ ). The circumference is divided into four quadrants for imaging and identifying regions of interest.

At the present time, one sample from a CIRFT test that resulted in as-expected data (3D8E14-2963-3116) has been characterized via SEM. Optical images of this sample are provided in Figure F-22. This sample failed near the center of the CIRFT test gauge section, and its fatigue life (39,700 cycles) was consistent with previous test data. An observed decrease in the radius of curvature at  $\sim 34,500$  cycles indicates the initiation of a fatigue crack (see Figure F-38).<sup>a</sup>

The most distinct feature of 3D8E14-2963-3116's fracture surface is in the upper part of quadrant 1 near the boundary with quadrant 4 (Figure F-39 and Figure F-40). At the end of each CIRFT test, the specimen must be removed from the CIRFT machine. Often, the specimen has not fractured completely, and the fracture must be manually completed to remove it from the machine. An area in quadrant 1 was likely created after the fatigue test was stopped, during removal from the test equipment. At higher magnification (Figure F-40), the features near the center of the cladding wall have a classic ductile dimple appearance further suggesting the fracture surface was created as the specimen was removed from the equipment rather than during the fatigue test. In contrast, the features in quadrant 1 near the cladding ID appear more brittle-like, with ratchet lines typical of fatigue, indicating that these features were created during the fatigue test.

In quadrant 3 ( $\sim 180^\circ$  from the quadrant 1 region, Figure F-39), the features are flat compared to those in quadrant 1. This is the likely quadrant where the fatigue crack first initiated, and then wear of the surfaces followed as the test continued. High magnification of one area in quadrant 3 (Figure F-41) shows ratchet lines emanating from the cladding ID surface, suggesting that the fatigue crack initiated on the ID in this region.

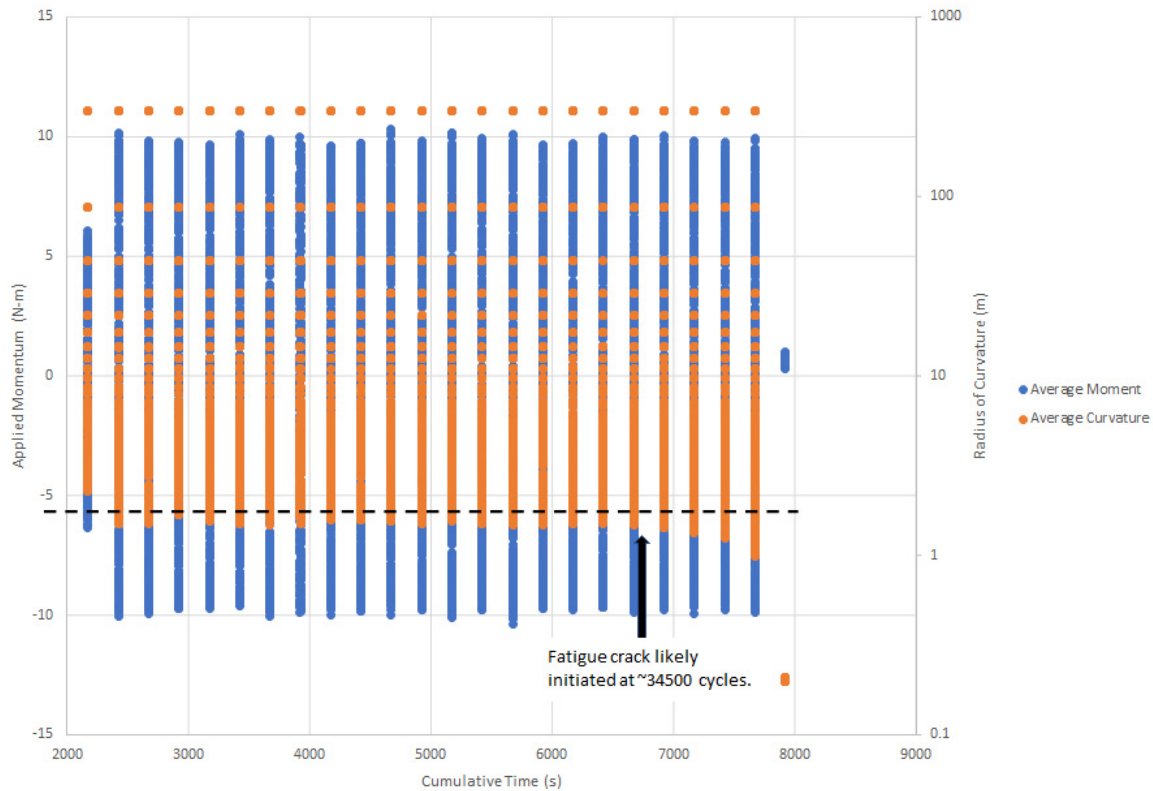
The high magnification images from quadrants 2 and 4 both show remnants of fatigue crack propagation in the form of fatigue striations (see Figure F-42 and Figure F-43). These images also show indications of circumferential cracks in both quadrants, which may be associated with propagation of the crack along precipitated hydrides. The flat area on the cladding ID in quadrant 4 may be a fatigue crack initiation site.

---

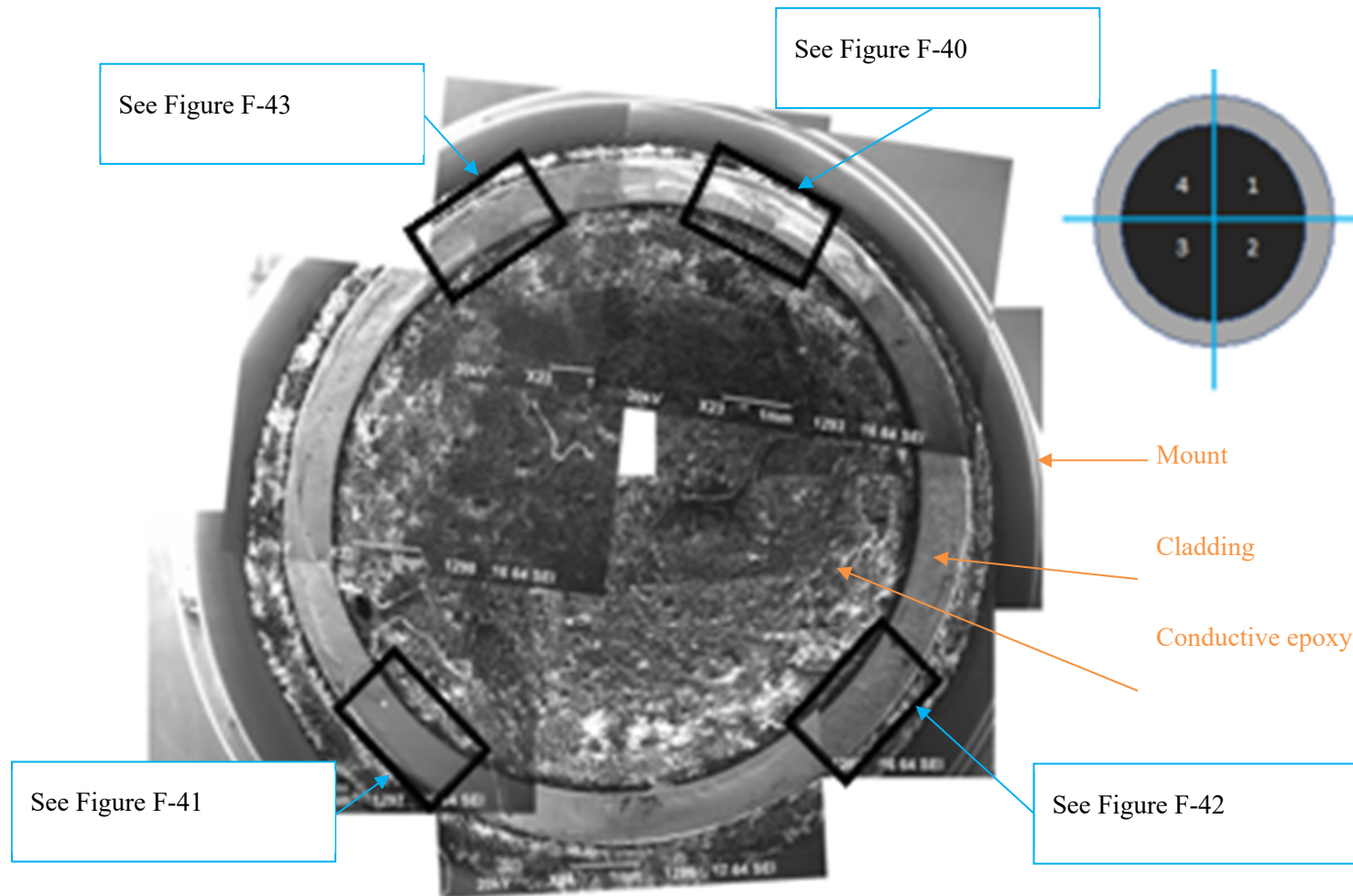
<sup>a</sup> Considering the uncertainty in the calculated radius of curvature, which is estimated as 0.3 m based on the uncertainty in the curvature given in Appendix G, the radius of curvature decreases more than the uncertainty at  $\sim 37,000$  cycles.

**Table F-8. CIRFT Specimens identified for SEM characterization**

Cladding material	CIRFT Specimen ID	Estimated specimen-average burnup (GWd/MTU)	Cycles to failure	Applied moment (N-m)
M5	30AD05-0697-0850	58	3,368	17.8
M5	30AD05-2050-2203	59	133,000	5.1
M5	30AD05-2630-2783	59	22,300	10.7
M5	30AE14-0672-0825	56	1,630	15.6
Zirc-4	F35P17-1855-2008	66	525	17.8
Zirc-4	F35P17-2027-2180	66	1,340,000	4.0
Zirc-4	F35P17-3159-3312	62	773	8.6
LT Zirc-4	3A1F05-3214-3367	48	3,450	8.8
LT Zirc-4	3A1F05-1853-2006	56	1,300	15.9
LT Zirc-4	3A1F05-2025-2178	56	48,200	8.8
ZIRLO	3D8E14-2412-2565	64	191,000	5.0
ZIRLO	3D8E14-2963-3116	62	39,700	8.7
ZIRLO	3F9N05-2329-2482	59	189,000	4.8
ZIRLO	6U3K09-2310-2463	59	1.75E+04	12.7
ZIRLO	6U3K09-3200-3353	50	3.49E+04	8.8



**Figure F-38. Applied moment and measured radius of curvature as a function of cumulative time for the final test session of 3D8E14-2963-3116. The decrease in radius of curvature is likely caused by the initiation and growth of a fatigue crack.**



**Figure F-39. 23X montage of the surface of the fatigue failure in sample 3D8E14-2963-3116. The areas identified in the various quadrants were investigated at higher magnification (see Figures F-40 to F-43).**



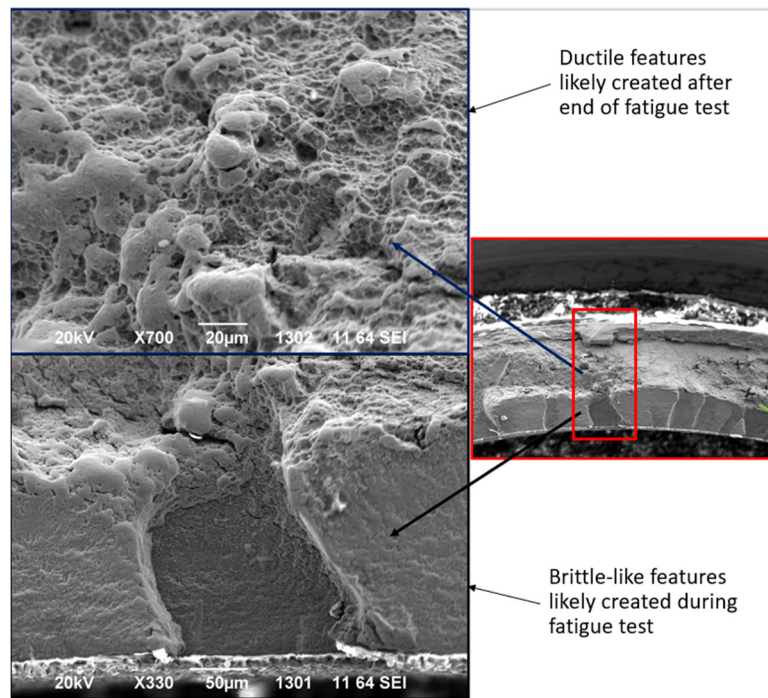


Figure F-40. 330× and 1,000× images of quadrant 1 in sample 3D8E14-2963-3116.

### Quadrant – 3

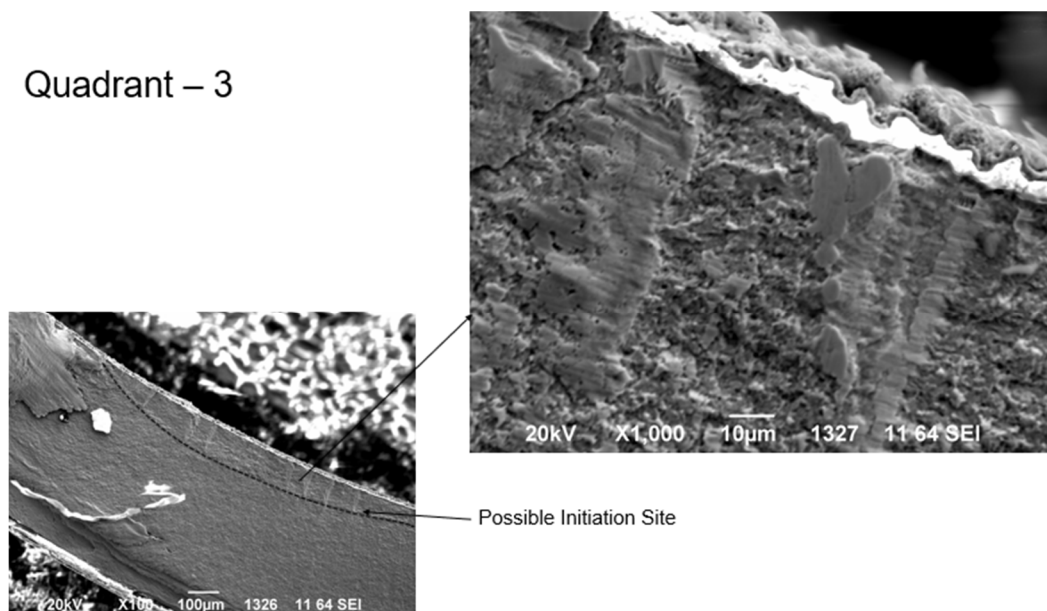
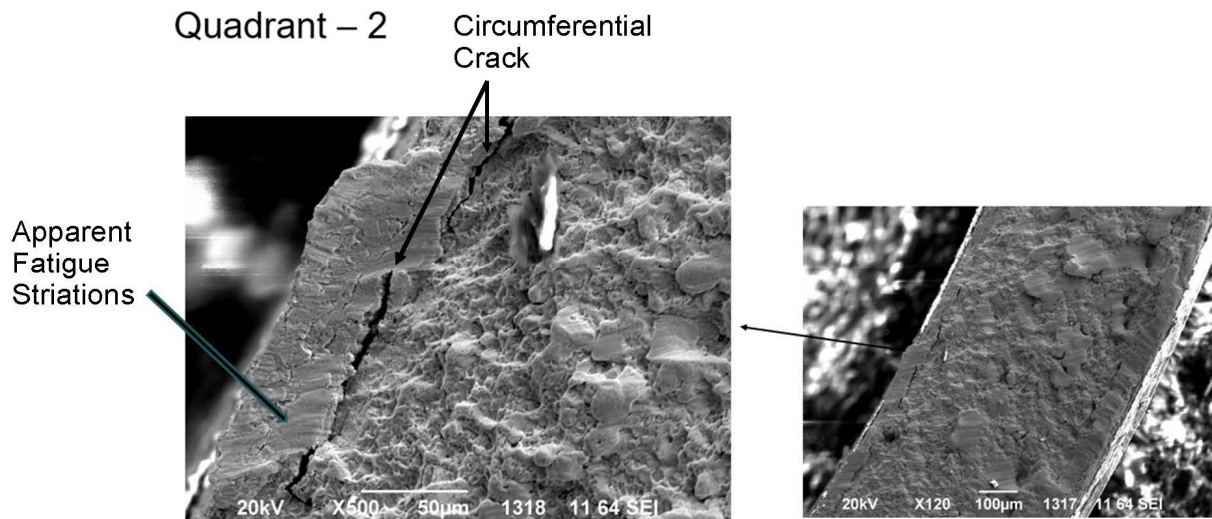
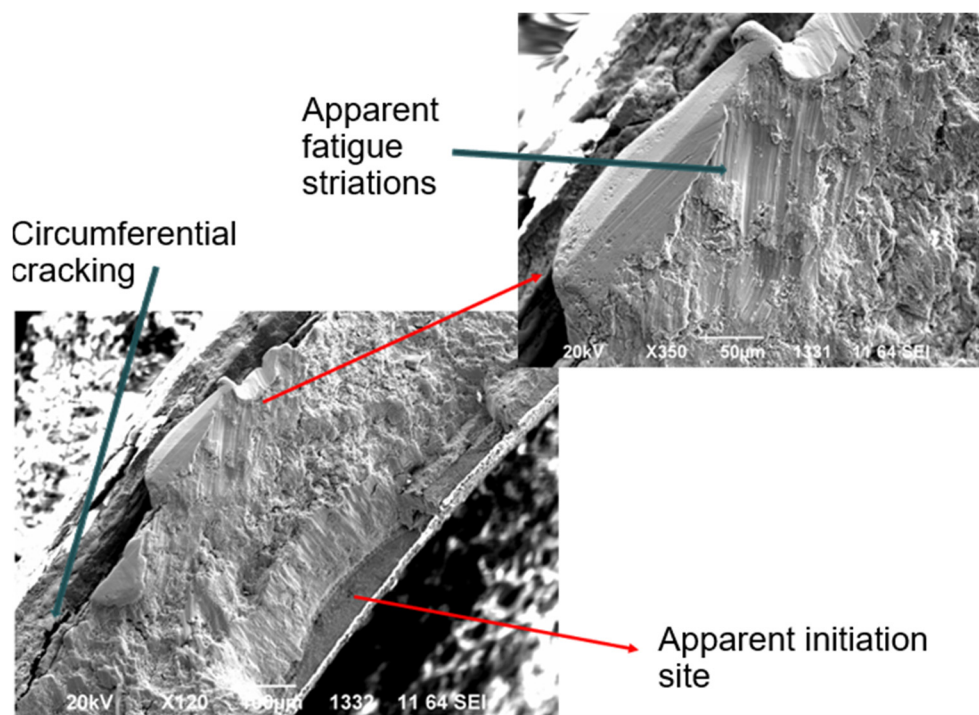


Figure F-41. 100× and 1,000× images of quadrant 3 in sample 3D8E14-2963-3116, approximately 180° from region in quadrant 1, that is suspected to have failed after fatigue test ended.



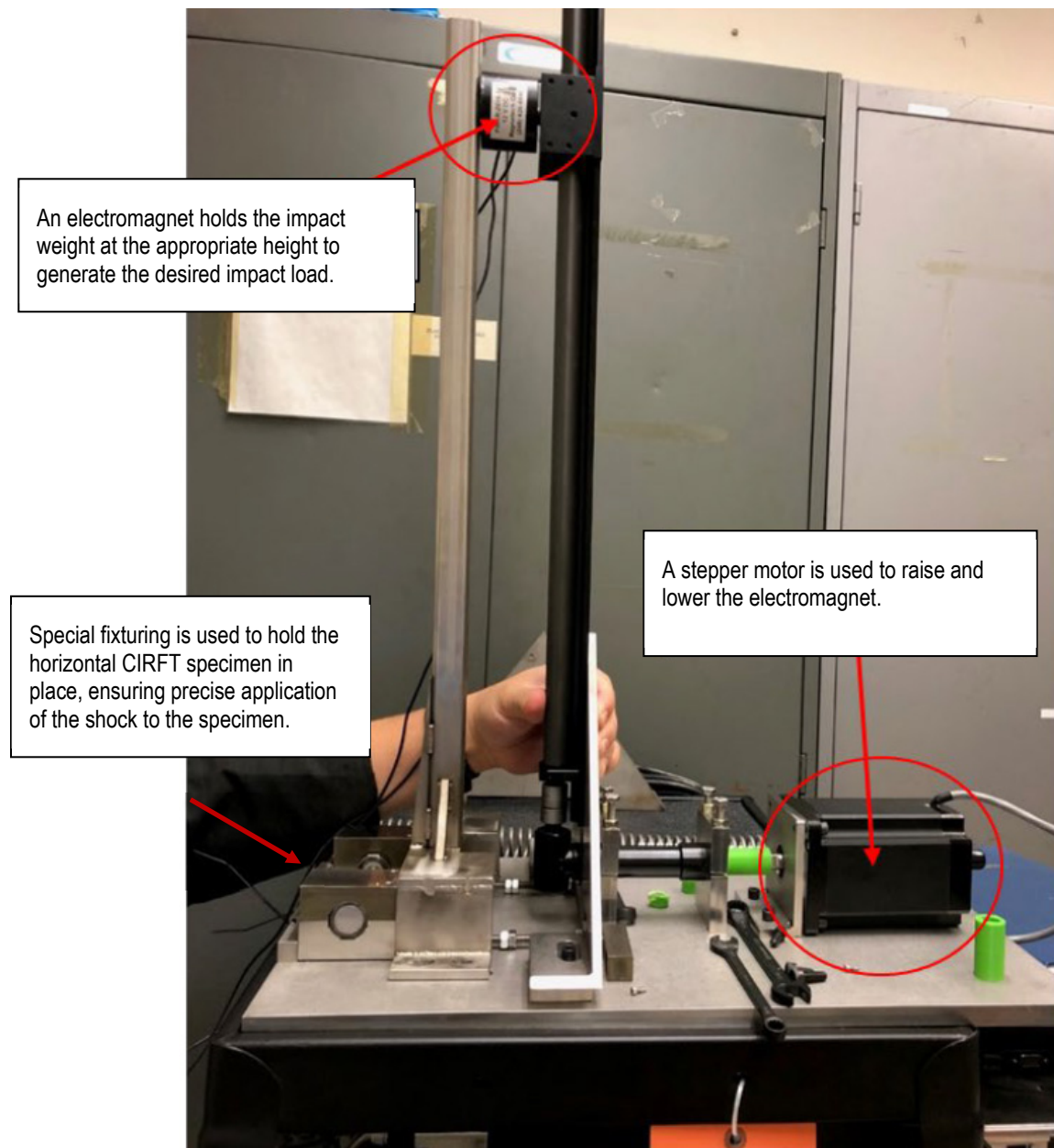
**Figure F-42. 120× and 500× images of quadrant 2 in sample 3D8E14-2963-3116, showing signs of fatigue striations typical of fatigue crack propagation, indicating propagation in the circumferential direction.**



**Figure F-43. 120× and 350× images of quadrant 4 in sample 3D8E14-2963-3116 showing signs of fatigue striations typical of fatigue crack propagation. The flatness of the feature on the cladding ID may be associated with fatigue initiation. There are also circumferential cracks near the cladding OD that may be associated with hydrides.**

## F-8. CIRFT Cumulative Effects Fixture Development

Equipment for performing the cumulative shock tests, as shown in Figure F-44, was developed and is currently being tested out-of-cell. The design incorporates an electromagnet and weight and uses gravity to deliver one or more impacts to the CIRFT specimen before fatigue testing. The parameters for the impact (e.g., impact load, number of impacts) have not yet been established. To help determine the necessary drop height, impactor weight, and impactor weight geometry for postulated normal condition impacts, a finite element model was developed for the impact system. The model and results are discussed in the following sections.



**Figure F-44. Cumulative shock fixture developed to apply a normal transport condition shock before fatigue testing.**

## F-8.1 Finite Element Modeling of the Cumulative Impactor

An impact analysis of the cumulative impactor was performed using a nonlinear dynamic FEA. Solid eight-node elements and shell four-node elements are used for all the models in which structure failure modes can be simulated during the impact.

The cumulative impactor model includes the impactor weight, a fuel rod test segment, and supports/restraints representing the lower bed of the impactor, as shown in Figure F-45. The fuel rod is supported by guide blocks at both ends. The cumulative impactor weight was centered over the rod and at a variable height above the outer surface of the cladding. Several different impactor end geometries were evaluated, including:

- a. a grid strip wall with dimples (shown in Figure F-45)
- b. a grid strip wall without dimples
- c. a rectangular weight only (the brown feature shown in Figure F-45)
- d. a plate with dimples
- e. a plate without dimples

These studies are focused on determining the g-load on the rod segment for various cumulative impactor conditions to determine whether such conditions reflect expected normal conditions of transport. Per Kalina et al. [F14], the normal condition g-loads experienced during transport of the SNF are less than 15 g and more typically less than 3 g.

### F-8.1.1 Finite Element Modeling Software

A nonlinear finite element model is developed using ANSYS Workbench. The dynamic analysis with time integration and contact configuration is used to solve the transient impact problem.

LS-DYNA, developed by Livermore Software Technology Corporation (LSTC), is a multipurpose explicit and implicit finite element program used to analyze the nonlinear response of structures. Its fully automated contact analysis and wide range of material models enable users worldwide to solve complex real-world problems. It is used by the automobile, aerospace, construction, military, manufacturing, bioengineering industries, and nuclear industries. LS-DYNA is optimized for shared and distributed memory on Unix-, Linux-, and Windows-based platforms, and it is fully qualified by LSTC. The code's origins lie in highly nonlinear, transient dynamic FEA using explicit time integration [F-15].

LS-DYNA has an extensive material library that includes metals, plastics, glass, foams, fabrics, elastomers, honeycombs, concrete and soils, viscous fluids, and user-defined materials.

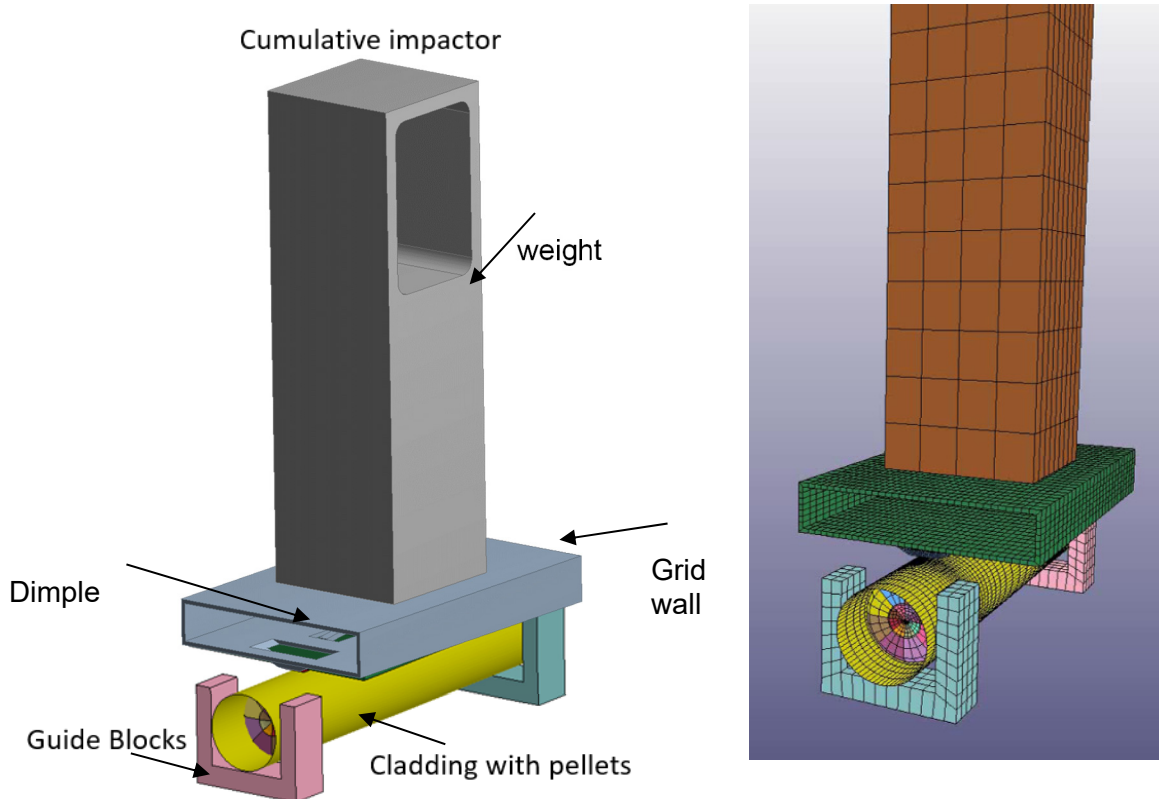
LS-DYNA has been widely used in various applications, including automotive crashworthiness and occupant safety, metal forming, aerospace (e.g., blade containment, bird strike, failure analysis), drop testing, nuclear shipping container design, metal cutting, earthquake engineering, offshore platform design, and sports equipment design.

Because impact is a transient structural dynamics problem that involves large deformation of solid structures and nonlinear material behavior, LS-DYNA is chosen to perform the impact analysis of the cumulative impactor.



### F-8.1.2 Finite Element Model

Structurally insignificant features such as small curves and lines such as fillets and chamfers were omitted from the finite element model. The omitted features are small and are not expected to significantly influence the structural response. The mesh element size near the impact zone was 0.5 mm; all other element sizes ranged from 0.5 to 2 mm. The cladding was modeled using linear shell elements.



**Figure F-45. The cumulative impactor CAD model (left) and finite element model (right) include a rod segment with discrete pellets, guide blocks, and a weight with impact geometry.**

The units and values used for the simulations are:

- mass, kg
- length, m
- time, s
- force, N
- stress, Pa
- energy, Joule
- density,  $\text{kg/m}^3$
- elastic modulus, Pa

The cumulative impactor was modeled as separate parts, with the surface-to-surface interfaces modeled using the bonded surface-to-surface connection. The surface-to-surface connections in the finite element model cannot deform, but they can break in accordance with the user-input stress criteria. The model uses various contacts to model the interaction between the elements. Automatic single-to-surface contact is an all-purpose contact used to model component interaction. Friction in LS-DYNA is modeled through the classic Coulomb friction model. In the cumulative impactor fuel rod segment model, contacts between the pellet-to-pellet and pellet-to-cladding contacts were assigned a static friction coefficient of 0.95 and a

dynamic friction coefficient of 0.85 to simulate a relatively rigid system. The friction values are being investigated with other models; these values might not be entirely representative of the actual frictional contact, but they are considered acceptable for the purposes of this work.

### F-8.1.3 Material Models

The cladding, spring, and dimples are modeled as Zirc-4; the pellets are modeled using a response profile similar to concrete, which is load-bearing in compression and has a lower strength in tension; and the cumulative impactor is modeled as stainless-steel. The pellets are modeled with a concrete material property as a surrogate for UO<sub>2</sub>. The compression strength of the pellets was 15 Mpa, with an aggregate grain size of 25.4 mm.

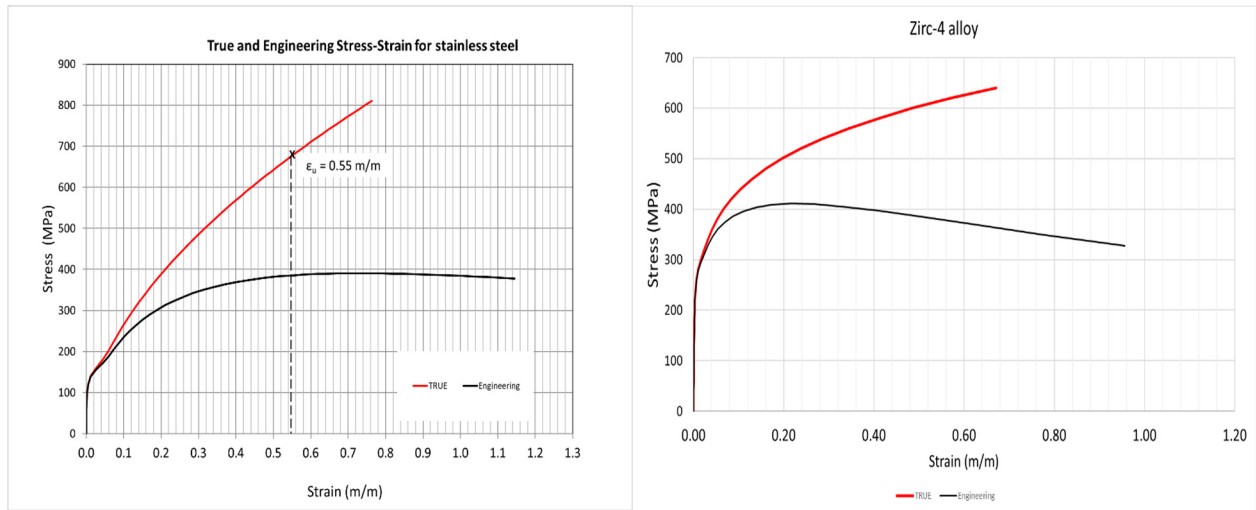
To model the plastic deformation of metal materials, the LS-DYNA code needs the true stress–strain curve of the material. Up to the maximum point on the engineering stress–strain curve, a uniform elongation and a uniform area reduction occur. The minimum true stress–strain curve used is based on the model provided in the American Society of Mechanical Engineers (ASME) Boiler and Pressure Vessel Code (BPVC) Sec. VIII, Div. 2, Annex 3-D [F-16], which uses the minimum yield stress, the minimum ultimate tensile stress, and elastic modulus of the material at the specified temperature. The true stress–strain curves obtained with this model are valid up to the value of the true ultimate tensile stress at true ultimate tensile strain.

The LS-DYNA material model used in the analysis is the \*MAT\_PIECEWISE\_LINEAR\_PLASTICITY, also known as \*MAT\_024. This material model prompts the user to specify the elastic modulus, Poisson’s ratio, yield stress, and failure strain of the material. When the calculated element’s plastic strain reaches the specified failure strain, the material has failed, and the element is deleted from the analysis. Additionally, the effective stress vs. plastic strain curve must be entered as a \*DEFINE\_CURVE entry.

Following the ASME model, a true stress–strain curve was developed for stainless steel and Zirc-4 using the minimum yield strength, minimum ultimate tensile strength, and elastic modulus of the material in Table F-9 [F-17]; the curve is shown in Figure F-46. Before the true stress–strain curve was entered into LS-DYNA, the elastic portion of the strain was subtracted from the total strain to develop the effective plastic strain used by LS-DYNA.

**Table F-9. Cumulative impactor model minimum material properties.**

Material properties				
Material	Minimum yield stress (MPa)	Minimum ultimate stress (MPa)	Elastic modulus (GPa)	Reference
304	106	392	172	[F-16, F17]
Zirc-4	241	413	99.3	[F-16, F-17]



**Figure F-46. 304 stainless steel (left) and Zirc-4 (right) true stress–strain curves used compared with corresponding engineering stress–strain curves.**

#### F-8.1.4 Initial Conditions, Boundary Conditions and Load Cases

All simulations were completed using room temperature material properties. A gravity load of  $9.81 \text{ m/s}^2$  was applied to all components in the finite element model. The guide rods were constrained in all three directions using the \*BOUNDARY\_SPC\_SET keyword. The fuel rod segment was placed on the guide blocks with full frictional contact.

#### F-8.1.5 Load Cases

The impact of the weight was studied using nine load cases, as listed in Table F-10, for each of the impactor end geometries. Load cases 1–4 correspond to a maximum cumulative impactor weight of 0.11 kg, with height increasing from 0.15 to 0.61 m (0.5 to 2.0 ft). Load cases 5–7 correspond to a 25% reduction in the cumulative impactor weight with increasing drop height. The cumulative impactor mass for load case 8 was reduced by 50% when compared with load case 1, and the drop height was 0.15 m (0.5 ft). Finally, for load case 9, the mass for the cumulative impactor was reduced by 75% when compared with load case 1, and the drop height was 0.15 m (0.5 ft).

**Table F-10 Cumulative tester FEA load case summary.**

Load case	Impactor mass (kg)	Impactor height (m)
1	0.107	0.15
2	0.107	0.30
3	0.107	0.46
4	0.107	0.61
5	0.080	0.15
6	0.080	0.30
7	0.080	0.46
8	0.053	0.15
9	0.027	0.15



## F-8.2 Results, Discussion, and Conclusions from the Cumulative Effects Fixture Modeling

The analysis focused on determining the g-load applied to the cladding when subjected to an impact from the cumulative impactor. The cladding g-load for each load case was extracted from the analysis and was plotted as a function of time. The system can dissipate the impact energy in three ways:

(1) rebound/deflection of the impactor, (2) bending deflection of the target rod segment, and (3) absorption into the rod cladding and pellets and supporting end blocks. End configurations (a) and (b), described in section F-8.1, resulted in a significant amount of rebound and the lowest g-load impacts. The concentrated load application in end configuration (c) resulted in rod segment bending, but the g-loads on the rod segment were extremely high. The plate type end configuration, (d) and (e), resulted in high shear loads on the rod segment near the guide blocks that are not considered representative of the target g-load of <15 g.

None of the combinations resulted in a g-load below 20 g. For example, the results from impactor end configuration (d), the plate with dimples, are provided. The impactor-applied g-load as a function of time is provided in Figure F-47 for load cases 1–4 and in Figure F-48 for load cases 5–9. For this impactor geometry, the initial impact takes less than 0.3 ms, after which the weight is rebounded. The g-load on the rod during the impact ranges from 781 to 3,298 g, as listed in Table F-11. Load case 4 has the highest drop height and heaviest weight, and it resulted in the maximum g-load because it had the largest potential energy when compared with the other load cases. Load cases 1, 8, and 9 resulted in a cladding g-load less than 800. All load cases resulted in g-loads greater than 500, with multiple shock waves on the cladding and localized plastic strain on the impactor weight dimples, as shown in Figure F-49.

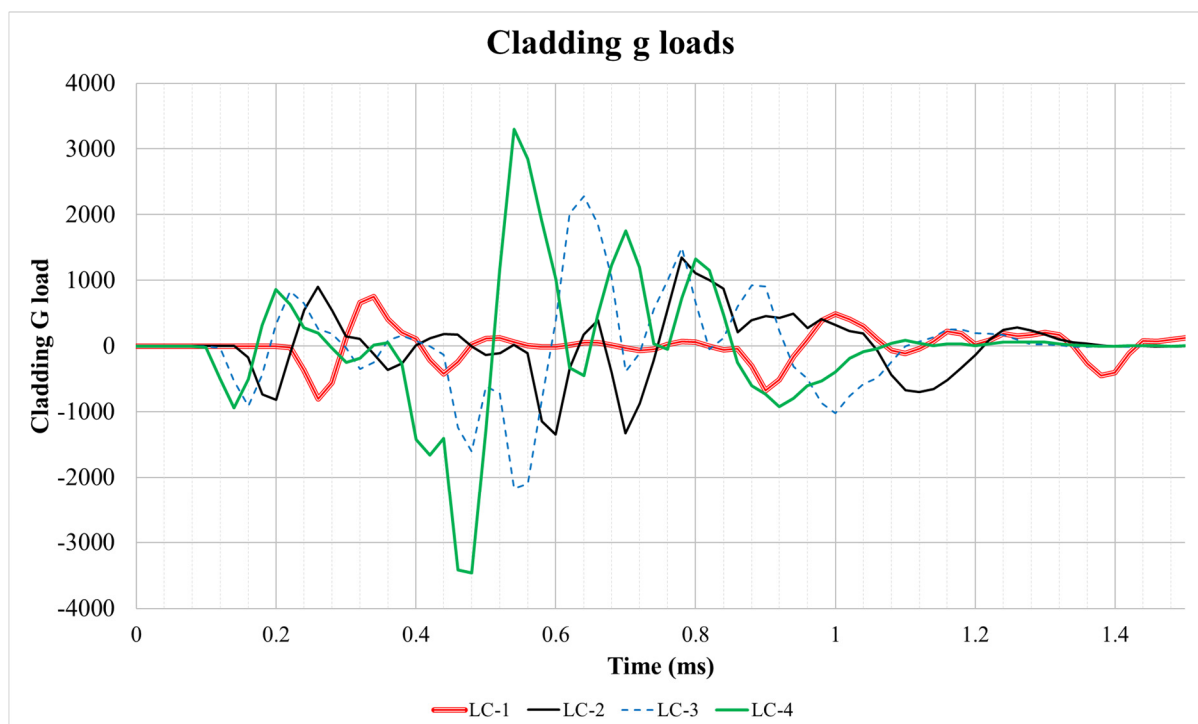
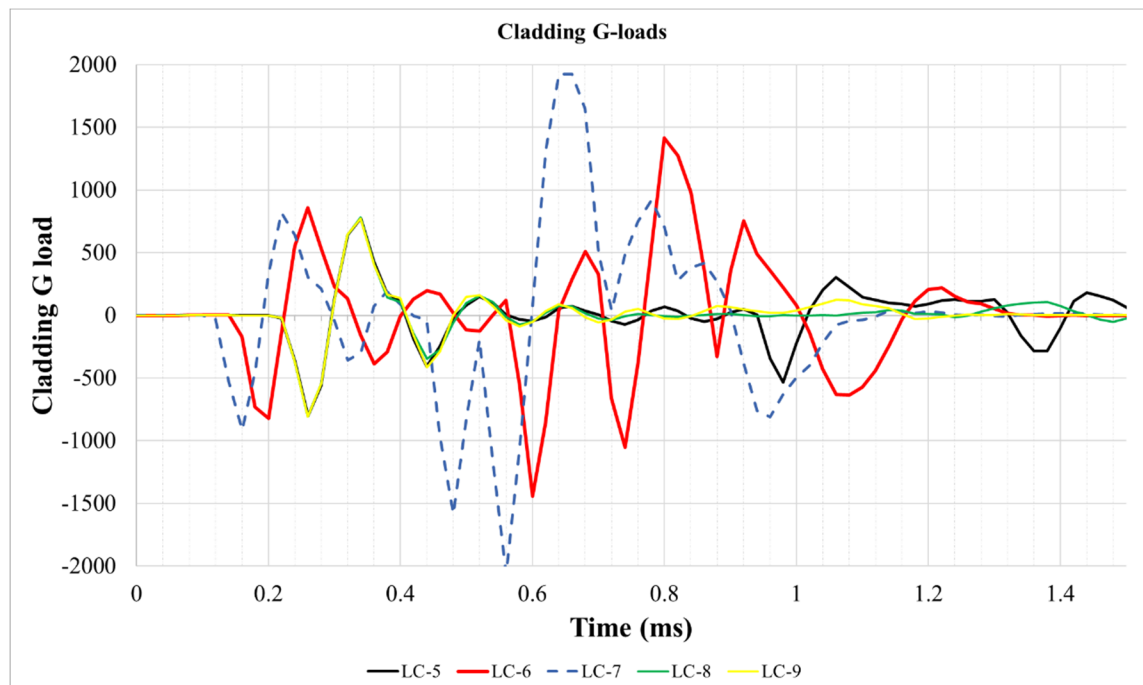


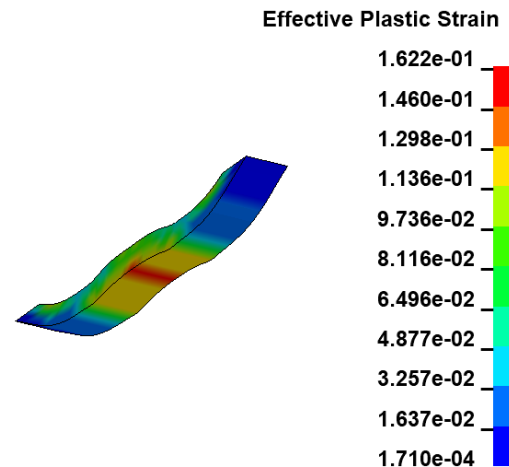
Figure F-47. Impactor end configuration (a) results for load cases 1–4.



**Figure F-48. Impactor end configuration (a) results for load cases 5–9.**

**Table F-11. Summary of fuel rod maximum g-load during impact with end configuration (a).**

Load case	Cladding maximum g-load
LC-1	754
LC-2	1,344
LC-3	2,279
LC-4	3,298
LC-5	774
LC-6	1,414
LC-7	1,925
LC-8	781
LC-9	773



**Figure F-49. Plastic strain occurred on the dimples for impactor end configuration (a).**

In addition to the permanent deformation of the impactor end dimples, configuration (a) also resulted in large rebound and fluttering of the grid wall portion of the impactor. Since these effects would produce uncontrolled variation in the impacts, this configuration was not appropriate for future cumulative shock testing prior to fatigue testing in CIRFT.

Based on the FEA, the main reason that the target g-load range cannot be achieved has nothing to do with the impactor itself. Rather, the problem is that the target rod segment is very stiff. It is necessary to prepare the segment for CIRFT testing by installing the heavy dogbone grips on each end. Only 50 mm of segment length is exposed for impact, as shown in Figure F-50. The dogbone provides a very stiff target that does not deflect in bending, so any impact will result in a high g-load, even with very low drop height, low impactor weight, and a soft impactor end configuration such as the dimples with a grid wall. With the dogbone as the target, low g-load impacts are not possible with the current fixture.



**Figure F-50. CIRFT dogbone.**

### F-8.3 Verification of FEA Results Using the Cumulative Effects Fixture

Physical tests using the cumulative effect fixture were completed as a verification of the FEA. A CIRFT dogbone surrogate with stainless-steel cladding and ceramic pellets was constrained in the specimen holder, as shown in Figure F-51. Various impactors with masses ranging from 355 to 47 g were used for the tests. These impactors had end geometries designed to mimic grid dimples, but they were solid, as shown in Figure F-52.

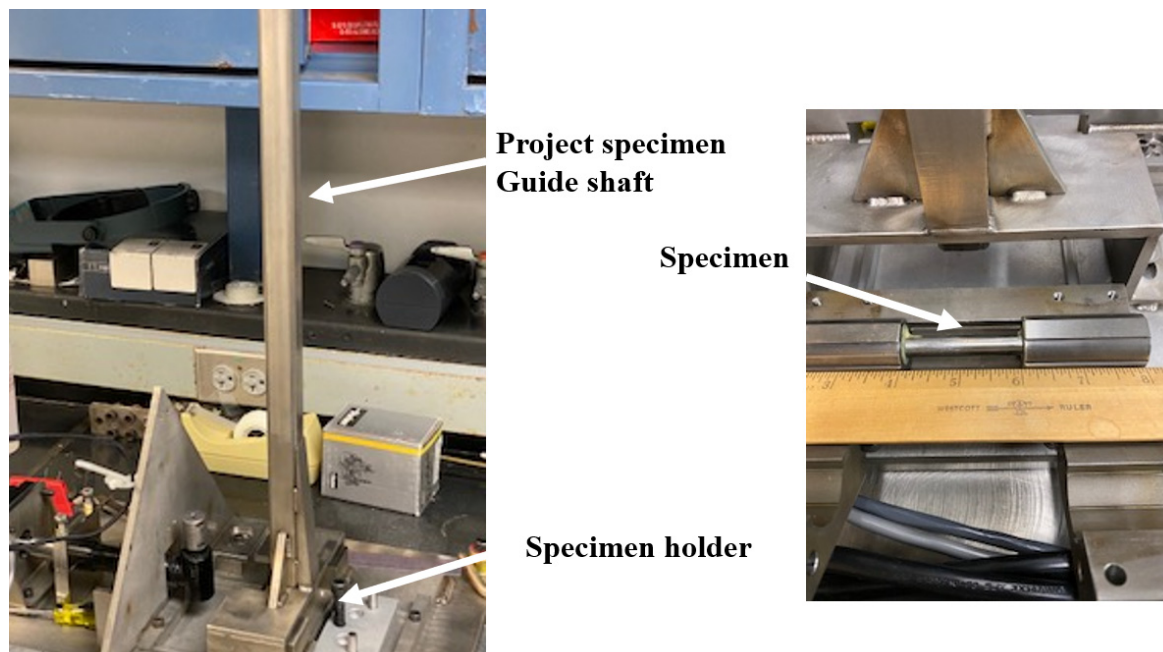


Figure F-51. Physical test configurations with the cumulative effects fixture.



Figure F-52. Impactors used in the physical tests.

To record the maximum g-load on the specimen, a single axis accelerometer was mounted on the specimen with epoxy adhesive. The maximum recordable load for the accelerometer used is 1,100 g. The 85 g projectile was dropped from two different heights: 127 and 25 mm. The mounted accelerometer on the specimen recorded its maximum acceleration of 1,100 g for all tests, indicating a load greater than 1,100 g for all tests. Some attempts were made to reduce the impact load by adding compliant layers to the impact surfaces, but this was unsuccessful.

## **F-8.4 Summary**

Both FEA and experimental evidence indicate that the current configuration of the drop test is not able to recreate the desired g loads on the dogbone specimens used in CIRFT fatigue testing. It was concluded that the stiffness of the dogbone specimen results in very high g-loads. No further investigations were completed, but alternatives will be considered in the coming year. For example, one potential change is to control the impact velocity rather than dropping a target.



## REFERENCES

- [F-1]. *High Burnup Dry Storage Cask Research and Development Project: Final Test Plan*, contract no. DE-NE-0000593, Electric Power Research Institute, Palo Alto, California (2014).
- [F-2]. S. Saltzstein et al., *Visualization of the High Burnup Spent Fuel Rod Phase I Test Plan*, SAND2018-8042-O (2018).
- [F-3]. R. A. Montgomery et al., *Post-Irradiation Examination Plan for High Burnup Demonstration Project Sister Rods*, SFWD-SFWST-2017-000090 ORNL/SR-2016/708, Oak Ridge National Laboratory (2016).
- [F-4]. J.-A. Wang and H. Wang, *FY 2017 Status Report: CIRFT Data Update and Data Analyses for Spent Nuclear Fuel Vibration Reliability Study, Revision 1*, ORNL/SPR-2017/521, SFWD-SFWST-2017-000030/R1 (2017).
- [F-5]. J.-A. Wang and H. Wang, *Mechanical Fatigue Testing of High Burnup Fuel for Transportation Applications*, NUREG/CR-7198/R1 (2017).
- [F-6]. R. A. Montgomery et al., *Sister Rod Nondestructive Examination Final Report*, SFWD-SFWST-2017-000003 Rev. 1 (M2SF-17OR010201021) / ORNL/SPR-2017/484 Rev. 1 (ORNL/SPR-2018/801), Oak Ridge National Laboratory (2019).
- [F-7]. J.-A. Wang and H. Wang, *FY 2017 Status Report: CIRFT Data Update and Data Analyses for Spent Nuclear Fuel Vibration Reliability Study, Revision 1*, ORNL/SPR-2017/521, SFWD-SFWST-2017-000030/R1 (2017).
- [F-8]. J.-A. Wang and H. Wang, *Mechanical Fatigue Testing of High Burnup Fuel for Transportation Applications*, NUREG/CR-7198/R1 (2017).
- [F-9]. W. J. O'Donnell and B. F. Langer, "Fatigue Design Basis for Zircaloy Components," *Nuclear Science and Engineering* 20 (1964): 1–12.
- [F-10]. P. McConnell et al. *Normal Conditions of Transport Truck Test of a Surrogate Fuel Assembly*, SAND2014-20495/FCRD-UFD-2014-000066, Revision 0.1, Sandia National Laboratory, December 2014.
- [F-11]. K. Geelhood et al. "Modeling Structural Loading of Used Nuclear Fuel under Conditions of Normal Transportation," *Ceramic Materials for Energy Application IV*, The American Ceramic Society, 2015.
- [F-12]. J.-A. Wang and H. Wang, *FY 2017 Status Report: CIRFT Data Update and Data Analyses for Spent Nuclear Fuel Vibration Reliability Study, Revision 1*, ORNL/SPR-2017/521, SFWD-SFWST-2017-000030/R1 (2017).
- [F-13]. J.-A. Wang and H. Wang, *Mechanical Fatigue Testing of High Burnup Fuel for Transportation Applications*, NUREG/CR-7198/R1 (2017).
- [F-14]. E. A. Kalinina et al., *Data Analysis of ENSA/DOE Rail Cask Tests*, SFWD-SFWST-2018-00049/ SAND2018-13258R (2018).
- [F-15]. LS-DYNA. "LS-DYNA." <http://www.lstc.com/products/ls-dyna>, (9/1/2020).
- [F-16]. ASME BPVC Sec VIII Div. 2 *Annex 3-D Rules for Construction of Nuclear Facility Components*, 2013
- [F-17]. ASME BPVC Sec II, Part D *Rules for Construction of Nuclear Facility Components*, 2013.

- [F-18]. P. Efsing and K. Pettersson, “Delayed Hydride Cracking in Irradiated Zircaloy Cladding,” Zirconium in the Nuclear Industry: 12<sup>th</sup> International Symposium, ASTM STP 1354, G. P. Sabol and G. D. Moan, Eds, ASTM, West Conshohocken, PA, 340-355, 2000.
- [F-19]. J.-A. Wang and H. Wang, *Data Processing Package for Cyclic Integrated Reversible Bending Fatigue Testing*, ORNL/TM-2021/2114 (2021).
- [F-20]. NUREG-2224, “Dry Storage and Transportation of High Burnup Spent Nuclear Fuel,” US NRC, November 2020.
- [F-21]. J-A. Wang, H. Wang, H. Jiang, B. Bevard, “High Burnup Spent Nuclear Fuel Transport Reliability Investigation,” Nuclear Engineering and Design, 330, 497-515 (2018).